7

Formability of multiaxial warp-knitted fabrics

Abstract: The understanding of the unique behaviour of multiaxial warp-knitted (MWK) fabrics during forming and the practical viability of various forming processes is crucial in assessing their utilization and applicability. In this chapter, a model for the prediction of the formability of an MWK fabric to a 3-D surface is described. For this purpose, a detailed characterization of the forming behaviour of MWK fabrics containing two bias inserting yarns (TBMWK fabrics) is made. A mathematical model is established for predicting the deformations of TBMWK fabrics during the hemisphere-forming process. The shape of flat TBMWK fabric that can yield the corresponding hemisphere during the forming process as well as local deformations can be calculated through this model.

Key words: multiaxial warp-knitted (MWK) fabrics, formability of MWK fabrics, deformation mechanisms, two-bias MWK (TBMWK) fabrics, modelling formability of MWK fabrics, hemisphere.

7.1 Introduction

Over the past decade, there has been a significant amount of research interest in the field of composites, especially in 3-D fabric-reinforced sheet materials. The understanding of the unique behaviour of these 3-D fabrics during forming and the practical viability of various forming processes is crucial in assessing their utilization and applicability. A relatively recent innovation in this field is the use of MWK fabrics as the reinforcement. Knitted fabrics offer a number of potential advantages over woven fabrics: they can be stretched in both directions during forming, thus increasing the potential for forming complex and deeply curved components (Mayer *et al.*, 1998; Mouritz *et al.*, 1999; Savci *et al.*, 2000), they have excellent impact, fracture toughness and energy absorption properties and (in the case of 3-D knits) they exhibit improved out-of-plane mechanical properties.

So far, the bulk of the literature has concentrated on characterizing the mechanical properties of both thermosetting and thermoplastic-based knitted composite materials. Modelling of the mechanical properties (mainly stiffness and tensile) has also been popular. However, limited literature exists on the forming property characteristics of knitted fabric-reinforced thermoplastics (Lim *et al.*, 1998; Takano *et al.*, 2001) and their processing properties are still poorly understood. In fact, most of the literature on

forming properties deals with unidirectional, mostly woven and, to a lesser extent, braided reinforcements, rather than knitted reinforcements.

Although the actual mechanism of sheet forming can be quite complex, a general understanding of the process and material characteristics can be gained through a series of simple experiments including hot-tension, dome-forming, cup-drawing, V-bending and picture-frame experiments. They are designed to subject the material to selective modes of deformation, allowing a more systematic approach to the analysis. One way of obtaining a physical measure of the forming behaviour is to develop kinematic models based purely on geometrical changes. These changes can be measured using grid strain analysis (GSA) where grid points before and after the forming process are used to calculate forming strains. The experiments not only provide a general understanding, but also serve as a check for any predictive work (Duhovic and Bhattacharyya, 2005).

When sufficient data regarding the material and other processing parameters are available, numerical simulations can provide time-saving predictions of the forming behaviour. For materials with complex reinforcing structures, such as knitted fabrics, the material model must be able to accommodate the most important parameters, so that the material can be simulated accurately. Since the forming behaviour of textile composites is governed by their reinforcing structures, the examination of the reinforcement can identify these important parameters. It has been shown that the best results can be achieved using a low-viscosity matrix, i.e., when the lubricating effects are significant. Therefore, the understanding of the deformation behaviour of the reinforcing structure alone is of critical importance. To investigate these parameters physically would be very difficult, because of the scale and level of detail required; however, using advanced numerical simulations, a large quantity of information may be obtainable.

Textile composite materials offer an attractive alternative to metals in the automotive and aerospace industries. However, fibre and yarn movement during fabric forming can cause adverse effects such as wrinkling and thinning, which will lead to a decrease of the mechanical properties of the finished composite (Kaufman, 1991). In addition, the high level of waste generated by subsequent trimming operations is unacceptable. Hence there exists a need to establish a model to predict the deformation and possible wrinkles of MWK fabrics during the forming process in order to enable waste-free design and defect predictability. Before doing this, an understanding of the detailed characterization of the forming behaviour of multiaxial warp-knitted (MWK) fabrics containing two bias inserting yarns (TBMWK fabric) is very important.

In this chapter, a model for the prediction of the formability of a multiaxial warp-knitted (MWK) fabric to a 3-D surface has been described. For this purpose, a detailed characterization of the forming behaviour of MWK

fabrics containing two bias inserting yarns (TBMWK fabric) was made. Through experimental observation, it was found that the two bias inserting yarns always tend to gather along the weft direction. The angle between the two bias yarns has a linear relationship with the perpendicular distance from the measured points to the longitudinal axis of the hemisphere during the forming process. The slope of this linear relationship is also linear with the magnitude of the radius of the pressing hemisphere, provided that the radius is larger than 7 cm.

Based on the above finding, a mathematical model is established for predicting the deformations of TBMWK fabrics during the hemisphere-forming process. The shape of flat TBMWK fabric that can yield the corresponding hemisphere during the forming process as well as local deformations can be calculated through this model. The hemisphere-forming experiments show that the present model is workable and accurate. The results from both the model and experiments suggest that the shape of flat TBMWK fabric that can yield the corresponding hemisphere is close to rectangular, not square as presented by woven fabric.

The method developed in this chapter has laid a foundation for further modelling of the forming behaviour of MWK fabrics onto other 3-D surfaces. More importantly, it is of great value to find that the two bias inserting yarns always tend to gather along the weft direction of the fabric, which is a starting point for modelling of the forming behaviour of MWK fabrics.

7.2 Textile composite deformation mechanisms

In thermoforming textile composite materials, it is useful to understand the deformation mechanisms that take place inside them, so that the forming process can be optimized to produce parts of the best quality. The experimental observations and measurements are helpful for a general understanding, but do not provide enough detail to reveal the actual mechanisms. The following sections attempt to investigate these mechanisms in more detail.

The hierarchy of deformation modes for this family of composite materials can be divided into three categories: prepreg flow mechanisms, macro-level fabric deformation modes, and micro-level fabric deformation modes, each of which contains a number of different mechanisms.

7.2.1 Prepreg flow mechanisms

When the textile fabric reinforcement is combined with the matrix to form the composite prepregs, a set of deformation modes are introduced, which may be referred to as top-level deformation modes since they involve the movements of the reinforcement (macro- and micro-level fabric deforma-

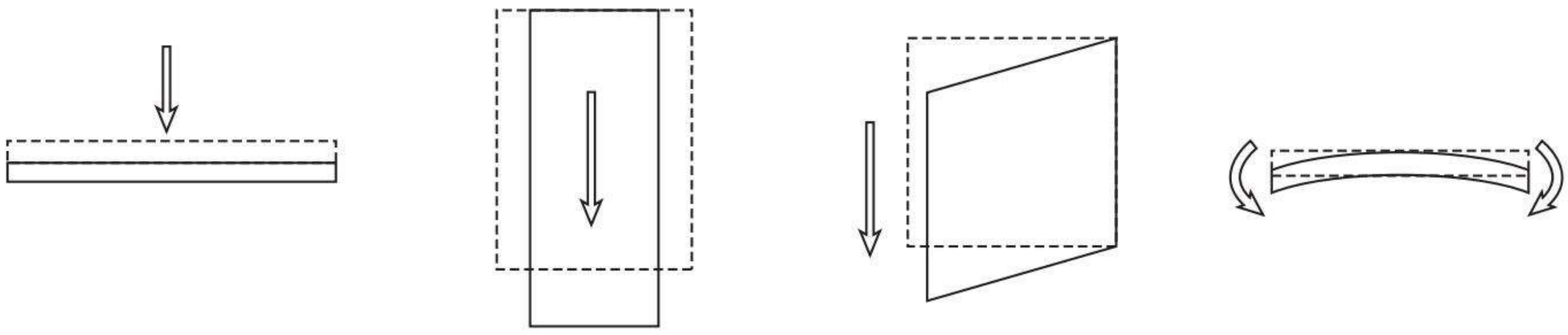

7.1 Macro-level fabric deformation modes.

tion mechanisms) and the matrix. They are in fact the conformation modes of the composite prepreg sheet or group of sheets, as is usually the case, during the forming process. The hierarchy of the top-level deformation modes consist of transverse flow, resin percolation, interply shear and intra-ply shear, as summarized by Cogswell (1992) and revisited by Martin *et al.* (1997).

7.2.2 Macro-level fabric deformation modes

The four types of macro-level fabric deformation modes, as shown in Fig. 7.1, describe the deformations observed when looking at the fabric as a whole. However, the way in which each fabric complies to these modes is different and can be attributed to the deformations occurring within the textile structure itself. These sub-structure or micro-level deformation modes are the real mechanisms behind textile deformations and need to be identified in order to understand the material's behaviour.

7.2.3 Micro-level fabric deformation modes

Micro-level fabric deformation modes exist through the interaction of structured yarns within the fabric. Figure 7.2 shows what are generally believed to be the eight micro-level deformation modes for textile fabrics. Inter-yarn slip, as shown in Fig. 7.2(a), occurs when the yarns that construct the fabric move over one another. It is one of the modes of deformation belonging almost exclusively to knitted fabrics. In this mode of deformation, the friction between the yarns becomes important since it determines where the onset of buckling will take place, as well as the magnitude of the forming forces required. Fortunately, the matrix and fibre chemical sizing (coatings) usually lubricate the yarn to help this mode of deformation.

Inter-yarn shear is a common mode of deformation in many woven fabrics. This is where the yarns rotate about their crossover points to accommodate the required deformation, as shown in Fig. 7.2(b). In fact, this type of mechanism has been reported to occur in multilayered continuous fibre-reinforced composites also, as outlined by Krebs and Bhattacharyya (1998),

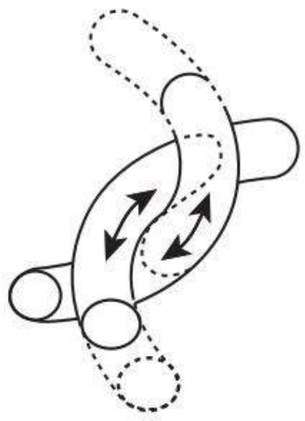

(a) Inter-yarn slip

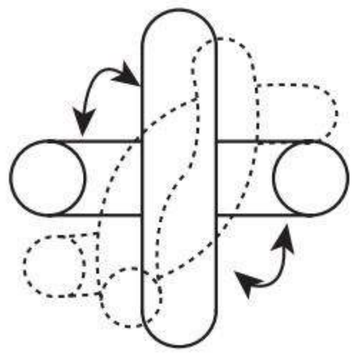

(b) Inter-yarn shear

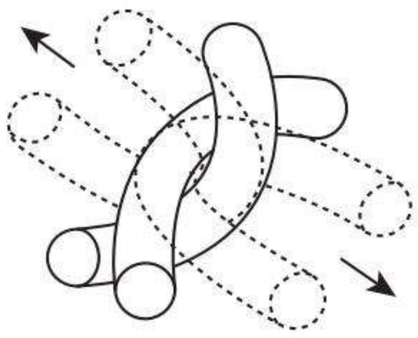

(c) Yarn bending

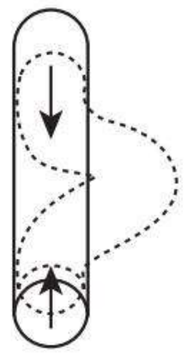

(d) Yarn buckling

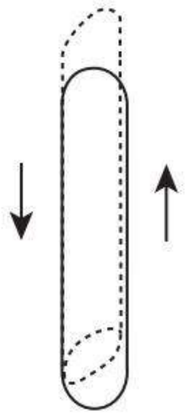

(e) Intra-yarn slip (inter-fibre friction)

(f) Yarn stretching

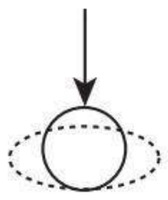

(g) Yarn compression

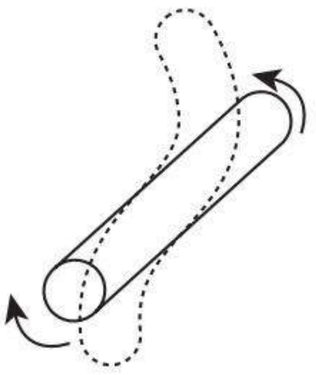

(h) Yarn twist

7.2 Micro-level fabric deformation modes.

Martin *et al.* (1997) and Christie (1997), and is commonly referred to by many researchers as the 'trellising effect'. In knitted fabrics, depending on the orientation of the reinforcement, large in-plane tension and in-plane shear can be accommodated, but not in the same direction.

The yarn bending or 'straightening' shown in Fig. 7.2 is in many cases the most significant deformation mode in many textiles. It is the most influential mode in knitted fabrics because of the knit loop geometry. Straightening also occurs to a lesser extent in woven and braided fabrics depending on the amount of crimp or yarn undulation present in the fabric structure. Out of all the different deformation modes, fibre buckling is the only unfavourable one since the material movement through this mode creates what is considered as defects, although it is quite difficult to observe with complex structures, such as knits and braids. Out-of-plane buckling usually occurs when the inplane modes cannot accommodate the required deformation. In-plane buckling can also occur, but is less likely due to in-plane geometric constraints – see Fig. 7.2(d).

The intra-yarn slip shown in Fig. 7.2(e) coupled with yarn bending, Fig. 7.2(c), are the biggest contributors to a textile fabric force–displacement curve. Intra-yarn slip is where the continuous fibres within the yarn slide past one another along the length of the fibre because of changes in fibre curvature during bending and unbending. The yarn stretching, Fig. 7.2(f), while not so prominent in the early stages of fabric deformation, is certainly present and contributes significantly to the deformation at larger strains.

Another fabric deformation mechanism to consider is yarn compression, Fig. 7.2(g), where forces at yarn crossover points compress the filaments in

the yarn and cause them to flatten out and conform to the curvature of perpendicular yarns. Like fibre stretching, this can also be considered relatively insignificant; it only starts to contribute to the load–extension curve once the aforementioned mechanisms have been exhausted.

Finally, the yarn twist, Fig. 7.2(h), which has been observed in knitted fabrics and not so much in woven fabrics, imparts further resistance to the fabric deformation. This is where the yarn is subjected to one full turn during the manufacture of the fabric in order to create the looping structure of the knit. The twist creates a resistance to the increase in yarn curvature during fabric deformation.

7.3 Structure of multiaxial warp-knitted fabrics

The basic structure of MWK fabrics has been discussed in previous chapters (e.g. Chapter 3). The typical structure of an MWK fabric is illustrated in Fig. 7.3. A variation of this structure contains two bias inserting yarn systems, hereafter called TBMWK fabric, which is the main concern of this chapter and will be introduced in later sections.

MWK fabrics may still be categorized as 2-D reinforcements even though there is a stitching system (chain or tricot loops) which partly orients along the thickness direction and accordingly improves the through-thickness strength as well as the interlaminar shear resistance. This kind of fabric thus can be applied for conforming to a 3-D surface, which is called the forming process. There have been many papers (Mack and Taylor, 1956; Robertson *et al.*, 1981, 1984; Heisey and Haller, 1988; Amirbayat and Hearle, 1989; Bassett and Postle, 1990; Bergsma, 1993; Aono *et al.*, 1994, 1996; Laroche and Vu-Khanh, 1994; Long, 1994; Hu *et al.*, 1998) published on the forming behaviour of woven fabrics, most of which are based on the main and

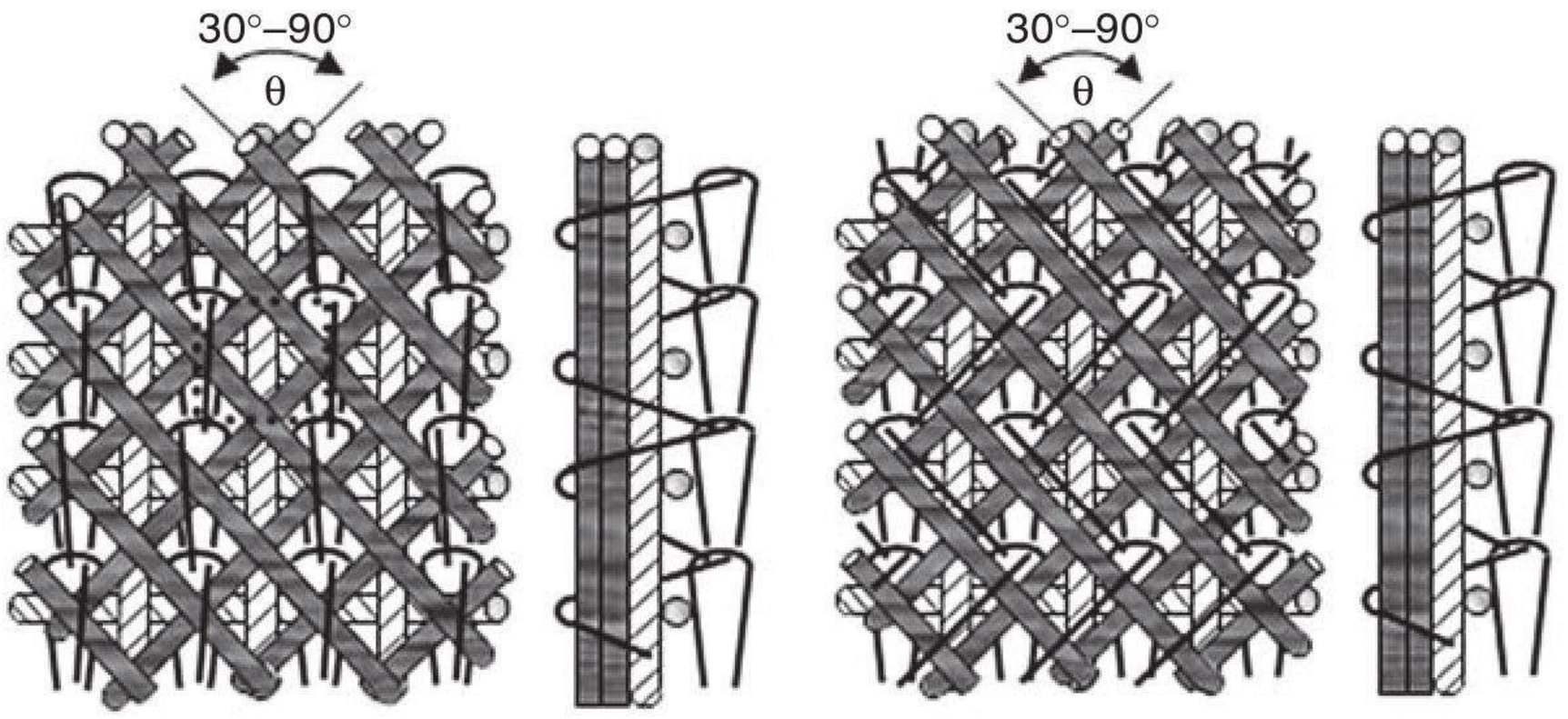

(a) Chain structure (b) Tricot structure

7.3 Typical structure of an MWK fabric.

important assumption that the two interlaced yarn systems in a plain weave are pin-jointed together at crossovers.

In the 2-D fabric forming process, the main deformation modes usually include in-plane tension, transverse compression, in-plane shear and out-of-plane bending, of which the in-plane shear is the most important. It can be regarded as the dominant factor which dictates whether the desired 3-D surface can be formed or not.

7.4 Deformation characteristics of woven fabrics during the forming process

For woven fabrics, the in-plane shear deformation directly determines the magnitude of the locking angle (Bergsma, 1993), which determines the jamming state during forming. It can be seen according to experiments that woven fabrics are formed into a 3-D surface just through the changes of the original right angle between the warps and wefts, as illustrated in Fig. 7.4 (a woven fabric with yarns of glass filament bundles). This has also been shown by many other authors (Mack and Taylor, 1956; Robertson *et al.*, 1981, 1984). This means that, under the assumption of inextensibility of the constituent yarns, the in-plane shear deformation (trellis effect) plays the leading role in the forming process of woven fabrics. If the fabric can be sheared to a great degree, which means the locking angle is sufficiently small, better forming will result and a more complex 3-D surface may be formed. Once the locking angle is exceeded, wrinkles or buckling will occur.

7.5 Deformation characteristics of multiaxial warp-knitted fabrics during the forming process

For MWK fabrics the situation is quite different due to the different geometrical structures. Our earlier study (Hu *et al.*, 1998) suggests that the typical structure of an MWK fabric (Fig. 7.3) presents an isotropy in the in-plane tensile properties, which is the unique mechanical advantage of this kind of fabric. However, this is at the same time a disadvantage owing to the possibility of deformation during the forming process. The dotted

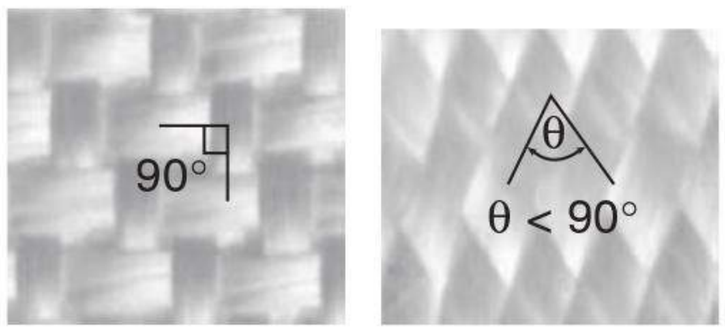

(a) Undeformed state (b) Deformed state

7.4 Trellis effect of the woven fabric.

square marked in Fig. 7.3(a) represents a unit cell which can never be sheared easily no matter how the in-plane shear force is exerted, since in all situations there will be one or more systems of inserting yarns stretched by the shear force. This means that the typical structure of MWK fabric is more difficult to deform, i.e. to conform to a 3-D surface. As illustrated in Fig. 7.5(a), the hemisphere pressing experiment gives a proof to this analysis in which wrinkles occur. However, a variant structure of MWK fabric (as shown in Fig. 7.6) shows quite good conformability, as suggested by

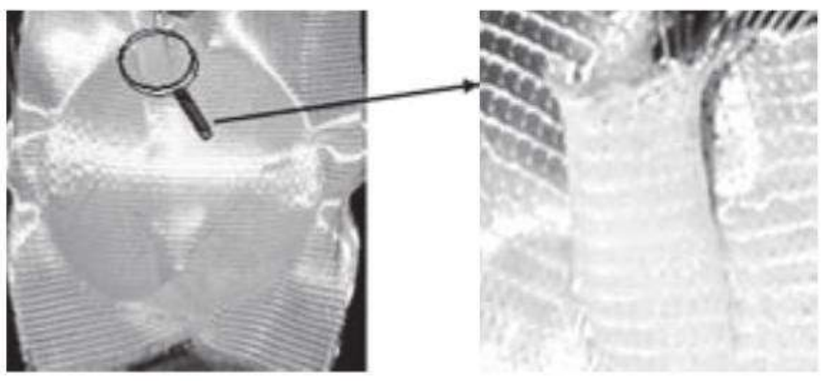

(a) Typical structure (as shown in Fig. 7.3, inserting yarns are glass fibre bundles)

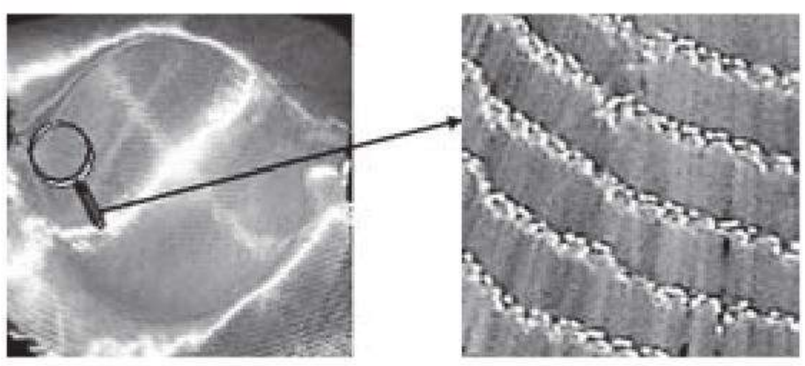

(b) MWK fabric with only two bias inserting systems (as shown in Fig. 7.4)

7.5 Hemisphere-pressing experiments on MWK fabrics.

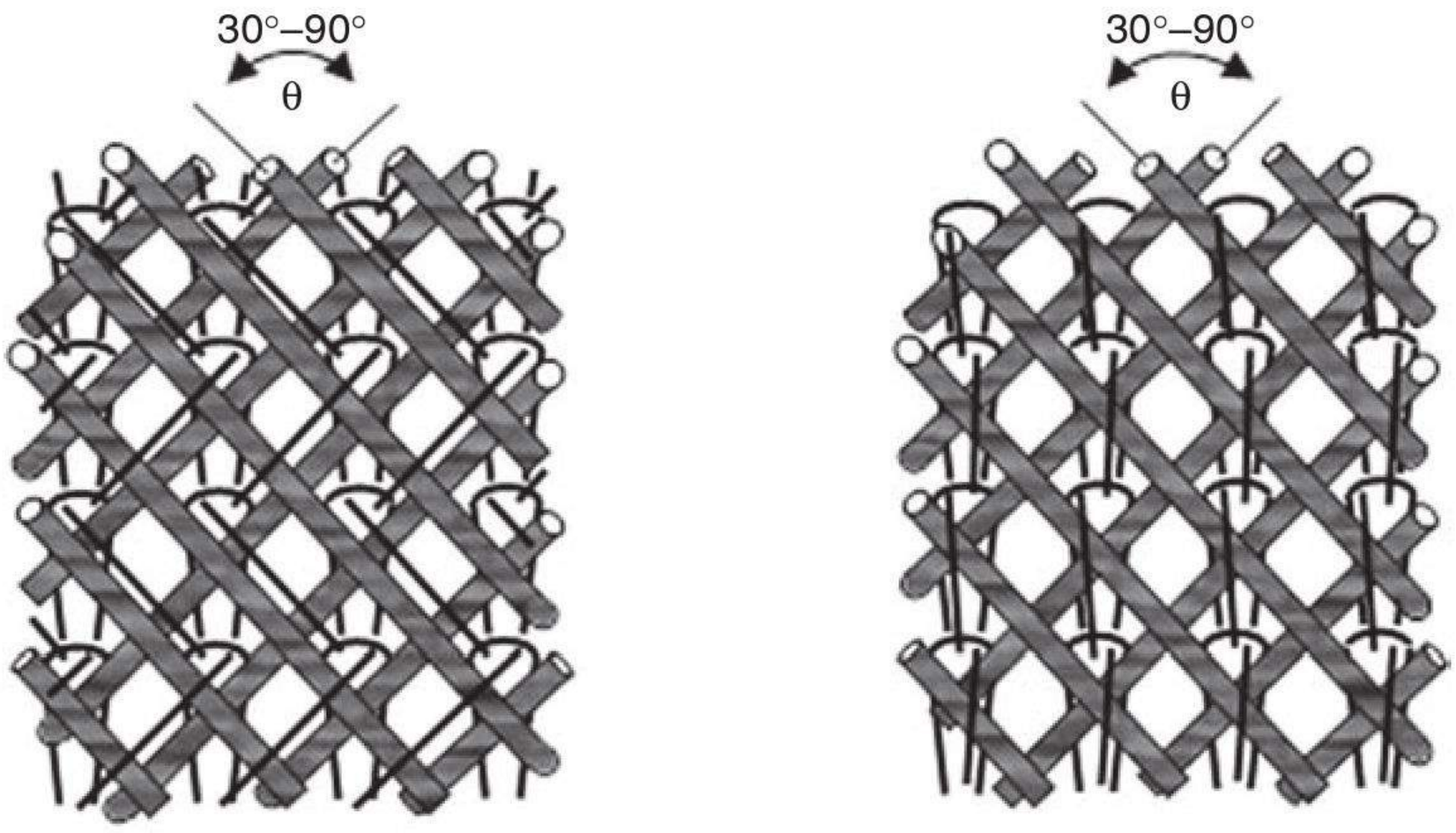

(a) Tricot structure

(b) Chain structure

7.6 A variation of MWK fabric (TBMWK) containing only two bias inserting yarn systems.

Fig. 7.5(b), in which the inserting yarns come gathered together along the weft direction.

It can be inferred from Fig. 7.5 that the typical structure of MWK fabric is more suitable for plate or low-curvature-shell composite material, and the structure shown in Fig. 7.6 (hereafter in this chapter called two-bias multiaxial warp-knitted (TBMWK) fabric) has great potential in forming 3-D complex preforms. In the subsequent sections of this chapter, discussions will be concentrated on deformations of TBMWK fabrics.

7.6 Deformation behaviour of two-bias multiaxial warp-knitted fabrics

7.6.1 Relative movement of two inserting yarn systems

As shown in Fig. 7.6, the TBMWK fabric contains only two bias inserting yarn systems. Since the inserting yarn systems are not interlaced as the woven fabric but overlapped together, there are obviously fewer frictional constraints at the contact area. This means that the relative movement between the two inserting systems will be easier. Actually, the angle between the two systems can nearly approach 0° after deformation, as illustrated in Fig. 7.7(a), in which both inserting yarn systems become nearly parallel to the weft direction. However, the analogous phenomenon, that both inserting yarn systems become nearly parallel to the warp direction when the exerted forces change direction, does not occur as might be expected, as denoted in Fig. 7.7(b).

Figure 7.7 gives the deformations of the TBMWK fabric with tricot loops (Fig. 7.6(a)). The other structure, TBMWK fabric with chain loops (Fig. 7.6(b)), presents a similar deformation, as shown in Fig. 7.8.

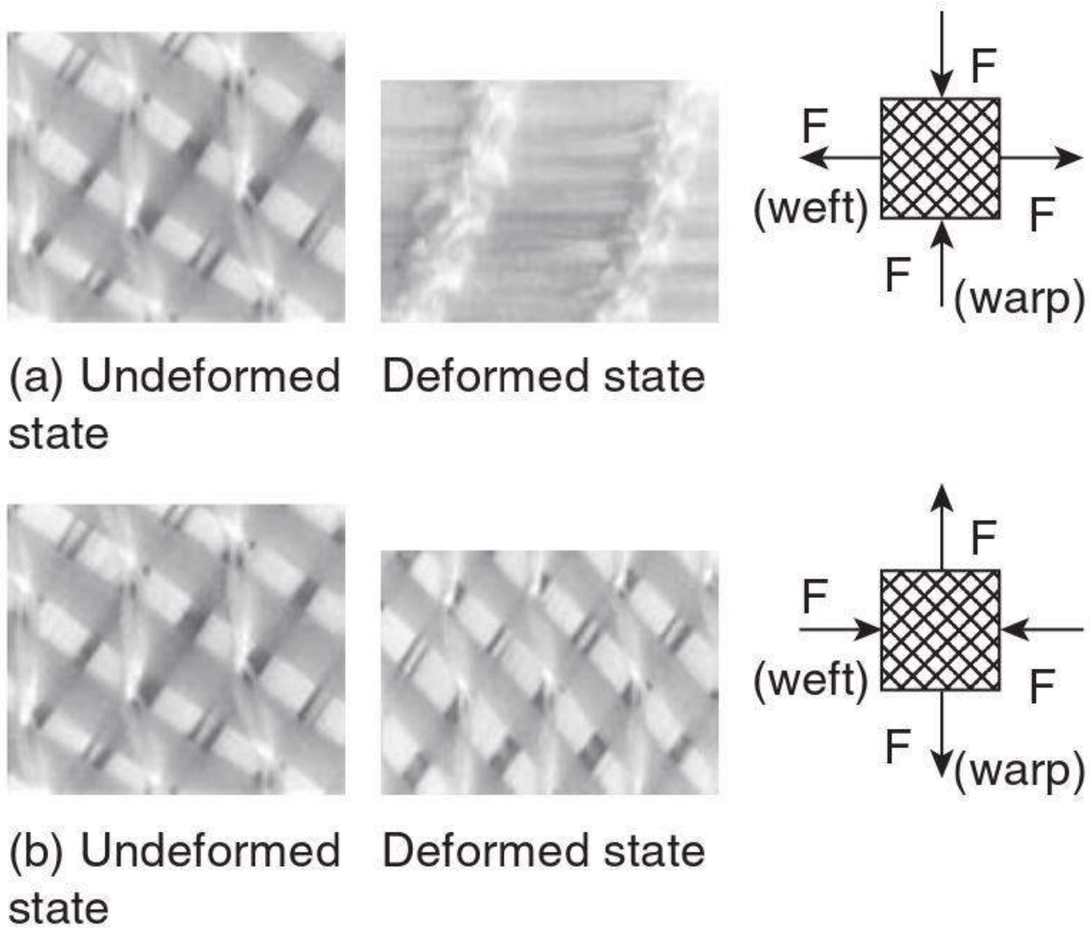

(a) Undeformed state Deformed state

(b) Undeformed state Deformed state

7.7 Deformations of a TBMWK fabric with tricot loops.

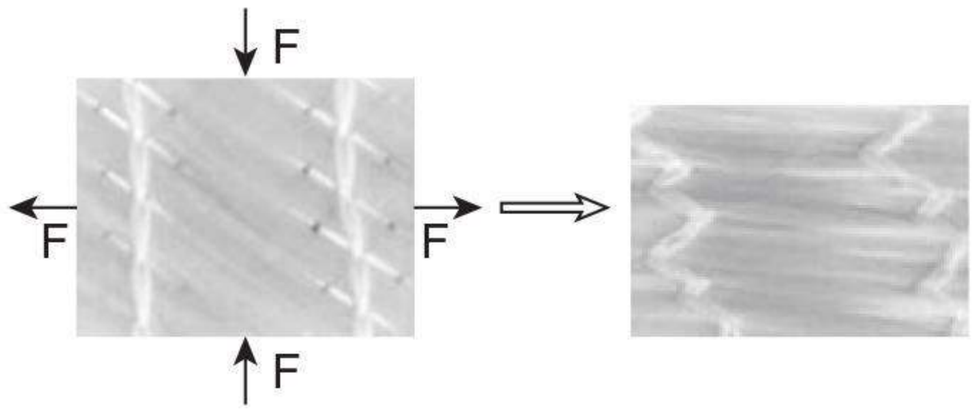

7.8 Deformations of a TBMWK fabric with chain loops.

7.6.2 Roles of stitching loops on the deformation of two-bias multiaxial warp-knitted fabrics

The inserting yarns always being gathered along the weft direction is the unique deformation characteristic of TBMWK fabric, which is quite different from woven fabrics. The deformation of woven fabric should be similar under the exerted force conditions of Fig. 7.7(a) and (b) or Fig. 7.8(a) and (b), i.e. the yarns will tend to orient along the ±45° directions (measured from the warp or weft direction). This has been proved from the experiment of Robertson *et al.* (1981) of shaping cotton cheesecloth around a bowling ball. Apparently, this special deformation behaviour of TBMWK fabric must result from the stitching system – tricot loops or chains. Microphotographs of deformations of these two kinds of stitches under stretching force can clearly explain this deformation characteristic, as shown in Fig. 7.9.

Although the tricot fabric can extend in both the weft and warp directions, the fabric elongation along the warp direction is much smaller than that along the weft direction (Fig. 7.9(a)). The extensibility of the chain loops (Fig. 7.9(b)) is also much smaller (3% or so for polyester filament yarn of 15 Tex). As shown in Figs 7.7(b) and 7.8(b), when the inserting yarns in the TBMWK fabric tend to orient along the warp direction, the stitching system (just being stretched in the same direction) constrains their movement. From this point of view, when the TBMWK fabric conforms to a 3D surface, the quick and easy response of the inserting yarns is to orient along the weft direction, as justified by Fig. 7.5(b). This deformation behaviour of

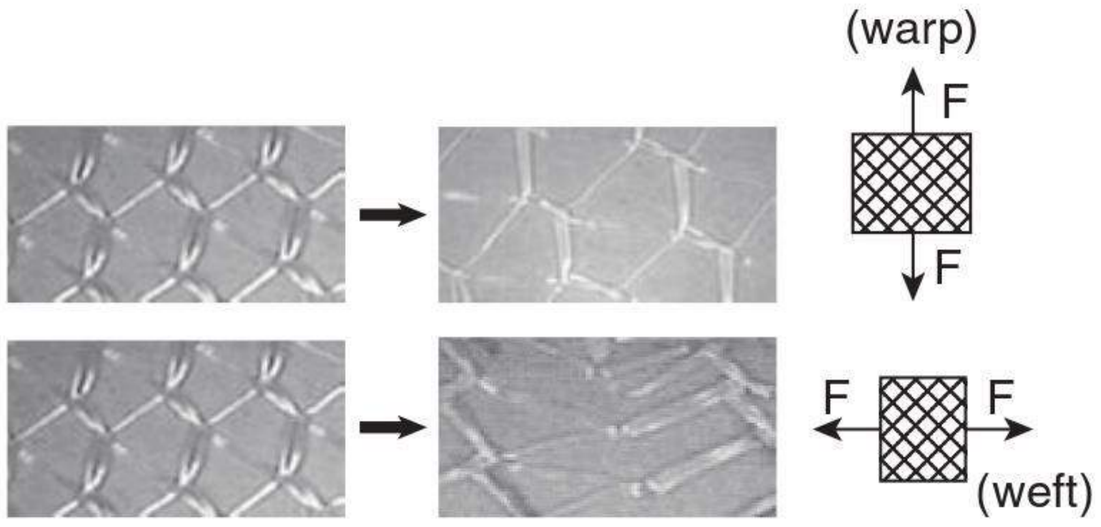

(a) Deformation of tricot loops

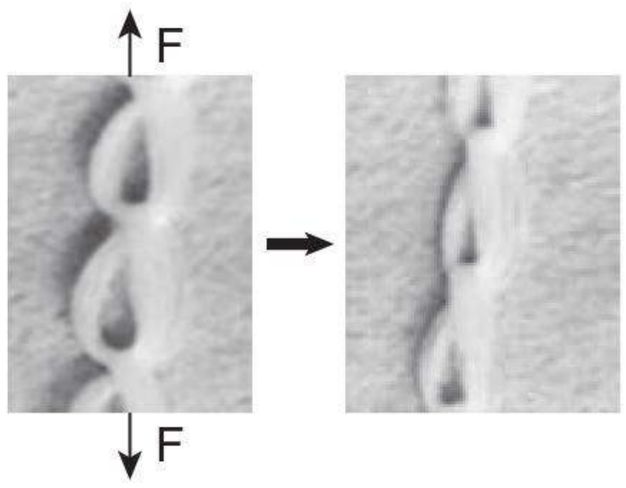

(b) Deformation of chain loops

7.9 Deformations of tricot loops and chains.

TBMWK fabric is of great importance as far as the design of the forming process is concerned.

7.6.3 Hemisphere-pressing experiments

Hemisphere-pressing experiments were conducted on three sample fabrics in order to study the forming behaviour of TNMWK fabric. Specifications of the samples are listed below:

- Sample 1: TBMWK fabric, consisting of two bias (±45°) inserting yarn systems (glass filament bundles, count of 300 Tex, density of 6.8 yarns per cm, yarn width of 0.98 mm), held by tricot loops (polyester filaments, count of 15 Tex).
- Sample 2: TBMWK fabric, consisting of two bias (±45°) inserting yarn systems (glass filament bundles, count of 250 Tex, density of 10.3 yarns per cm, yarn width of 0.96 mm), held by chain loops (polyester filaments, count of 15 Tex).
- Sample 3: plain woven fabric, consisting of two interlaced yarn systems (glass filament bundles, count of 300 Tex, density of 11 yarns per cm, yarn width of 0.86 mm).

A series of hemispheres of different radii ranging from 5 to 15 cm are chosen in order to study the effect of the magnitude of the radius on the forming results. The angle changes between yarns are measured along the weft direction for TBMWK fabrics or along the ±45° directions for

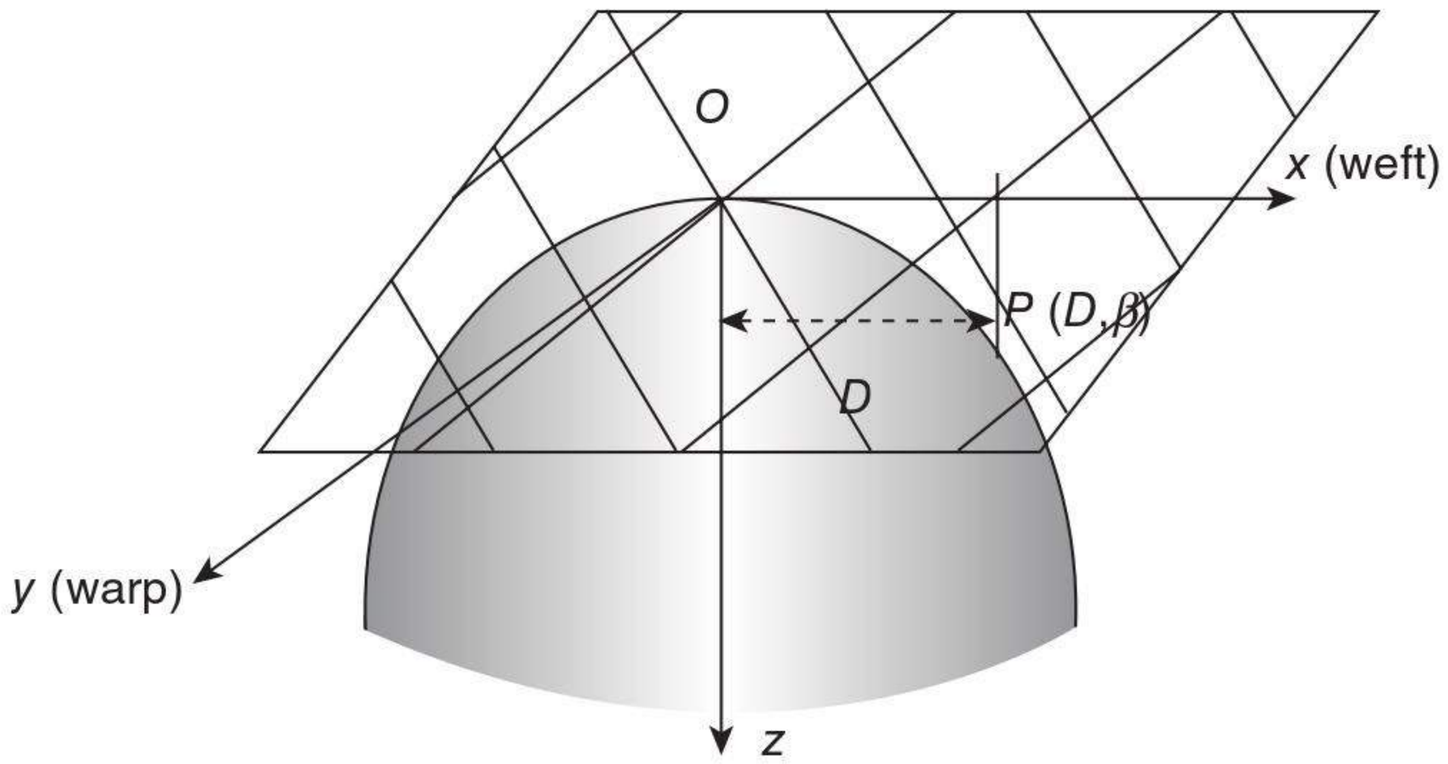

7.10 Illustration of measurement.

the plain-woven fabric. In addition, comparisons are also made between the patterns of flat TBMWK fabric and plain-woven fabric that can yield the corresponding hemisphere surface.

7.6.4 Theoretical analysis

As shown in Fig. 7.10, we assume that the centre point O (assumed to be some crossover point) of the original flat sample fabric happens to touch the pole of the pressing hemisphere after forming. Measurements are made of angles (denoted β in degrees) as well as the corresponding distances (denoted D in cm). Angles β are between the two bias inserting yarn systems along the weft direction for Samples 1 and 2, and between warps and wefts along the ±45° directions for Sample 3. D is the distance from the measured point (such as P) to the longitudinal axis of the hemisphere. In Fig. 7.11, the relation between D and β is presented for hemispheres with radii of 7.5 and 11 cm.

In order to consider comprehensively the effect of the magnitude of the radius of the pressing hemisphere on the relation between D and β, more pressing experiments (the radius of the pressing hemisphere ranging from 5 to 15 cm) were carried out on Sample 1. In Fig. 7.12, the relation between the slope of the trendline for the plot of D versus β and the radius of the pressing hemisphere, as well as the relation between the correlation coefficient of the trendline for the plot of D versus β and the radius of the pressing hemisphere, are presented. It can be inferred from Figs 7.11 and 7.12 that:

- The plot between D and β basically possesses good linearity, and the larger the radius of the pressing hemisphere, the higher the linearity.
- The slope of the trendline for the plot of D versus β is linear with the radius of the pressing hemisphere, and the larger the radius, the smaller the absolute value of the slope.

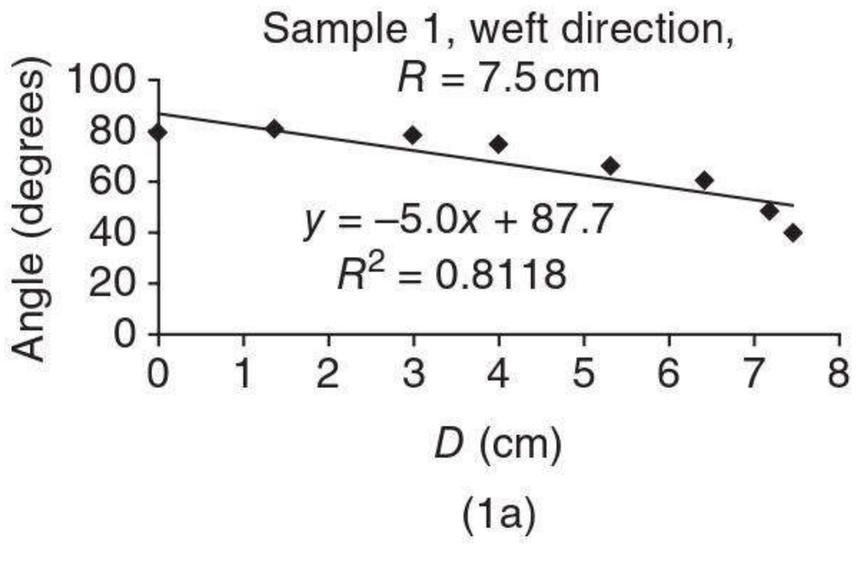

(1a)

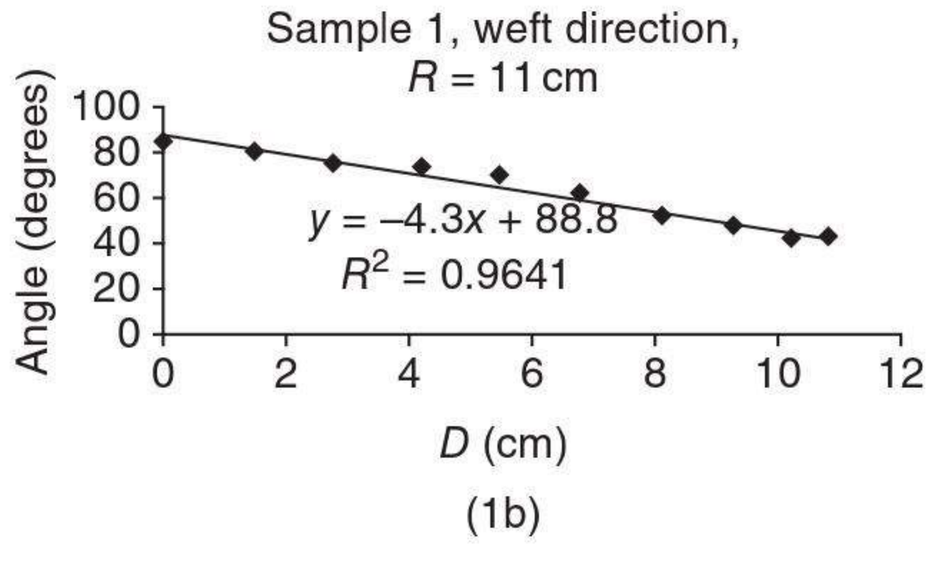

(1b)

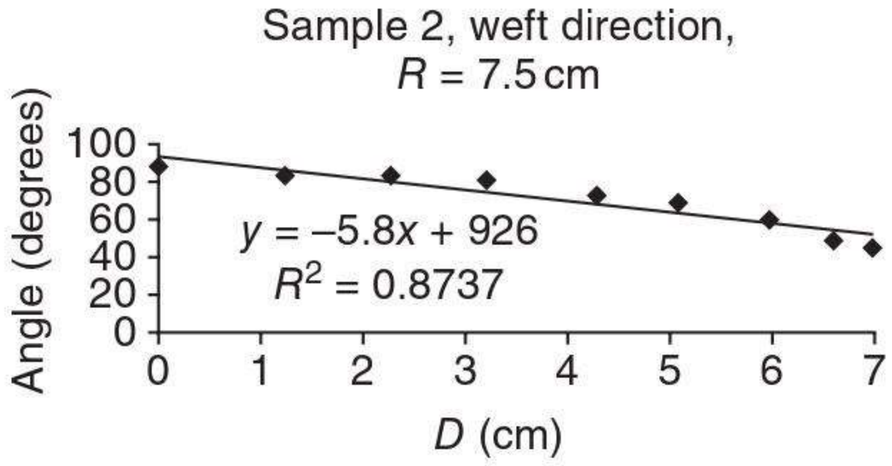

(2a)

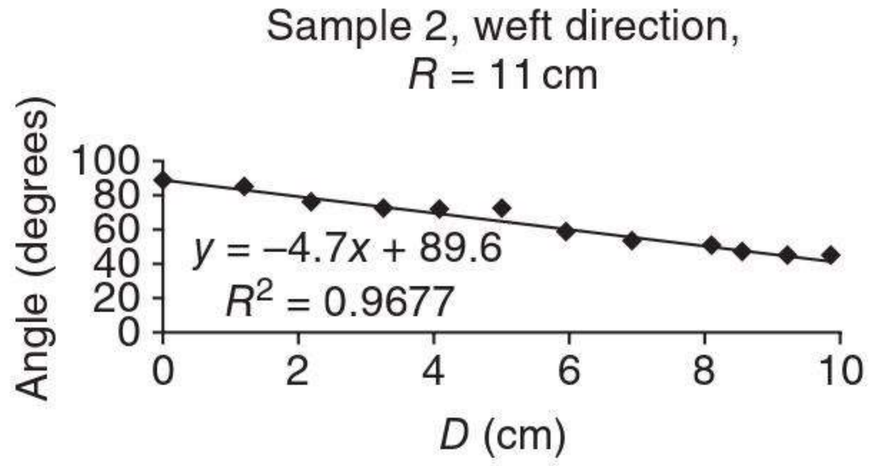

(2b)

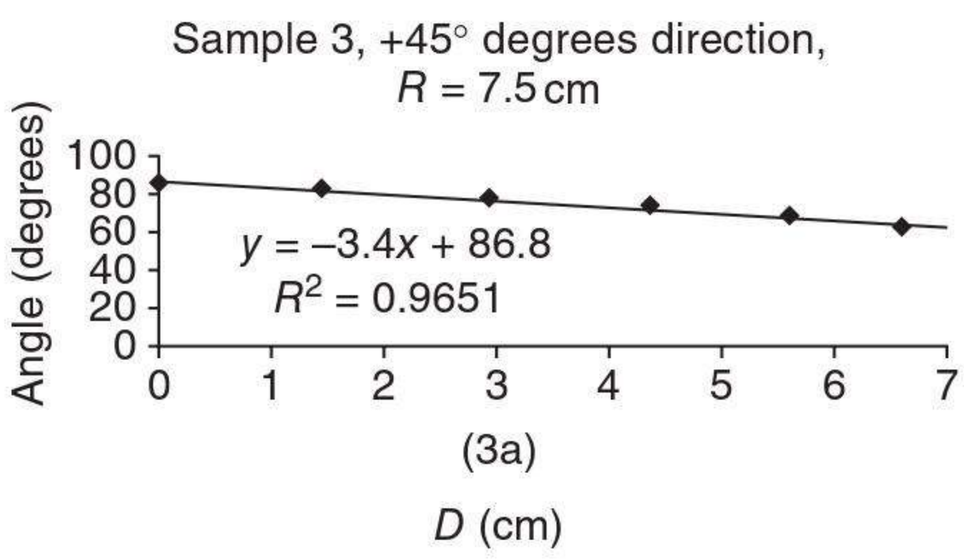

(3a)

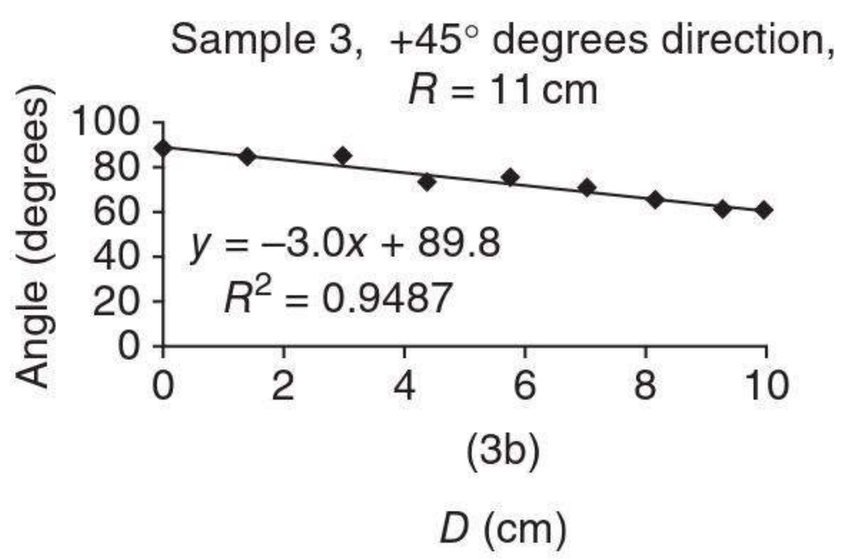

(3b)

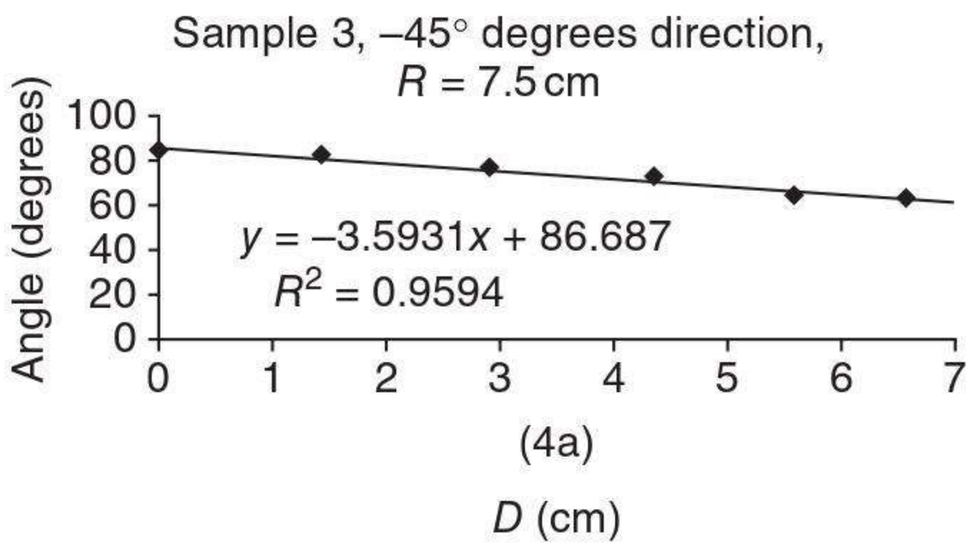

(4a)

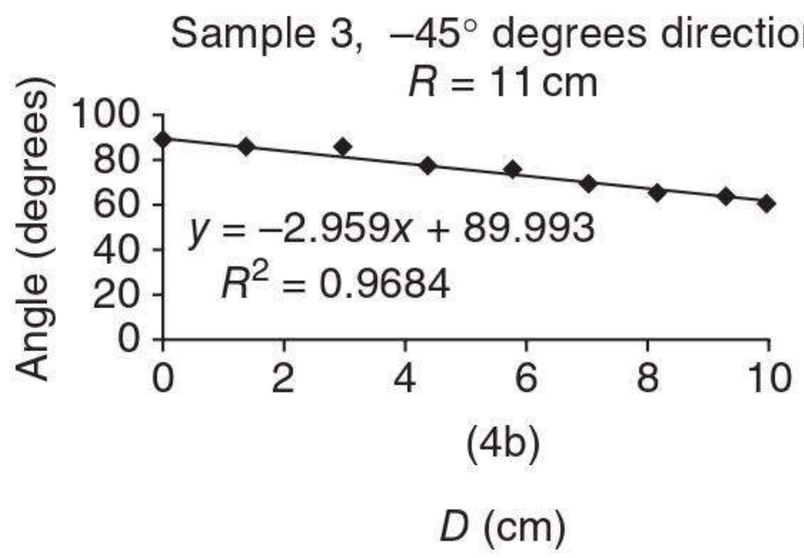

(4b)

7.11 The relation between D and β for hemispheres with radii of 7.5 and 11 cm.

- The correlation coefficient of the trendline for the plot of D versus β is also linear with the radius of the pressing hemisphere, and the larger the radius, the larger the correlation coefficient (close to unity).
- The inserting yarns of TBMWK fabrics tend to become gathered always along the weft direction since the slope for the plot D versus β is always negative.
- The plots of D versus β for Sample 3 along the –45 and +45° directions are just analogous.

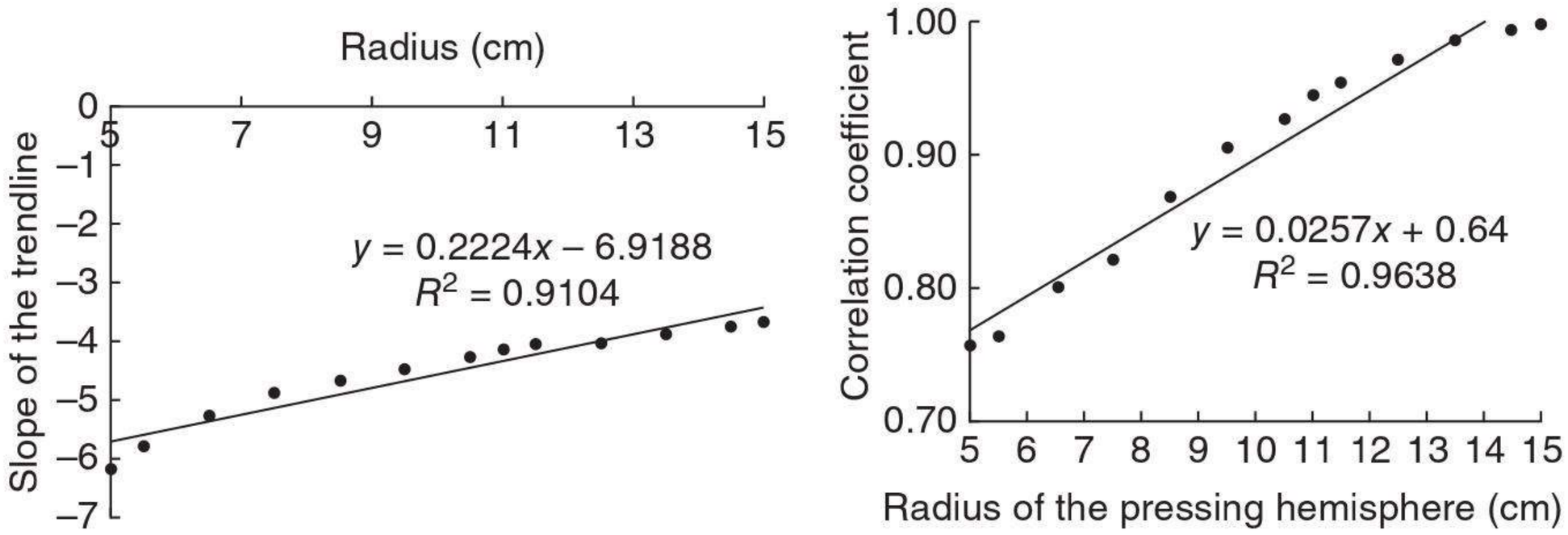

7.12 Effect of radius magnitude of a pressing hemisphere on the relation between D and β.

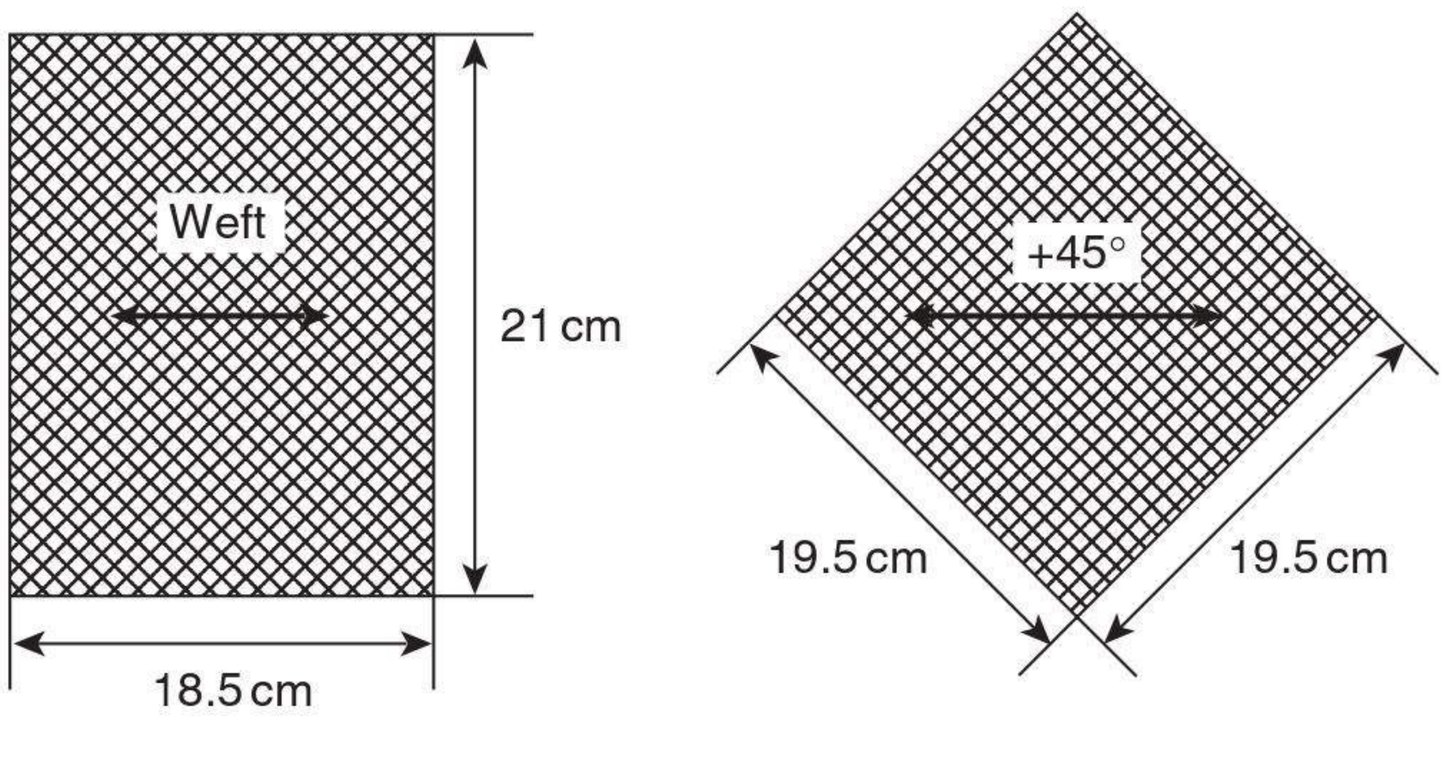

(a) Sample 1, R = 7.5 cm (b) Sample 3, R = 7.5 cm

7.13 Schematic diagram of the flat patterns of both TBMWK fabric and woven fabric that can yield a hemisphere of diameter 7.5 cm.

Other hemisphere-pressing experiments show that the plot of D versus β is non-linear and the correlation coefficient of the trendline decreases below 0.8 when the radius of the pressing hemisphere is less than 7 cm. It is also impossible to represent the relationship between D and β by a simple equation under this condition.

Figures 7.11 and 7.12 just provide proofs to the foregoing analysis of the deformation behaviour of TBMWK fabrics as well as the woven fabrics. In addition, it can also be seen from the schematic diagram in Fig. 7.13 that the two inserting yarn systems of a TBMWK fabric tend to become gathered along the weft direction during the hemisphere-pressing process. Figure 7.13 gives the schematic flat patterns of both TBMWK fabric and woven fabric that can yield a hemisphere of diameter 7.5 cm, in which pattern (a) is close to rectangular while pattern (b) is close to square.

7.7 Modelling the formability of two-bias multiaxial warp-knitted fabrics

As suggested by Fig. 7.11, the relation between D and β presents very good linearity and the slope of the trendline is not sensitive to the diameter of the pressing hemisphere provided that the radius of the pressing hemisphere is more than 7 cm. Accordingly, it is reasonable to use one linear equation to represent the relation between D and β for a specified radius (more than 7 cm) of the pressing hemisphere. Based on this point of view, a model for predicting the deformation of TBMWK fabrics during the hemisphere-forming process is established. The model makes two main assumptions: (1) the distance between any two adjacent crossovers along any single inserting yarn remains unchanged; and (2) the relative slippage between the two inserting yarn systems is ignored in consideration of the constraints of the stitching system.

7.7.1 Modelling the forming process of two-bias multiaxial warp-knitted fabrics

An illustration of the vertical view of the sample fabric after deformation is given in Fig. 7.14, in which the xOy coordinate system simply corresponds to that in Fig. 7.10.

If we use the equation $\alpha = Kx + \alpha_0$ to represent the relation between D and β (Fig. 7.10), the coordinates of point A (1,1) in the 3-D Cartesian coordinate system (Fig. 7.14) are

$$\begin{cases} A_x(1,1) = L_0 * \sqrt{(\cos^2(\alpha_0/2) - L_0{}^2/4R^2)} \\ A_y(1,1) = -L_0 * \sin(\alpha_0/2) \\ A_z(1,1) = L_0{}^2/2R \end{cases}$$

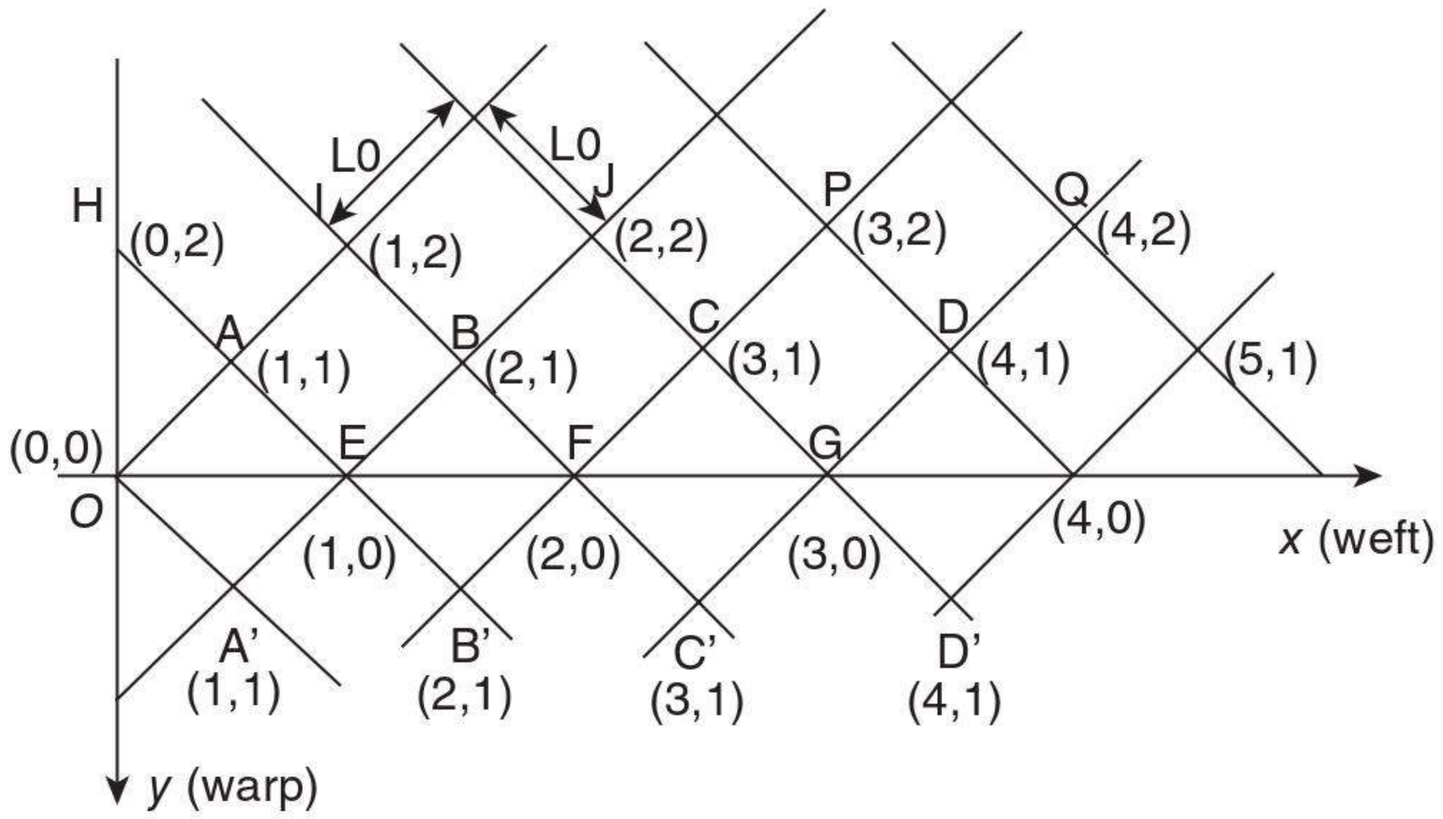

7.14 Illustration of the vertical view of the sample fabric after deformation.

in which α_0 corresponds to angle AOA'. Then the coordinates of the symmetrical point A' of A about plane xOz can be obtained. To locate the node point E (1,0), we consider the points of intersection of three spheres: one centred at A (1,1) of radius L_0, another centred at A' (1,1) of radius L_0, and the third the hemisphere of radius R. These three spheres will intersect at two points: O (0,0) and E (1,0). Here and in each subsequent step we will choose the point furthest from the pole. According to the angle BEB' (E_x (1,0)$K + \alpha_0$) and the coordinates of point E, the locations of B and B' can be determined. Following these steps, the locations of all the node points $O, E, F, G, \ldots$ and $A, B, C, D, \ldots$ can be calculated. The coordinates of all the other points can also be obtained through the same method, i.e. solving the group of equations of three spheres. For example, to locate the node point H (0,2), we consider the points of intersection of three spheres: one centred at A'' (1,1) of radius L_0 (A'' is the symmetrical point of A about the plane yOz), another centred at A (1,1) and the third the hemisphere of radius R. To locate the node point P (3,2), we consider the points of intersection of three spheres: one centred at C (3,1) of radius L_0, another centred at D (4,1) of radius L_0, and the third the hemisphere of radius R.

Since the angles between the two inserting yarn systems along the weft direction can nearly become 0° (as shown in Figs 7.5(a) and 7.6(a)), we have reason to use the distances (d_C) between the pairs of symmetrical points ($AA', BB', CC', DD', \ldots$) as criteria to determine whether wrinkles occur or not. If d_C becomes less than the width of a single inserting yarn during theoretical calculation, we assume that wrinkles occur.

7.7.2 Verification of the model

In Fig. 7.15, the calculated vertical view (xOy plane) and side view (yOz plane) of Sample 1 after deformation in the hemisphere-pressing experi-

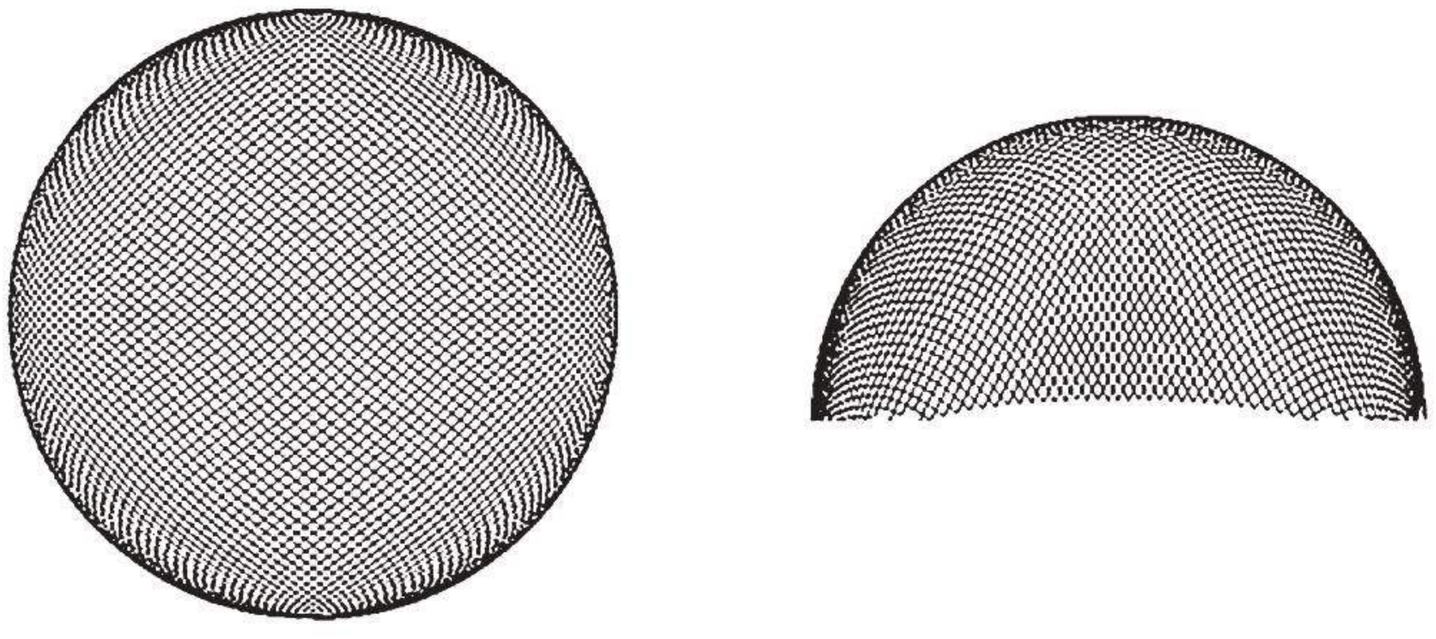

(a) Vertical view (b) Side view

7.15 Calculated vertical view and side view of Sample 1 after deformation in the hemisphere-pressing experiment (Sample 1, $R = 7.5$ cm).

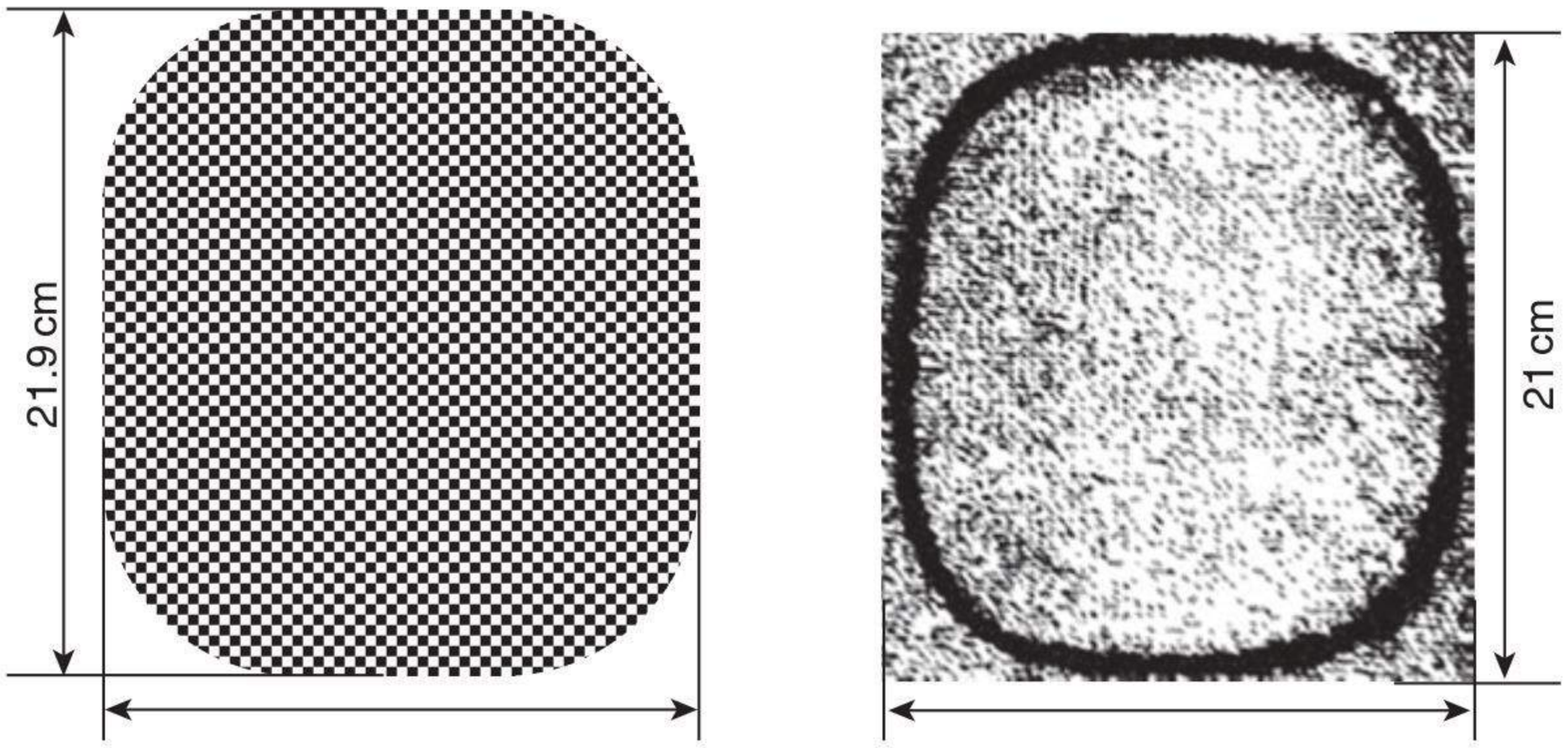

(a) Calculated results (b) Experimental results

7.16 Comparison between the calculated flat shape and the experimental one.

ment ($R = 7.5$ cm) are given. As far as Sample 1 TBMWK fabric is concerned, no wrinkles occur even at the equator area of the hemisphere. In Fig. 7.16(a), the calculated flat shape of the fabric (Sample 1) which can yield the hemisphere ($R = 7.5$ cm) is shown. It fits the experimental result (Fig. 7.16(b)) very well since the differences between them are only about 2% and 4% along the length and width directions respectively. The results for Sample 2 are similar to those of Sample 1.

According to the model established before, all crossover points on the 2-D fabric can be transformed to 3-D coordinates. Therefore, the local deformations, i.e. the local angle changes between the two bias inserting yarn systems, can also be predicted. In Fig. 7.17, comparisons between the calculated and measured local deformations are illustrated, in which the radius of the pressing hemisphere is 11 cm. As shown in Fig. 7.10, if the z-axis minus is described as the north direction, then Fig. 7.17(a) represents latitude 60°N, and Fig. 7.17(b) represents latitude 30°N. All calculated or measured angles are from the +45° inserting yarn system to the –45° inserting yarn system. It can be noted that the calculated local deformations fit the experimental ones very well.

7.8 Summary

Based on the characterization of the deformation behaviour of TBMWK fabrics during the hemisphere-pressing process, a model for predicting possible wrinkles as well as the flat shape of fabric that can yield the hemisphere was established. Comparison between the theory and the experimental results suggested that the model fits the experimental results very well.

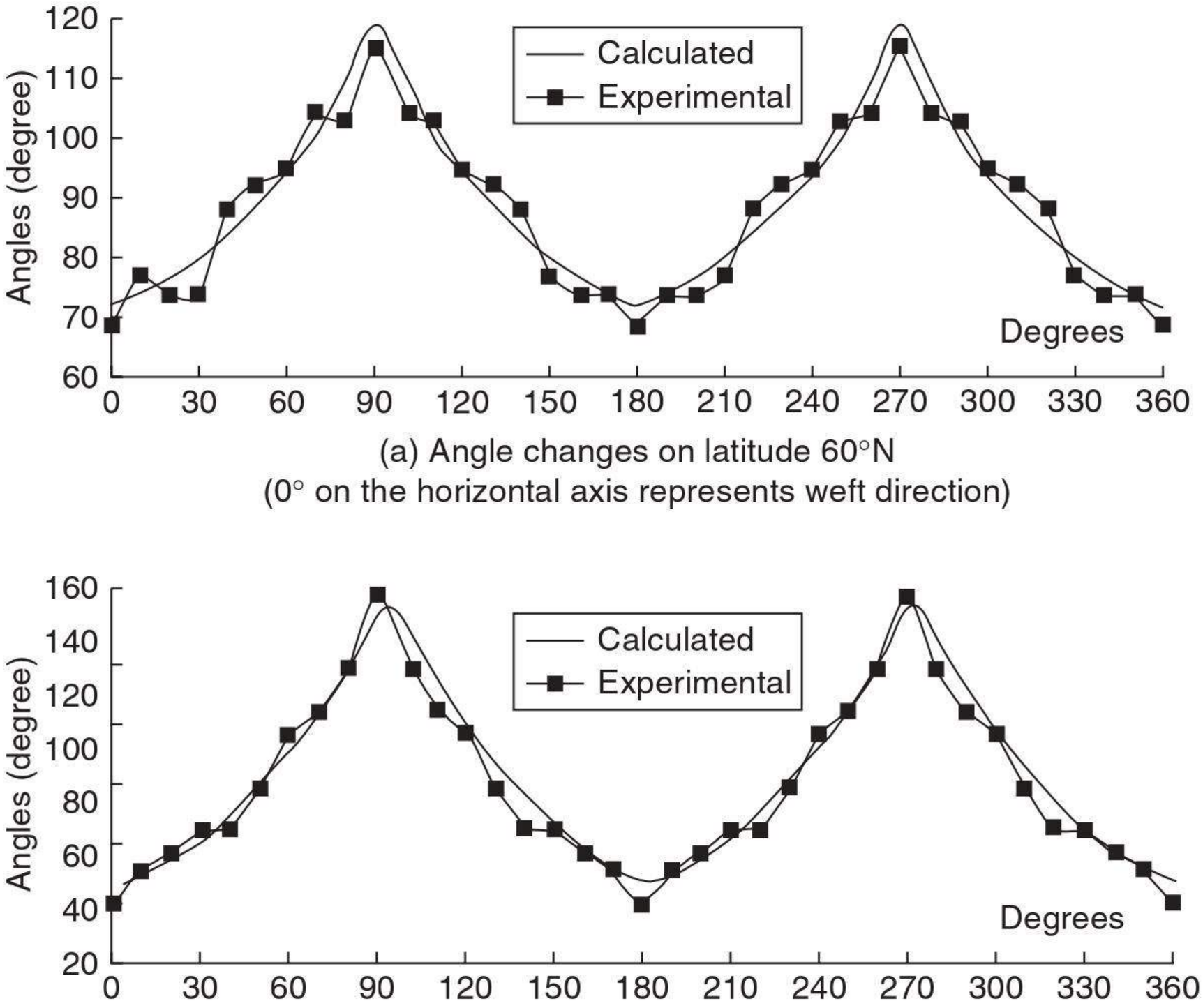

(a) Angle changes on latitude 60°N
(0° on the horizontal axis represents weft direction)

(b) Angle changes on latitude 30°N
(0° on the horizontal axis represents weft direction)

7.17 Comparisons between the calculated and measured local deformations.

It was found that the typical structure of MWK fabric does not possess satisfactory conformability, which is suitable for plate or low-curvature shell materials. TBMWK fabrics, however, possess much better conformability. It was noticed that the two bias inserting yarn systems tend to become gathered together always along the weft direction during the hemisphere-forming process, which is quite different from that of woven fabrics in which the yarns tend to orient along the ±45° directions. In addition, the angle between the two bias inserting yarn systems can reach nearly 0° during deformation; the woven fabrics, however, possess some locking angle, which is usually much larger than 0°.

An important phenomenon was found that the angles between the two bias inserting yarn systems in a TBMWK fabric along the weft direction during the hemisphere-forming process are basically linearly related to the perpendicular distances from the measured points to the longitudinal axis of the hemisphere, provided that the radius of the pressing hemisphere is larger than 7 cm. The larger the radius, the larger is the correlation coefficient (close to unity). The slope of the trendline is also linearly related to the magnitude of the radii of the pressing hemispheres, and the larger the

radius, the smaller the absolute value of the slope. In addition, the shape of flat TBMWK fabric that can yield the corresponding hemisphere is close to rectangular, not square as presented by the woven fabric. In addition, the predicted local deformations of a TBMWK fabric during the hemisphere-pressing process also fit the experimental results very well.

7.9 References

Amirbayat J and Hearle J W S (1989), The anatomy of buckling of textile fabrics: drape and conformability, *Journal of the Textile Institute*, **80**, 1, 51–70.

Aono M, Breen D E and Wozny M J (1994), Fitting a woven-cloth model to a curved surface: mapping algorithms, *Computer-Aided Design*, **26**, 4, 278–292.

Aono M, Denti P, Breen D E and Wozny M J (1996), Fitting a woven cloth model to a curved surface: dart insertion, *IEEE Computer Graphics and Applications (Computer Graphics in Textiles and Apparel)*, 60–69.

Bassett R J and Postle R (1990), Fabric mechanical and physical properties, Part 4: The fitting of woven fabrics to a three-dimensional surface, *International Journal of Clothing Science and Technology*, **2**, 1, 26–31.

Bergsma O K (1993), Computer simulation of 3D forming processes of fabric reinforced Plastics, *Proc. 9th Int. Conf. on Composite Materials (ICCM-9)*, 560–567.

Christie G R (1997), Numerical modeling of fibre-reinforced thermoplastic sheet forming, PhD Thesis, Department of Mechanical Engineering, University of Auckland.

Cogswell F N (1992), *Thermoplastic Aromatic Polymer Composites*, Butterworth-Heinemann, Oxford, UK and Boston, MA.

Duhovic M and Bhattacharyya D (2005), Deformation mechanisms in knitted fabric composites, in *Polymer Composites from Nano-to-Macro Scale* (ed. K Friedrich, S Fakirov and Z Zhang), Springer, New York, 265–288.

Heisey F L and Haller K D (1988), Fitting woven fabrics to surfaces in three dimensions, *Journal of the Textile Institute*, **79**, 2, 250–263.

Hu J, Jiang Y M and Ko F (1998), Modeling of bending properties of multiaxial warp knitted fabrics, *Textile Research Journal*, **68**, 11, 828–834.

Kaufmann J R (1991), Industrial applications of multiaxial warp knit composites, Chapter 5 in *High-Tech Fibrous Materials* (ed. Tyrone L Vigo and Albin F Turbak), American Chemical Society, Washington, DC, 81–89.

Krebs J E and Bhattacharyya D (1998), A direct comparison of matched-die versus diaphragm forming, *Composites, Part A*, **29**, 183.

Laroche D and Vu-Khanh T (1994), Forming of woven fabric composites, *Journal of Composite Materials*, **28**, 18, 1825–1839.

Lim T C, Ramakrishna S and Shang H M (1998), Improvement of knitted fabric composite sheet formability by simultaneous deep drawing and stretch forming, *First Asian–Australasian Conf. on Composite Materials (ACCM-1)*, **1**, 409.

Long A C (1994), A simulation of reinforcement deformation during the production of preforms for liquid molding processes, *I. Mech. E., J. Eng. Manuf.*, **208**, 269–278.

Mack C and Taylor H M (1956), The fitting of woven cloth to surfaces, *Journal of the Textile Institute*, **47**, 8, T477–T488.

Martin T A, Christie G R and Bhattacharyya D (1997), Grid strain analysis and its application in composite sheet forming, in *Composite Sheet Forming* (ed. D Bhattacharyya), Elsevier, New York, 217.

Mayer J, Haan J D, Reber R and Wintermantel E (1998), Knitted carbon fibre reinforced thermoplastics: An overview, *First Asian–Australasian Conf. on Composite Materials (ACCM-I)*, **1**, 401.

Mouritz A P, Bannister M K, Falzon P J and Leong K H (1999), Review of applications for advanced three-dimensional fibre textile composites, *Composites*, Part A, **30**, 1445–1461.

Robertson R E, Hsiue E S, Sickafus E N and Yeh G S Y (1981), Fiber rearrangements during the molding of continuous fiber composites. I. Flat cloth to a hemisphere, *Polymer Composites*, **2**, 3, 126–131.

Robertson R E, Hsiue E S and Yeh G S Y (1984), Fiber rearrangements during the molding of fiber composites. II. Flat cloth to a rounded cone, *Polymer Composites*, **5**, 3, 191–197.

Savci S, Curiskis J I and Pailthorpe M T (2000), A study of the deformation of weft knit preforms for advanced composite structures. Part 2: The resultant composite, *Composites Science and Technology*, **60**, 1943.

Takano N, Ohnishi Y, Zako M and Nishiyabu K (2001), Microstructure-based deep drawing simulation of knitted fabric reinforced thermoplastics by homogenization theory, *International Journal of Solids Structures*, **38**, 6333.

8

Permeability of multilayer woven fabrics

Abstract: In this chapter, a comprehensive study on the permeability modelling of multilayer woven (MLW) fabrics is presented. A framework for flow permeability measurement in resin transfer moulding is described. The Darcy law is used to model the flow through the reinforcement fibres where permeability is a measure of the resistance of the fibres to the flow. Two types of woven fabrics, one fabricated using monofilaments so as to eliminate the effects of other factors such as fibre bundle on the permeability, and the other by using multifilament yarns, are used for modelling. Two models are developed to explain the permeability of these two different varieties of multilayer woven fabrics.

Key words: multilayer woven (MLW) fabrics, permeability of MLW fabrics, Darcy's law, modelling permeability of MLW fabrics, fractal permeability model.

8.1 Introduction

Permeability is a geometric characteristic related to the structural features of the textile at several length scales. It is an important property that affects the comfortability of fabric. In the manufacture of composites with textile reinforcement, the permeability plays a key role (Guangbiao Xu and Fumei Wang, 2005). It is the most important parameter influencing the flow through the porous medium and relates the velocity of the flow to the pressure gradient within the medium. In other words, permeability is a measure of the ability of the resin to flow through the preform. In the Liquid Composite Moulding (LCM) process, such as Resin Transfer Moulding (RTM) and Reaction Injection Moulding (RIM), for fibre composites, the flow characteristics, such as the permeability and flow pattern, of the fibre reinforcements play a crucial role in the fill process and finished properties of the composites. Thus, if the permeability of the reinforcements can be acquired, the fluid progress and fill time during the injection process may be accurately predicted to obtain an artistically finished product with minimum void content.

The prediction of textile permeability is important due to the often encountered problems of non-uniform impregnation, which may even involve void and dry spot formation. Permeability can be highly directional (anisotropic), a serious concern for mould design in terms of the placement

of inlets, and vents, and is directly affected by the amount of compaction of the preform in the mould as well as the preform architecture.

One of the key issues in the manufacture of polymer composites is the resin infiltration of the fibrous preform. The resin transfer moulding (RTM) method is generally used to manufacture composite parts. In this method, the reinforcing fibres are placed in a mould cavity and the resin is injected to fill up the empty spaces. After the resin cures, the mould is opened and the part ejected. The resin must infiltrate the whole preform and displace the air between the fibres within the time limits dictated by its processing parameters and pressures limited by the equipment and mould design. This is not necessarily easy to accomplish. To predict the necessary pressures and filling times and the proper locations for the inlet ports for resin injection and of the vents for air ejection, it is necessary to model the resin infiltration process. A key to this modelling is permeability which characterizes the resistance of fibres to the flow of infiltrating resin.

It is apparent that the permeability of a textile preform (transport of resin) is a key aspect of fibre-reinforced plastic composite fabrication processes such as RTM. As one of the elemental performances of fibre materials, the importance of the permeability lies in the fact that, firstly, it can determine the filling and packing time in injection, and mould design, locate the injection port and exhaust port, thus becoming a critical parameter for numerical simulation; secondly, it can determine fluid flow attribute, and degree of impregnation, thus becoming a key factor in the manufacture of high-performance products.

Problems related to the permeability include the formation of dry spots or voids within the preforms. These dry spots and voids will have an adverse effect on the performance of products, so it is important to eliminate them. But this problem is not easy to solve, particularly when the preform is composed of multiple layers of reinforcement. Only after analyzing the relationship between fabric permeability and fabric construction is it possible to eliminate dry spots and voids to improve the performance of the products.

Studies of the permeability of textile preforms have been reviewed by Lee (1997) and Rudd *et al.* (1997). The preform permeability can be obtained by experiments, empirical and analytical equations, and numerical simulations (Skartsis *et al.*, 1992; Berdichevsky and Cai, 1993; Wang *et al.*, 1994).

For resin flow through the interstices and between layers of fibre beds, the Newtonian flows in macroscopically homogeneous domains were described originally by Darcy (1856), who developed the constitutive description by observing water flow through beds of sand. Application of Darcy's model to composite processes, from laminates to moulded materials, is widespread. The percolation flow is generally applied to thermosetting resins in autoclave (laminate) or liquid moulding processes.

The familiar Darcy model may be written $\bar{v} = \frac{-K}{\mu}\nabla P$, where v is the average fluid velocity, μ is the fluid viscosity, K is the permeability of the porous medium, and ∇P is the pressure gradient and can be written in tensorial form for anisotropic preforms, where up to three scalar permeabilities are required in the plane case. Such implementations thus require determination of the permeability or components of a permeability tensor, by experimental or theoretical means. In application to actual processing, various factors are commonly used to account for flow 'tortuosity', or circuitousness of the path that must be traversed to penetrate the material, the shape of the particles, material anisotropy, and the average volume fraction. Several modifications to Darcy's law have thus been proposed in the polymer processing arena and in other areas of fluid–structure interaction; for example, Kozeny (1927) treated a permeated porous medium as a bundle of capillary tubes and obtained a relationship to adapt Darcy's law to include capillarity effects with an empirical relation; Blake (1922) derived a similar expression. Carman (1937) modified Kozeny's work by defining S, the specific surface with respect to a unit volume of solid, instead of a unit volume of porous medium. The 'Kozeny–Carman relationship' arose through these sequential contributions. Carman experimentally determined a range of 'Kozeny constants' for a variety of packing schemes and geometries of reinforcements.

Such relations have commonly been used to model polymeric flow in composite materials in the last 20 years (Coulter and Guceri 1988). Williams *et al.* (1974) considered the flow of several fluids through aligned reinforcements, both dry and presaturated with liquid. They obtained higher permeabilities for saturated than for unsaturated reinforcement, as did Martin and Son (1986). Many authors since the late 1980s have specifically studied the permeability of fibrous preforms for liquid moulding. More recent work has focused on complex geometries. Rudd *et al.* (1996) established a 'permeability map' for complex geometries. Smith *et al.* (1997) related permeabilities of sheared fabrics to ply angle. Lai and Young (1997) related similar experimental data to a geometry-based flow model.

Other closed-form modifications to Darcy's law have been developed to relate volume fraction and geometric or empirical constants such as the maximum packing fraction to the permeability of a periodic medium comprised of parallel cylinders. Gebart (1992) derived an equivalent permeability based on the assumption of hexagonally arranged fibres. Cai and Berdichevsky (1993) extended a classic self-consistent approach, wherein a heterogeneous element was assumed to be embedded in an equivalent homogeneous medium. The homogeneous medium was constructed such that the total flow and dissipation energy remained the same. Use of a

no-slip boundary condition at the fibre surface and zero velocity gradient in the radial direction at the domain boundaries resulted in an equivalent permeability value. The improved self-consistent method took into account an additional parameter V_A, the maximum packing capacity of fibres, to increase the accuracy of the model.

Bruschke and Advani (1993) developed a closed-form solution for permeability by matching the lubrication solution for low porosities and an analytical cell model solution for high porosities. They found agreement between their hybrid, arrangement-specific closed-form solution and a numerical solution of the Navier–Stokes equations for flow around both hexagonal and square arrangements of cylinders (using a simulation package, POLYFLOW). Van der Westhuizen and Du Plessis (1996) used phase-averaged Navier–Stokes equations to calculate the permeability of representative unit cells, and reported agreement with experimental in-plane permeabilities. Their model did not assume any particular arrangement of fibres for longitudinal permeability, but used the maximum packing capacity for different arrangements of fibres to create an effective volume fraction for transverse permeability. Wang (1996) developed a similar relation for an array of rectangular packed fibres.

Computational fluid dynamics software can be used to solve the full Navier–Stokes equations to determine flow progression, although in practice this can be done only for small domains. Several workers have developed intermediate special-purpose codes to model fluid flow in fabrics that account for effects such as capillarity, race tracking, saturation, etc. For example, Advani and co-workers developed 'LIMS' (Pillai and Advani, 1998), which is able to simulate edge effects by implementation of a mass sink to the continuity equation to account for saturation. Chang and Hourng (1998) developed a two-dimensional model for tow impregnation, taking into account micro/macroscopic flow and void formation. Ambrosi and Preziosi (1998) developed a model for flow dynamics in an elastically deforming environment.

Flow in tows versus gaps or voids has been specifically studied by a number of workers. Shih and Lee (1998), for example, used six different types of glass fibre reinforcements to determine the effect of fibre architecture on apparent permeability. The reinforcements included four-harness woven, plain weave, random fibre and stitched fibre mats. They argued that the gap size between the tows and the connectivity of the gaps control permeability. Kolodziej *et al.* (1998) proposed a theoretical model which accounted specifically for gaps as caverns or fissures inside the bundle of fibres. Both diameter of fibres and also diameter of gaps inside the fibre bundles were incorporated in the model. They reported that tow heterogeneity can decrease or increase tow permeability, depending on the critical dimensionless radius of these gaps. Heterogeneity was identified as the

probable cause of deviation of permeabilities from permeability models, which assume uniformity inside the fibre bundles.

The numerical simulation is usually made by the finite element analysis (Berdichevsky and Cai, 1993), finite difference (Gebart, 1992) and control volume methods (Lee, 1997) for idealized and/or simple preform structures. Regarding woven fabric, Rebenfeld and his students investigated the effective permeability in terms of the pore structure, weave type, fabric layering, fibre orientation and compressibility. When considering the heterogeneity, the combination of Navier–Stokes and Darcy equations with different permeability for flow in different portions of a preform extended to complicated fabrics (Lee, 1997).

The flow through multilayer assemblies is complex. Adams and Rebenfeld (1991) found that the permeability of multilayer assemblies differed from those of their constituent layers. In the homogeneous assemblies, the interlayer pores can increase the effective in-plane permeability, while in heterogeneous assemblies the permeability and anisotropy are governed by high-permeability layers or directions. They suggested a transverse flow mechanism to fill the low-permeability layers and keep the fluid front macroscopically uniform. Mogavero and Advani (1997) investigated the effect of varying the order of lay-up of a fixed number of plies and the impact of varying the thickness of individual layers. Batch and Cumiskey (1990) investigated the interface between layers in relation to compressibility and developed a model for calculating average volume fraction for multilayer assemblies, where it was found that increasing the number of layers decreased the permeability. They attributed this to the blocking at the interface of adjacent layers, which created tortuous flow paths. Loos *et al.* (1991) studied the permeability of carbon multiaxial warp knit preforms. It was found that the introduction of through-thickness fibres significantly increased the permeability of the preforms, especially for the preforms with high volume fraction. The Kozeny–Carman equation was found to be adequate to provide a quantitative relationship between permeability and the preform porosity. But the through-thickness fibres here are still different from those in 3-D multilayer woven fabrics.

Lekakou *et al.* (1996b) investigated the relationship between the compressibility and flow permeability of woven fabric assemblies. Multilayer assembly here means separate single-layer woven stacks. The interface is related to the sloughing or nesting (Mogavero and Advani, 1997), which is different from the stitching in integrally woven multilayer assemblies. Ko and Du (1997) reported that stitching in multiaxial warp-knitted fabrics can increase the fabric permeability, but the stitching here is still different from that in 3-D multilayer assemblies.

A large body of literature exists about the effects of fabric structures on permeability. For 3-D multilayer woven fabrics, the key feature of stitched

fabric is its interbundle stitches, but very limited information is available on the relationship between permeability and the effect of stitches. Shih and Lee (1998) proposed a parallel permeability model for flow through bidirectional stitched fabrics. The flow between the bundles is set by the Kozeny–Carman equation, and the effect of stitching was not specially mentioned. Cairns *et al.* (1999) developed a model that incorporates Darcy's law in fibrous bundle regions and the channel flow equations between bundles. This paper reported that two experimental systems, the stitched ±45 system and the stitched ±45/0 system, cannot be predicted well by using the presented model. Cairns *et al.* suggested that the permeability parameters needed to be re-evaluated with some account for the extensive stitching that was presented in these preforms. Loos *et al.* (1991) studied the permeability of carbon multiaxial warp-knitted preforms. It was found that the introduction of through-thickness fibres significantly increased the permeability of the preforms, especially for preforms with high volume fraction. The Kozeny–Carman equation was found to be adequate to provide a quantitative relationship between permeability and preform porosity.

Lundström (2000) also proposed a model for non-crimp stitched fabrics through theoretical analysis. It has been found that the flow in the interbundle channels was the most important and that the bundle flow could be neglected in computations of the overall flow rate and consequently also with regard to the permeability. The results showed that the permeability of the fabrics varied considerably as a function of the direction of infiltration, although the geometrical variations were small. In the production direction of the fabrics the permeability was generally two to three times higher than it was in the perpendicular direction. On the other hand, the spread of the results between several samples was always measured to be higher in the high flow direction. The experiments also revealed that a choice of larger bundles in a fabric did not necessarily result in a higher permeability. The proposed simple model works well for certain cases, while it overrates the permeability in other cases. This suggests that if the real fabric should have the same geometry as the model, its permeability would be higher. Therefore, it is really significant and urgent to carry out a quantitative study on the question of how the inter-layer stitching affects the effective permeability. Such a study will be very helpful for the rational design of the stitched fabrics, the exact pre-simulation of the moulding process, and the global optimization of the processing parameters.

In this chapter, a comprehensive study on the permeability modelling of multilayer woven fabrics is presented. A framework for flow permeability measurement in resin transfer moulding will be described. The Darcy law is used to model the flow through the reinforcement fibres where the permeability is a measure of the resistance of the fibres to the flow. Two types

of woven fabrics, one fabricated from monofilaments so as to eliminate the effects of other factors such as fibre bundle on the permeability, and the other made by using multifilament yarns, have been used for modelling. Two models were developed to explain the permeability of these two different varieties of multilayer woven fabrics.

8.2 Fabric compressibility

Compressibility of preforms is of importance in the RTM process, wherein mould closing force and attainable fibre volume fraction are directly dependent on the fabric compressibility (Padaki *et al.*, 2006). Fabric compressibility is very important in all RTM processes, and affects both the material and processing properties of the part. As the fabric is compressed by fluid pressure or the mould surface the fibres get compacted and the fibre volume fraction increases. This decreases the thickness of the part, decreases the permeability, and decreases the porosity. Compressibility is possibly a more important concept in one-sided moulding processes than in closed-mould processes. In a closed-mould process the permeability and fabric thickness are fixed at a certain value which is determined by the mould gap. Throughout the process the permeability is constant and independent of the injection pressure. In one-sided moulding processes the compaction of the fabric can lead to several important phenomena. In processes where the flow is in the plane of the fabric such as VARTM and SCRIMP™, a part with non-uniform thickness can be created since the net compaction pressure varies throughout the mould.

In processes where the resin is forced though the thickness, the pressure applied to the fluid is also the pressure compacting the fabric. Therefore, the permeability and fabric thickness can change throughout a process and can depend on the pressure at which the process is taking place. This can create an interesting competing mechanism in these types of processes. According to Darcy's law, an increase in pressure will increase the velocity of the fluid though the fabric. However, increasing the pressure of the fluid will increase the compaction pressure and lower the permeability. It could be possible in certain cases for an increase in pressure to increase injection time, although this is not common. For most fabrics the decrease in thickness tends to compensate for the decreased permeability in through-thickness flow. The effect of compaction on permeability is very dependent on the fabric architecture, which means some fabrics are more affected than others.

Fabric compaction also affects the porosity of the fabric, which will affect the saturation time for unsaturated flow. This fact adds yet another complication to the problem. Although permeability decreases with compaction, the decrease in porosity can increase the velocity of the fluid through a

preform. Decreasing the porosity also increases the capillary pressure. However, in most cases these effects are minor.

As a fabric is compressed there are three distinct regimes that have been identified. The first is where the spacing in the fabric caused by the stitching and weaving is compressed. This occurs at very low pressures, and results in fibre-on-fibre contact. This region is also very linear in nature. In the second regime, both the solid and the voids are compressed. This is the most complex region, and is the most studied. Very complex models have been generated to predict the behaviour of the fabric in this region. Although the fibres are touching, they are still moving due to fibre bending, slippage and nesting. The third region is where the fabric has been fully compressed. Most fabrics are fully compressed with 1–2 MPa pressure. In the third regime, all the fibres have been manipulated into a stable position and cannot be moved any further. The only compression occurring in this regime is due to the solid material compressing. Many fabrics have compressed to half their original thickness by this point.

8.3 Permeability testing

The permeability characterizes the porous material in terms of resistance to the fluid flow for a given injection pressure. The greater the value of permeability, the faster the resin permeates through the fibrous reinforcement. In the case of an isotropic fabric, the permeability tensor reduces to a single scalar. The most general situation of orthotropic reinforcement requires three values, k_1, k_2 and k_3, for the permeability in the principal directions of the material. However, most RTM moulded parts are thin shells and the preform does not consist of a multilayer reinforcement. So it is not always necessary to determine the through-thickness permeability k_3. Hence it is essential to measure the first two principal permeabilities, k_1 and k_2, the so-called in-plane permeabilities (Ferland *et al.*, 1996).

For flow through the fabric, it is extremely difficult to calculate the permeability constant (K) by knowing only the geometric information. Micro-models exist for estimating the permeability of a fabric given fibre diameters, fibre spacing and other relevant information (Simacek and Advani, 1996; Cairns *et al.*, 1999). However, these models are very complex and have varying accuracy. In addition, tests must still be performed in order to determine some of the parameters needed as input to the models. The most accurate and direct way to determine the permeability is through testing. By knowing the velocity, the pressure drop, and the viscosity of a fluid moving through a fabric, the permeability can be calculated. Because most RTM modelling has been done for closed-mould processes, the permeability in the plane of the fabric was typically of the greatest concern (Adams and Rebenfeld, 1991; Ferland *et al.*, 1996; Lai and Young, 1997).

For this reason, the majority of available permeability data is for flow in the plane. For the two-stage processes such as pressure bag moulding, the most important value is the permeability through the thickness. This is because the distribution channel covers the surface of the fabric, so all the in-plane flow occurs in the channel and the flow in the fabric is primarily though the thickness. For a process such as SCRIMP™ where there may be a large spacing between the flow channels, the in-plane permeability would be more important. The in-plane permeability can be either higher or lower than the through-thickness value, depending on the fabric type and compaction pressure. Parnas *et al.*, have found that in general the in-plane permeability in the direction of the fibres is 6–8 times larger than it is in the through-thickness direction (Parnas and Salem, 1993). However, if the flow in the plane is transverse to the fibres, the permeability could be expected to be close to the through-thickness value or possibly even less.

8.3.1 Saturated vs. unsaturated flow

Darcy's law was originally intended for modelling saturated flow of water through soil (Darcy, 1856). Because of this, it has some deficiencies when modelling unsaturated flow though a fabric. In order to use it to model this type of flow it must be modified slightly. In calculating the permeability, the velocity is determined by dividing the flow rate by the cross-sectional area. The area used is the total flow area of the fabric. This means that the velocity in Darcy's law is the superficial velocity, or the velocity averaged over the whole area. Due to the presence of the fabric, the actual flow area is less than the total area. This means that the actual velocity of the fluid through the preform is higher than the superficial velocity because the flow area is reduced. This reduction in flow area can be determined by knowing the fibre volume fraction of the fabric. Actually, the term commonly used is called the porosity (e) of the fabric which is one minus the fibre volume fraction. The modified equation becomes:

$$v_{\text{actual}} = -\frac{k}{\mu_e}\frac{\mathrm{d}p}{\mathrm{d}z}$$

Another additional term required to model unsaturated flow is the capillary pressure. This is a consequence of the wicking behaviour of the fabric caused by surface tension. This tends to pull the resin along, which results in a higher apparent pressure than the applied pressure. The $-\mathrm{d}P$ term will be replaced by ΔP, recognizing that the pressure drop is linear, and that the flow occurs from high to low pressure. Darcy's law is modified accordingly.

$$v_{\text{actual}} = -\frac{k}{\mu_e}\frac{\left(\Delta P_{\text{app}} + P_{\text{cap}}\right)}{\mathrm{d}z}$$

where:

ΔP_{app} is the drop in fluid pressure
P_{cap} is the capillary pressure.

The capillary pressure is dependent on properties of the fabric and the resin. One equation for determining the surface tension as presented is:

$$P_{cap} = \frac{F}{D_f}\frac{1-e}{e}\sigma\cos\theta$$

where:

F is the form factor
σ is the surface tension
D_f is the diameter of a fibre
$\cos\theta$ is the wetting angle.

The fibre diameter, porosity and form factor are all properties of the fabric, while the surface tension is a property of the resin. The wetting angle is a property of the resin and fabric. Its value can vary depending on the measurement method. For the most accurate results in an infusion process, the dynamic contact angle is the most appropriate (Skartsis *et al.*, 1992). It is measured as the fluid is moving in relation to the solid interface. Both an advancing and a receding angle can be determined. However, the static contact angle gives a very good approximation for the resin systems used in RTM, and is easier to measure. Fortunately, the wetting angle depends only on the fabric material and not on the fabric architecture. Therefore, once the fabric properties are known for a given fabric, the capillary pressure can be calculated for any resin with that fabric if its surface tension and wetting angle are known. The form factor depends on the fabric architecture and whether the flow is along the fibres or transverse. Transverse flow typically has a form factor with a value from 1 to 2. The porosity is included because as the porosity decreases, the surface area to volume ratio increases, which increases the capillary pressure. Capillary pressure is not very temperature dependent, since both the contact angle and surface tension are very weak functions of temperature.

Although the capillary pressure is typically much smaller than the injection pressure, it can change the results of a test by a noticeable amount. Some researchers have claimed that the capillary effect was negligible in their permeability tests while others have claimed capillary pressures had a significant effect (Parnas and Phelan, 1991). The extent of this effect is going to vary depending on the fabric, the resin and the injection pressures. Previous researchers have conducted a study on the capillary pressures of a silicone oil and a corn syrup with a couple of fabrics. The largest capillary pressure they found was approximately 5 kPa for the silicone oil and less for the corn syrup, although they did not give a specific value.

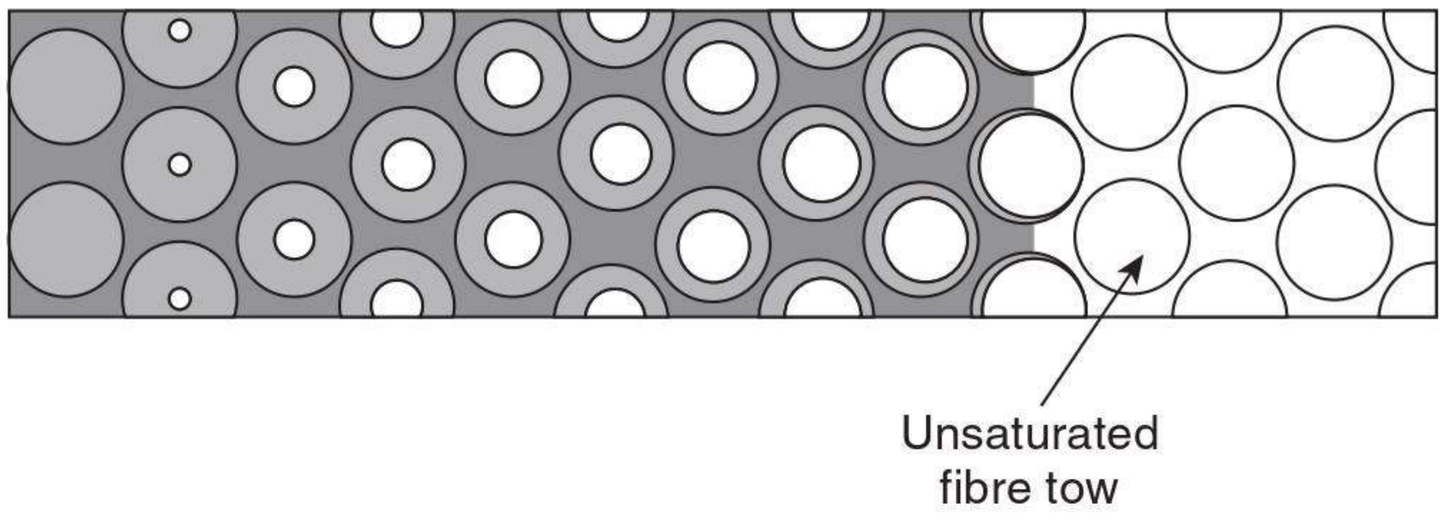

8.1 Illustration of dual-scale flow.

Another phenomenon of unsaturated flow arises from the fact that there is flow occurring between the fibre tows as well as within them. During a saturated permeability test, the flow in both these regions is factored into the total permeability. Because of the presence of macroscopic channels between tows and microscopic channels within them, a fabric is commonly referred to as a dual-scale porous medium. The consequence of this dual nature in unsaturated flow is that the flow in the macroscopic channels will advance much faster than the inside of the tows can be saturated. Cairns *et al.* (1999) found that the equivalent permeability of the channels between tows could be an order of magnitude larger than the permeability within the tow. This effect is shown in Fig. 8.1.

This can be a problem in modelling as well as for part quality and the effect on flow modelling is minor. This is mostly due to the fact that this occurs only at the flow front, and not in the saturated regions. It was determined, however, that this could have a large impact on part quality. This is why the use of a vacuum pump has become so critical in reducing porosity in RTM processes. The use of a vacuum reduces the amount of air that is trapped as the resin encircles a fibre tow.

8.3.2 Permeability as a function of weave type

There are hundreds of possible woven fabric combinations, which can be divided into biaxial and triaxial woven structures according to in-plane fibre orientation. The plane weave has the highest frequency of yarn interlacing, whereas the satin weave has the least, with the twill weave somewhere in between. Accordingly, woven fabrics have a higher level of structural integrity and greater ductility due to the crimp geometry produced by yarn interlacings. On the other hand, the satin weave has the highest level of fibre to fabric strength and modulus translation efficiency, due to the low level of yarn interlacing and yarn linearity. The low level of yarn integration in satin weave also allows freedom of yarn mobility, which contributes to higher fibre packing density and consequently a higher level of fibre volume fraction (Ko and Du, 1997). Open weave results in higher porosity and

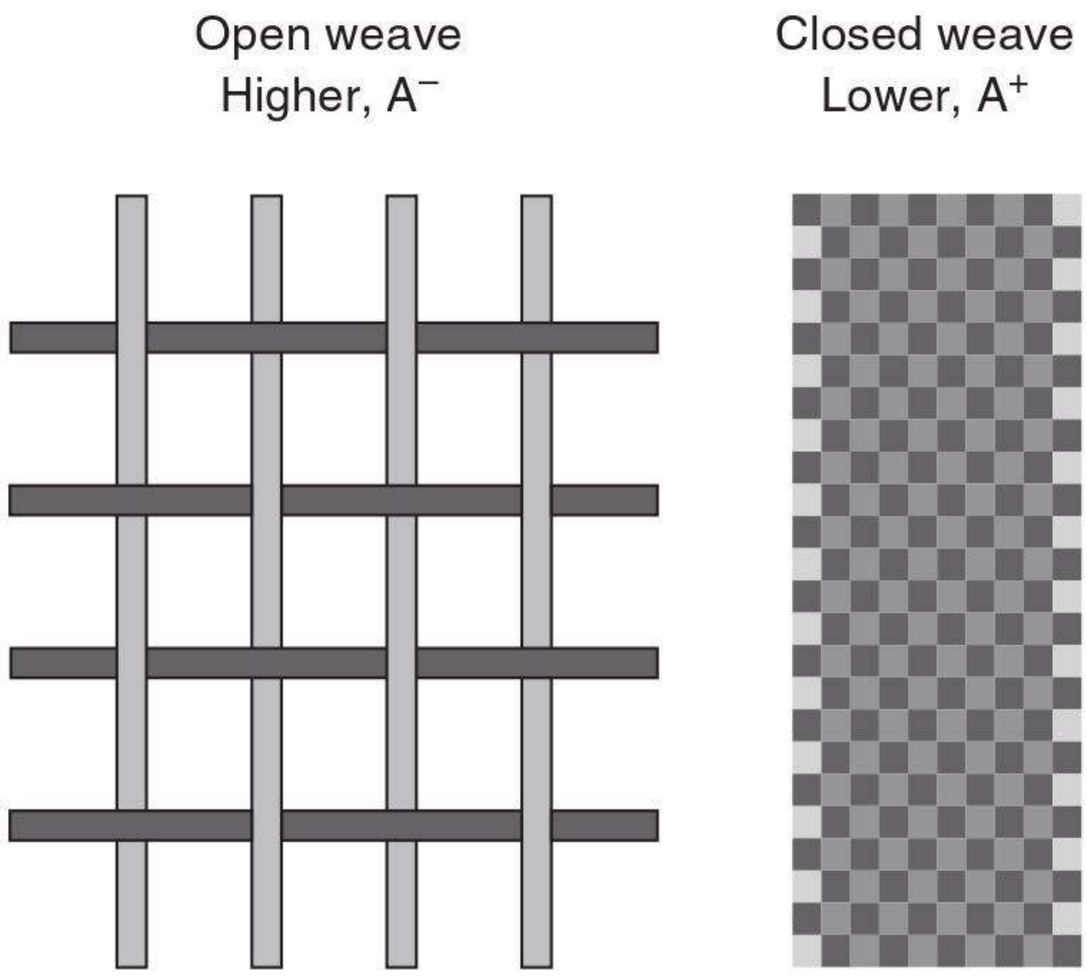

8.2 Difference between open weave and closed weave.

higher permeability. However, closed weave mats are difficult to penetrate, but offer relatively higher strength and module. For the 3-D multilayer woven fabric, the more porous or open preform structures have higher values of permeability and can be more easily filled. The difference between open weave and closed weave is shown in Fig. 8.2.

8.3.3 Direction of permeability measurement

The permeability tensor is represented by its components K_{xx}, K_{yy}, as the in-plane permeabilities, and K_t, as the transverse permeability (Advani and Calado, 1996). It is understood that effective (or directional) permeability in three dimensions follows the shape of an ellipsoid. Six independent measurements are required to determine the permeability tensor.

The first channel flow experiment to measure principal permeability was conducted in an arbitrary coordinate system x, y, z along the x-axis (Weitzenböck *et al.*, 1999b). For the permeability, there is some directional character in such anisotropic preforms, and three values for the permeability may be required: K_{xx}, K_{yy} and K_{zz}. In isotropic preforms, one value is sufficient: $K = K_{xx} = K_{yy} = K_{zz}$. The directional characteristics of K_{xx}, K_{yy} and K_{zz} are shown in Fig. 8.3.

8.3.4 Isotropic and anisotropic permeability

For isotropic materials a circular flow front can be observed in the radial flow experiment, while for anisotropic materials the flow front becomes elliptic.

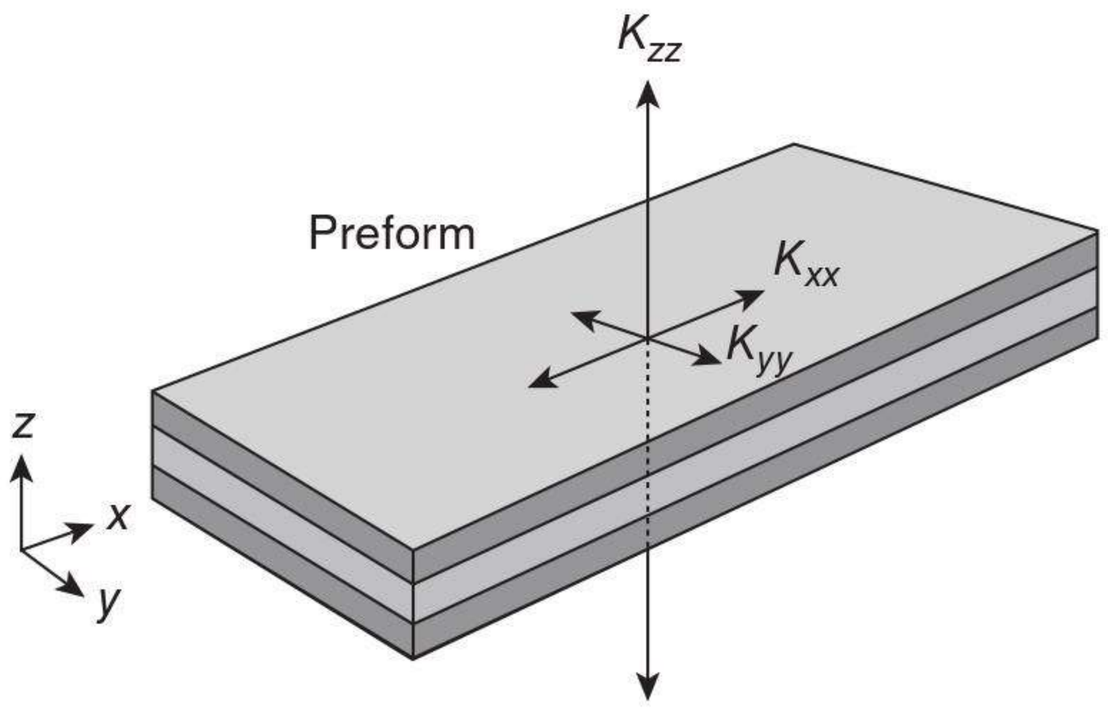

8.3 Directional characteristics of K_{xx}, K_{yy}, K_{zz}.

Isotropic permeability

To calculate isotropic permeability the pressure gradient within the mould has to be determined as a function of the flow front position. This is achieved by solving the Laplace equation in polar coordinates (Weitzenböck *et al.*, 1999a). If a preform is isotropic in the in-plane directions such that $K_{xx} = K_{yy}$, then the flow fronts progress as circles. Some fabrics, such as random fibre mats, four-harness woven fibreglass mat and symmetric bidirectional fabrics, produce isotropic preforms.

Anisotropic permeability

So far only flow in isotropic porous materials has been considered. However, for many fabrics commonly used in RTM an elliptical flow front is observed. As a consequence the second-order partial differential equation of the pressure distribution is no longer a Laplace equation, where K_{xx} and K_{yy} are two principal permeabilities (Weitzenböck *et al.*, 1999a). If the preform is anisotropic in the plane with K_{xx} different from K_{yy}, the flow fronts become elliptic and remain elliptic throughout filling. Furthermore, this situation can be encountered with unidirectional stitched mats.

8.3.5 Measurement of permeability

Generally speaking there are two different configurations for permeability measurement. These are the one-dimensional channel flow experiment and the two-dimensional radial flow experiment. For isotropic materials a circular flow front can be observed in the radial flow experiment, while for anisotropic materials the flow front becomes elliptic. The main attraction of the radial flow experiment is that both the principal permeability values

and their orientation can be determined in a single experiment; in addition, no racetracking occurs during the experimental process, so it is widely used by researchers (Adams *et al.*, 1986; Hirt *et al.*, 1987; Chan and Hwang, 1991; Parnas and Salem, *et al.*, 1993). For constant inlet pressure three algorithms to calculate permeability data from flow front measurement have been developed (Adams *et al.*, 1988; Carter *et al.*, 1995; Rudd *et al.*, 1995). In all these approaches the orientation of the flow front ellipse needs to be determined visually, since the algorithms apply only to flow front measurements along the principal axes. For all methods permeability is assumed to be a symmetric tensor. As a consequence there is a set of two mutually orthogonal axes where all the off-diagonal tensor components become zero.

8.4 Monofilament permeability model

8.4.1 Characterization of pore microstructures

The permeability is a function of the preform architecture, pore structure and porosity, and different types of fibre preforms may have substantially different permeability at the same fibre volume fraction. The micrograph of fibre preform reveals considerably complicated microstructures of multilayer woven fabrics. However, our experimental data showed that the vari-ation in the alignment of the fibre layers and the pore size distribution was regular. Thus it is possible to find an analytical solution for permeability based on the concept of a unit cell.

Figure 8.4 displays the top view of the three types of multilayer woven fabrics fabricated by the monofilaments. Each fabric has five layers in total,

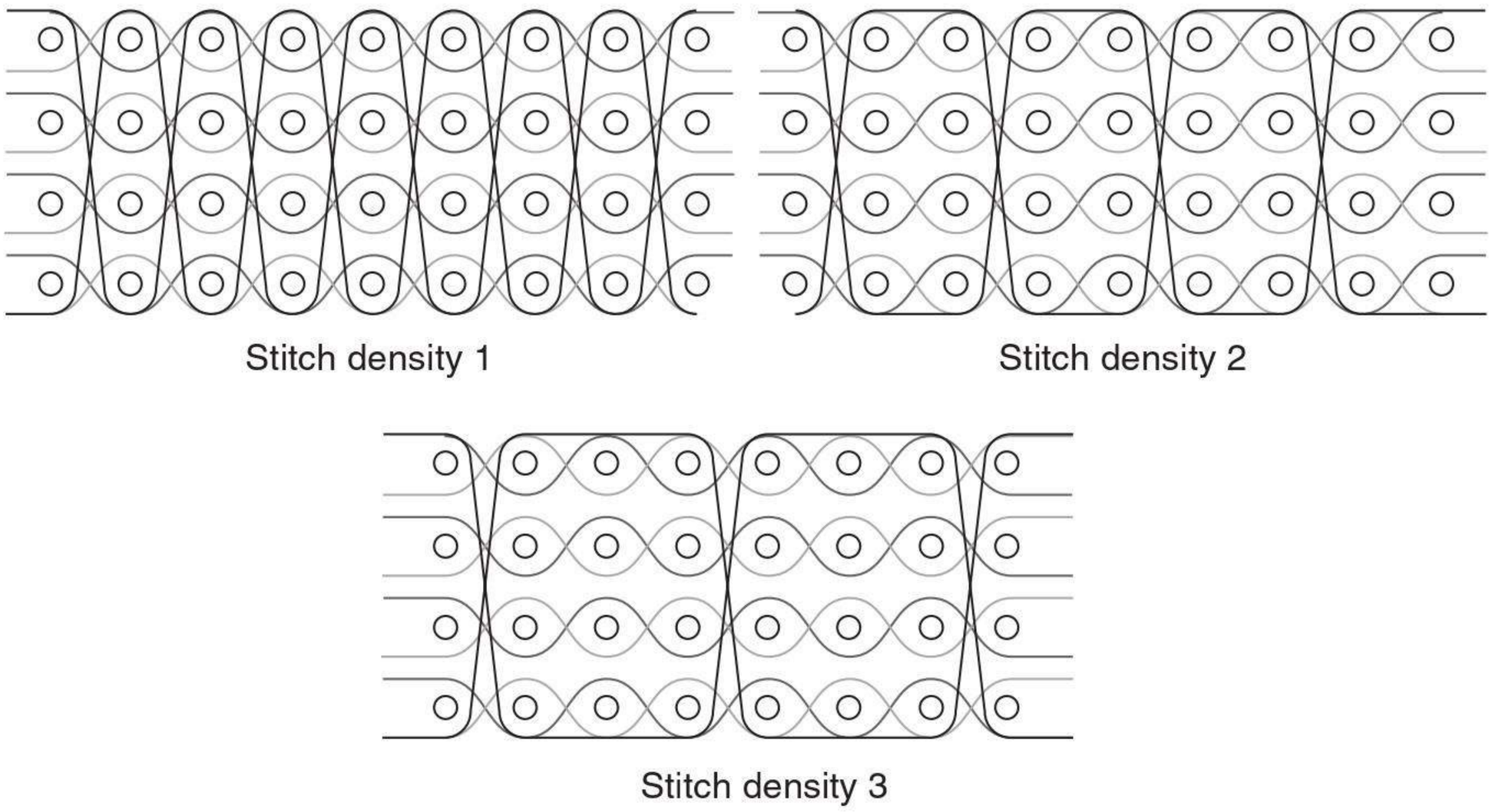

8.4 Schematic for three different stitch models of multilayer woven fabrics.

a layer being defined as containing both a warp and a weft yarn. All weaves are designed as plain weaves and weft yarns are used as stitches to interconnect adjacent layers. The differences between these designs are in the stitching density.

8.4.2 Permeability model of unit cell 1

From the cross-sectional view of three types of multilayer woven fabrics (Fig. 8.5), the structure of the preform can be idealized as a porous medium consisting of parallel fibres as shown in Fig. 8.6. Based on the assumption that the major contribution to the flow resistance comes from the narrow gap between the fibres, the permeability model therefore can be established as follows.

The fibres are arranged in a periodic pattern so that we only need to consider the flow in one 'representative unit cell'. The pattern that we are

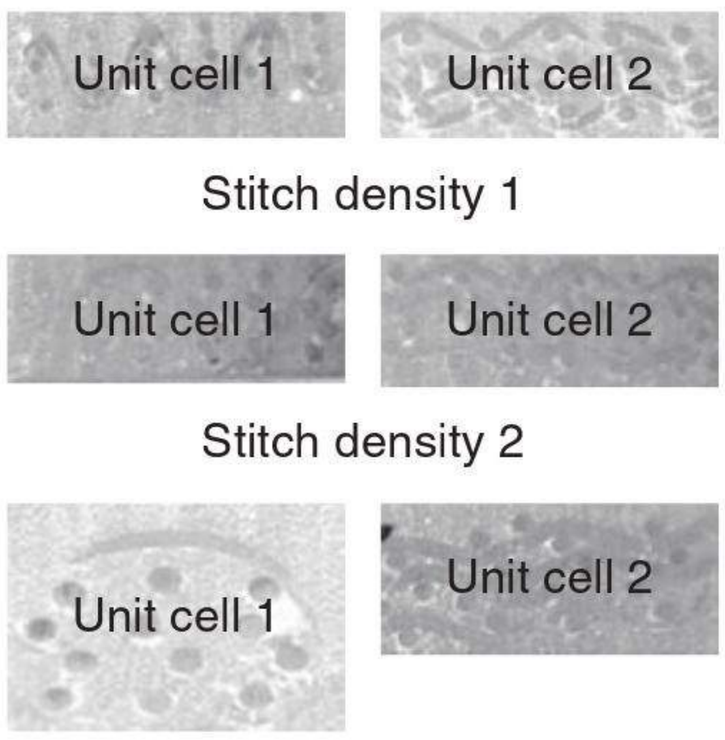

8.5 Cross-sectional view of three types of multilayer woven fabrics with different stitch density.

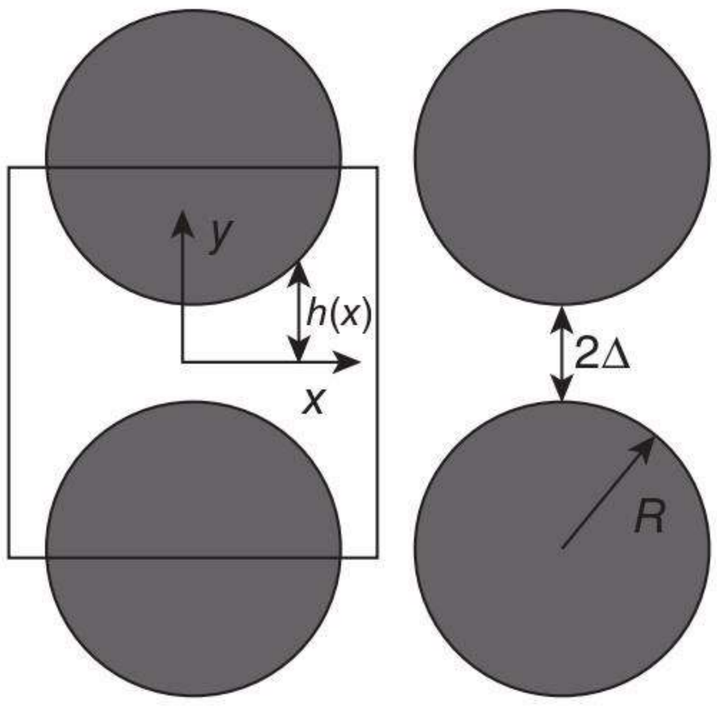

8.6 Definition sketch of the idealized monofilament reinforcement arrangement and the representative unit cell of quadratic fibre packing.

going to consider is the quadratic array. Let us assume that most of the resistance to flow which is perpendicular to the fibres comes from a small region close to the narrow gap formed between the fibres. If the fibres are very close to each other they form a channel with slowly varying area between them. Here we mean that the angle between the channel wall and the channel centre-line is small at all points along the channel (Liu Yi, 2006).

For the flow in the slow-varying channels, the cross-sectional area varying along the streamline direction is assumed to alter so slowly that inertia effects can be neglected (in the present case this is true for all geometries, since generally in RTM the Reynolds number of the resin is very small). If a constant pressure difference is maintained between two stations, the pressure gradient will vary slowly in the streamline direction:

$$\frac{\mathrm{d}p}{\mathrm{d}x} = -\frac{3}{2}\frac{\mu q}{h^3(x)} \qquad 8.1$$

where $h(x)$ is the half-height of the channel, p is the pressure, μ is the viscosity of the fluid q is the total flow rate. The total pressure drop between two stations a and b in the channel can be found from integration of Equation 8.1:

$$p_\mathrm{b} - p_\mathrm{a} = -\frac{3}{2}\mu q \int_\mathrm{a}^\mathrm{b} \frac{\mathrm{d}x}{h^3(x)} \qquad 8.2$$

From the definition sketch (Fig. 8.7) over the coordinate system and the channel half-height, the $h(x)$ needed in the integral can be calculated by:

$$h(x) = \Delta + R\left(1 - \sqrt{1 - \frac{x^2}{R^2}}\right) \qquad 8.3$$

which for $x << R$ can be written as

$$h(x) = \Delta + \frac{R}{2}\frac{x^2}{R^2} \qquad 8.4$$

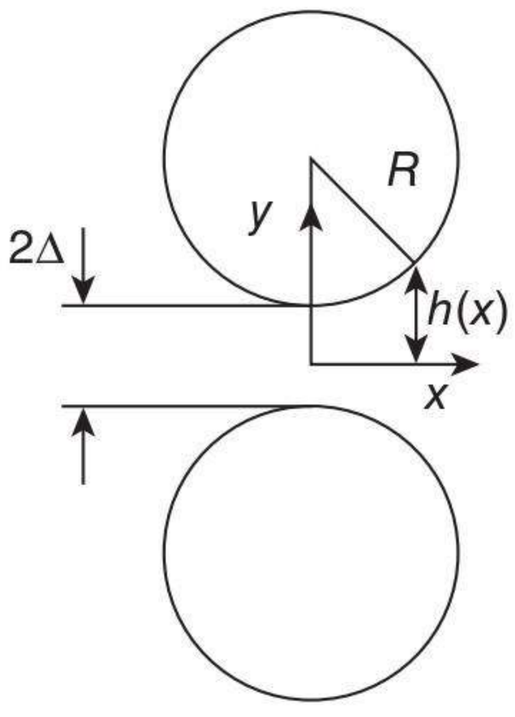

8.7 Definition sketch in the analysis of the flow between the fibres.

Substitution of $h(x)$ into Equation 8.2 gives

$$p_b - p_a = -\frac{3}{2}\mu q \int_a^b \frac{dx}{\left[\Delta + R\left(1 - \sqrt{1 - \frac{x^2}{R^2}}\right)\right]^3} \quad 8.5$$

By integrating the above integral equation and making some simplification based on the boundary conditions, we can get the following equation:

$$p_b - p_a = -\frac{9\pi}{16}\frac{\mu q}{\Delta^3}\sqrt{2R\Delta} \quad 8.6$$

which means that the pressure drop between two fibres in general can be written as:

$$\frac{\Delta p}{L} = -\frac{9\sqrt{2}\pi}{16L}\frac{\mu q}{R^2}\left(\frac{\Delta}{R}\right)^{-5/2} \quad 8.7$$

Comparing Equation 8.7 with the Darcy law, we can get the equation to calculate the permeability of the porous medium:

$$K_1 = \frac{16}{9\pi\sqrt{2}}\left(\frac{\Delta}{R}\right)^{5/2} R^2 \quad 8.8$$

Equation 8.8 can be rewritten in terms of fibre volume fraction if we notice that the fibre volume fraction can be calculated by:

$$V_f = \frac{\pi/4}{(1 + \Delta/R)^2} \quad 8.9$$

from which we see that Δ/R is given by

$$\Delta/R = \sqrt{V_{f,max}/V_f} - 1$$

where $V_{f,max}$ is the maximum fibre volume fraction which is achieved when the adjacent fibres touch each other (Liu Yi, 2006). Substitution of Δ/R in Equation 8.8 finally yields:

$$K_1 = \frac{16}{9\pi\sqrt{2}}\left(\sqrt{\frac{V_{f,max}}{V_f}} - 1\right)^{5/2} R^2 \quad 8.10$$

8.4.3 Evaluation of $V_{f,max}$

The maximum fibre volume fraction in the permeability expression of Equation 8.10 corresponds to the maximum space occupied by the fibres in the preforms. The architecture of the multilayer woven fabrics considered in the study consists of a layer to layer interlacement. For this architecture,

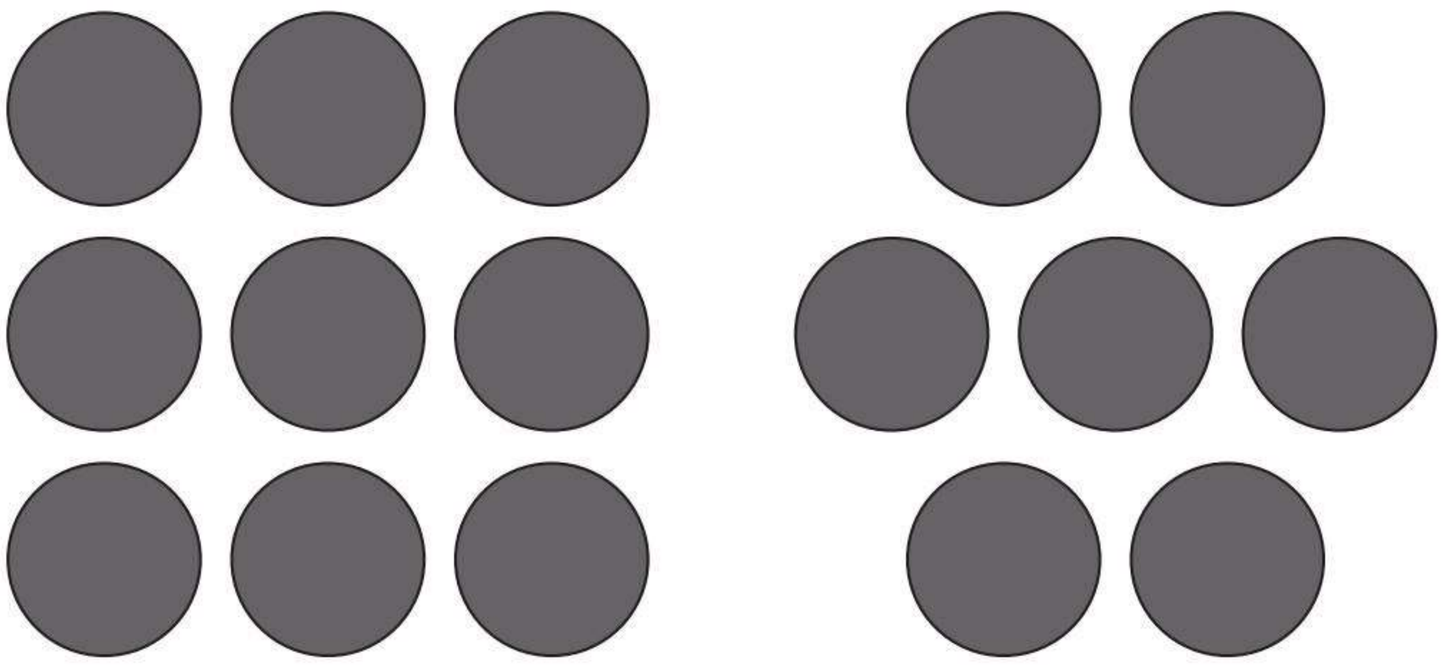

8.8 Definition sketch of quadratic and hexagonal arrays.

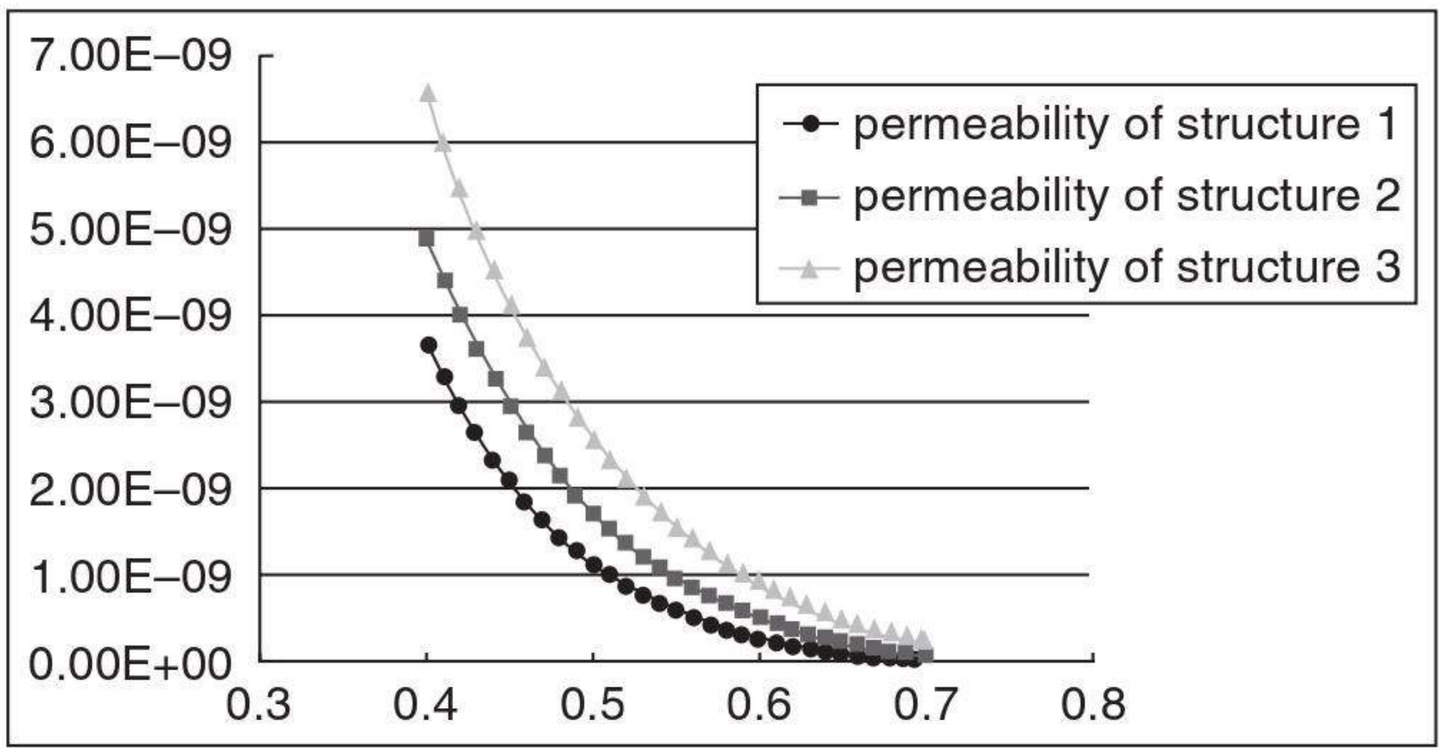

8.9 Permeability of three different structures of unit cells.

the maximum fibre volume fraction of these different stitch structures may be considered to vary from the quadratic array of Fig. 8.6 to the hexagonal array shown in Fig. 8.8.

For the quadratic array, the maximum fibre volume fraction is $\pi/4$; for the hexagonal array, the maximum fibre volume fraction is $\pi/2\sqrt{3}$. However, in this experiment, the maximum fibre volume fraction of the unit cell may be between these two values. A coefficient, C_f ($1 \le C_f \le 2/\sqrt{3}$), is thus introduced to define the maximum fibre volume fraction $V_{f,max} = C_f \cdot \frac{\pi}{4}$. If the coefficient $C_f = 1$, this means that the fibres in the unit cell from a quadratic array, and if $C_f = 2/\sqrt{3}$, the fibres are arrayed in a hexagonal model. As shown in the experimental cross-images, for the structure of stitch density 1, $C_f = 1$; for the structure of stitch density 3, $C_f = 2/\sqrt{3}$; for the structure of stitch density 2, $C_f = 1.1$.

8.4.4 Predicted permeability of unit cell 1

So, from Equation 8.10, we can get the permeability of these three different structures of unit cell as shown in Fig. 8.9. This figure shows that

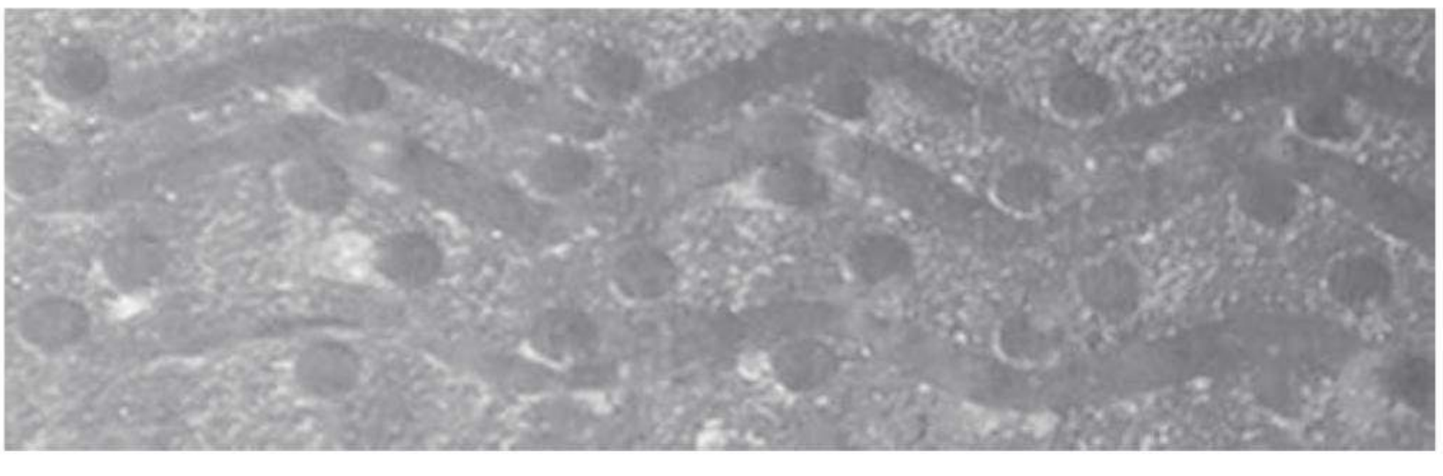

(a) Architecture of the structure

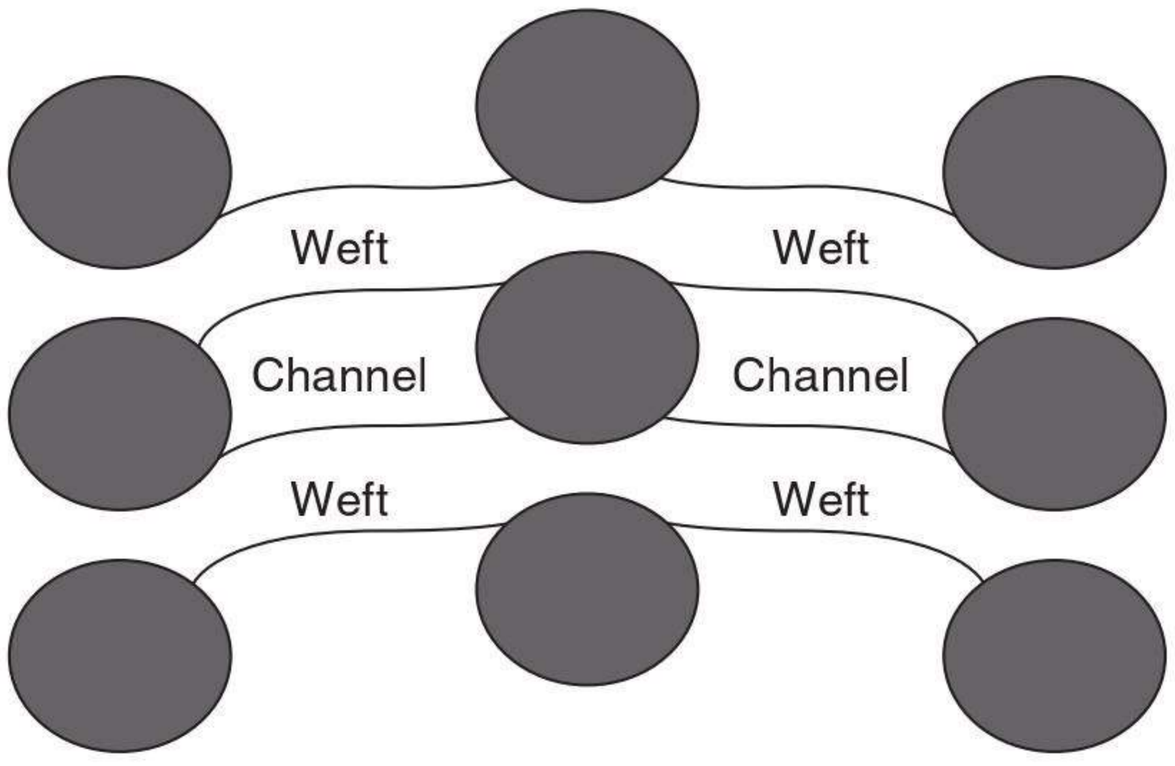

(b) An idealized structure

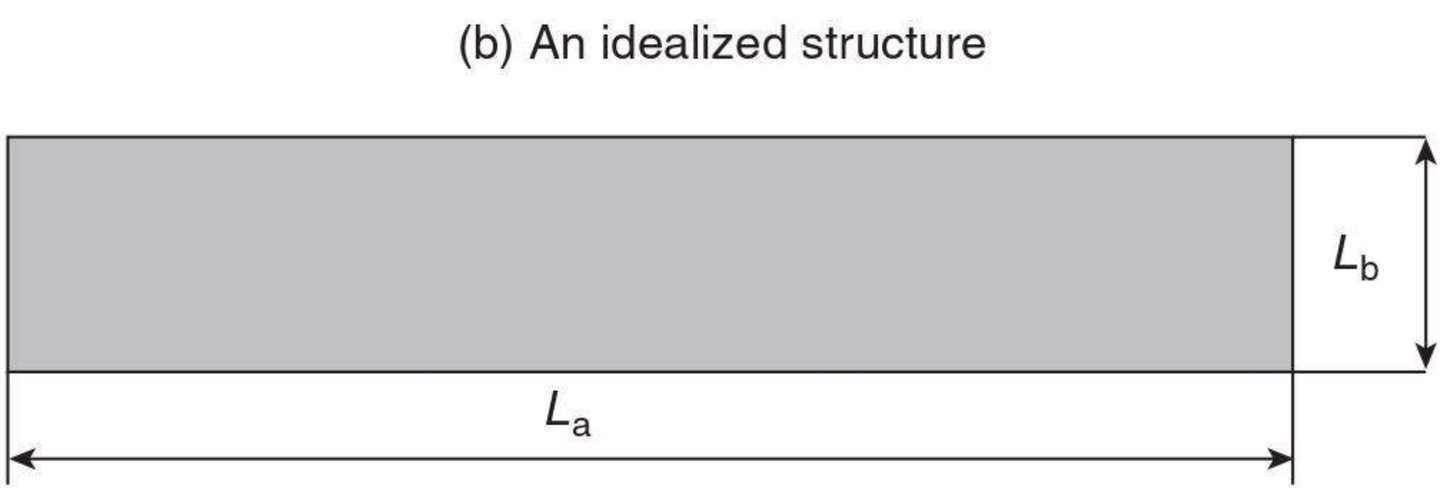

(c) An idealized unit cell

8.10 Simplified model of unit cell 2.

the permeability of stitch structure 3 is better than that of stitch structure 1. This is due to its easy-going pathway arrangement, and this is also testified by the subsequent experimental results as follows (Liu Yi, 2006).

8.4.5 Permeability model of unit cell 2

Unit cell 2 can be simplified as shown in Fig. 8.10. The permeability can be obtained from the expression for the equivalent permeability of a rectangular channel. In this study, the width of channel is assumed to be L_a; the height of the channel is L_b. The solution of the two-dimensional velocity field in an arbitrary duct geometry is governed by an equation of the Poisson form. Once the flow field is obtained, integration over the domain

provides a relationship for the average flow rate with respect to the applied pressure gradient. For a rectangular duct with sides of length L_a and L_b,

$$u = -\frac{l_a^2}{12}\left(\frac{dp}{dx}\right)\left[1 - \frac{192 l_a}{\pi^2 l_b}\sum_{n=1,3,5\ldots}^{\infty}\frac{\tanh(i\pi l_b/2l_a)}{i^5}\right] \quad 8.11$$

where u is fluid viscosity. This result can be compared to the Darcy law in one dimension:

$$u = -\frac{k_{equ}}{\mu}\frac{dp}{dx} \quad 8.12$$

Modelling the channel region as a porous medium of porosity 1.0, the average volume velocity may be equal to the average velocity provided by Equation 8.12. By comparison, we can obtain the permeability of this duct:

$$K_2 = -\frac{l_a^2}{12}\left[1 - \frac{192 l_a}{\pi^2 l_b}\sum_{n=1,3,5\ldots}^{\infty}\frac{\tanh(i\pi l_b/2l_a)}{i^5}\right] \quad 8.13$$

8.4.6 Permeability of whole structure

As shown in Fig. 8.11, the permeability of layer n is represented by K_n, and the height is represented by M_n. The total flow rate through the multi-layer, q, and the total height M can be expressed as follows:

$$q = q_1 + q_2 + \ldots + q_n = \sum_{i=1}^{n} q_i \quad 8.14$$

$$M = M_1 + M_2 + \ldots + M_n = \sum_{i=1}^{n} M_i \quad 8.15$$

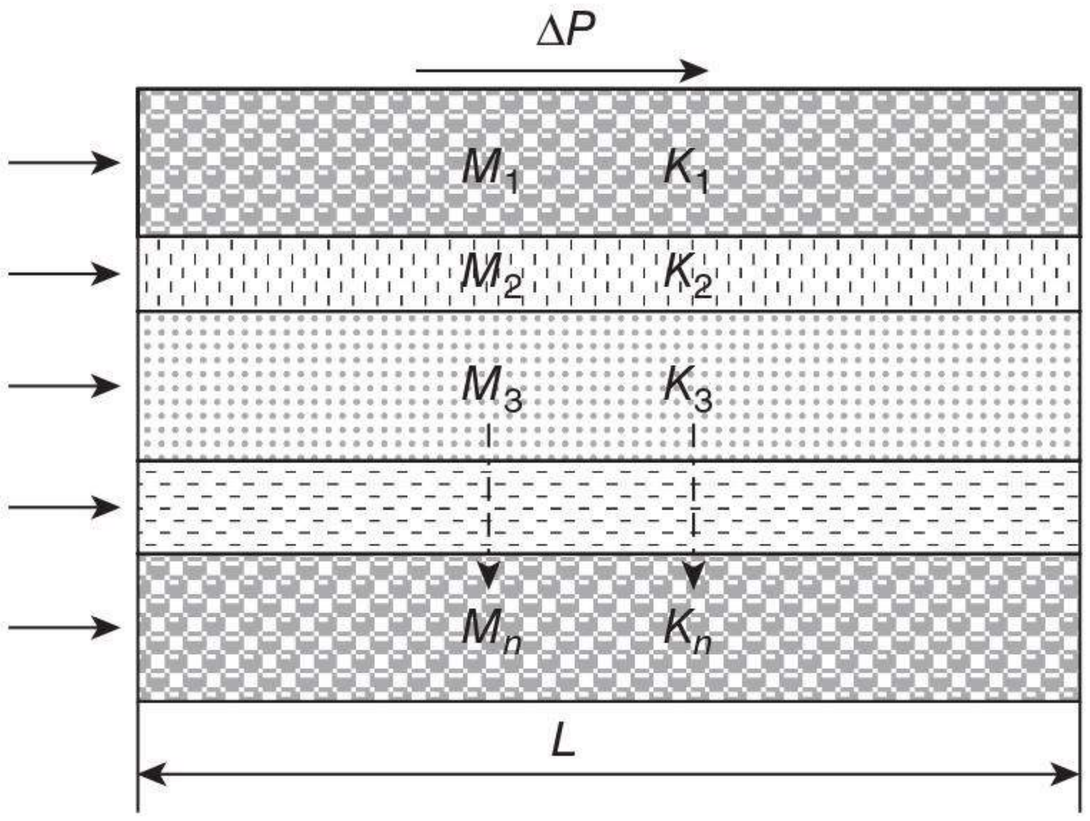

8.11 Schematic of multilayer laminar flow.

The pressure difference of each layer can be shown in the following equation:

$$\Delta P = \Delta P_1 = \Delta P_2 = \ldots = \Delta P_n \tag{8.16}$$

From the Darcy law,

$$q_i = K_i M_i \cdot \frac{\Delta P_i}{L} \tag{8.17}$$

we can get the total flow rate:

$$q = \sum_{i=1}^{n} q_i = \sum_{i=1}^{n} K_i M_i \cdot \frac{\Delta P_i}{L} = K_p \cdot M \cdot \frac{\Delta P}{L} \tag{8.18}$$

So the effective permeability of a multilayer flow channel K_p is given by

$$K_\mathrm{p} = \sum_{i=1}^{n} K_i \cdot M_i \Big/ \sum_{i=1}^{n} M_i \tag{8.19}$$

Incorporating Equations 8.10 and 8.13 into Equation 8.19, we can get the final equation to calculate the effective permeability of multilayer woven fabrics (Liu Yi, 2006):

$$K_\mathrm{p} = (K_1 M_1 + K_2 M_2)/(M_1 + M_2) \tag{8.20}$$

$$K_\mathrm{p} = \frac{\dfrac{16}{9\pi\sqrt{2}}\left(\sqrt{\dfrac{V_{\mathrm{f,max}}}{V_\mathrm{f}}} - 1\right)^{5/2} R^2 \cdot M_1 - \dfrac{l_\mathrm{a}^2}{12}\left(1 - \dfrac{192 l_\mathrm{a}}{\pi^2 l_\mathrm{b}} \sum\limits_{n=1,3,5\ldots}^{\infty} \dfrac{\tanh(i\pi l_\mathrm{b}/2l_\mathrm{a})}{i^5}\right) M_2}{(M_1 + M_2)} \tag{8.21}$$

8.5 Fractal permeability model

8.5.1 Fractal characterization of pore microstructures in fibre preforms

Figure 8.12 displays a cross-sectional view of multilayer woven preforms. There are two types of pores, a macropore (of the order of 10^{-3} m) between fibre tows, and the micropores (10^{-6}–10^{-5} m) inside the fibre tows. If several layers of fibre mats were stacked together, the macropores of each layer would form macro-channels with the sizes of 10^{-3} m, see Fig. 8.11, while micropores inside the fibre tows would form numerous tortuous micro-channels. Both the macro-channels and the micro-channels should follow the fractal scaling law given by Mandelbrot and Freeman (1982):

$$l_\mathrm{t}(\lambda) = \lambda^{1-D_\mathrm{T}} L_0^{D_\mathrm{T}} \tag{8.22}$$

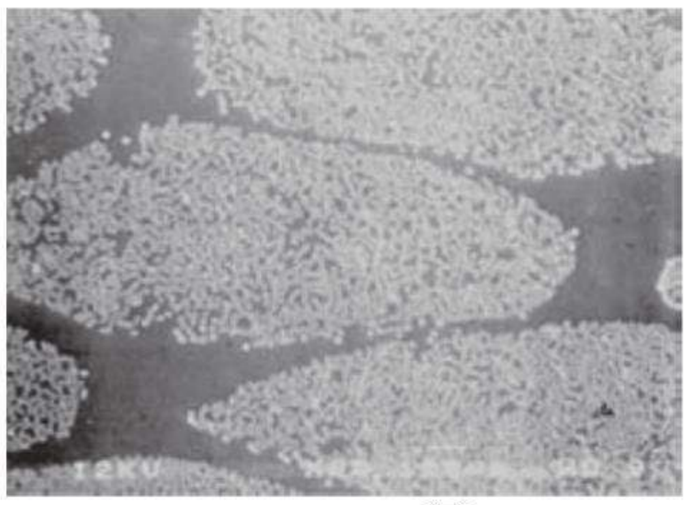

8.12 Micrograph of fibres and resin.

where D_T is the tortuosity fractal dimension, with $1 < D_T < 2$, representing the extent of convolutedness of capillary pathways for fluid flow through a medium, λ is the size of a pore channel in a fibre preform, and $L_t(\lambda)$ is its tortuous length along the flow direction.

For the macropores between fibre tows and the micropores inside fibre tows, the cumulative size distribution of pores in porous fibre preforms follows the fractal scaling law:

$$N(L \geq \lambda) = \left(\frac{\lambda_{\max}}{\lambda}\right)^{D_f} \qquad 8.23$$

From Equation 8.23, it can be found that

$$-\mathrm{d}N = D_f \lambda_{\max}^{D_f} \lambda^{-(D_f+1)} \mathrm{d}\lambda \qquad 8.24$$

Equation 8.24 describes the scaling relationship of the cumulative pore number (Liu Yi, 2006).

8.5.2 Fractal model for permeability

This model is related to the architectural parameters of preforms, the pore area fractal dimension D_f and the tortuosity fractal dimension D_T. The total volumetric flow rate, Q, through the unit cell is an accumulation of the flows through all the individual pore channels, including the macroscopic pore (gap or channel) between the fibre tows and the microscopic pores inside the fibre tows. The flow rate through a single pore channel is given by modifying the well-known lubrication flow theory (Wheatcraft and Taylor, 1988):

$$q(\lambda) = \frac{-1}{6\mu} A\lambda^2 \frac{\Delta p}{L(\lambda)} \qquad 8.25$$

The total flow rate Q through the unit cell can be obtained by integrating the individual flow rate, $q(\lambda)$, over the entire range of pore sizes from the minimum pore size $\lambda = \lambda_{\min}$ to the maximum pore size $\lambda = \lambda_{\max}$ (Pitchumani and Ramakrishnan, 1999). According to Equations 8.22–8.24, we have

$$Q = -\int_{\lambda_{\min}}^{\lambda_{\max}} q(\lambda)\,\mathrm{d}N(\lambda) \tag{8.26}$$

$$Q = -\int_{\lambda_{\min}}^{\lambda_{\max}} \frac{-1}{6\mu} A\lambda^2 \frac{\Delta p}{L(\lambda)} D_{\mathrm{f}} \lambda_{\max}^{D_{\mathrm{f}}} \lambda^{-(D_{\mathrm{f}}+1)}\,\mathrm{d}\lambda \tag{8.27}$$

$$Q = \frac{A\Delta p D_{\mathrm{f}}}{6\mu L_0^{D_{\mathrm{T}}}(D_{\mathrm{T}} - D_{\mathrm{f}} + 1)} \lambda_{\max}^{1+D_{\mathrm{T}}} \left(1 - \left(\frac{\lambda_{\min}}{\lambda_{\max}}\right)^{D_{\mathrm{T}} - D_{\mathrm{f}} + 1}\right) \tag{8.28}$$

Since $1 < D_{\mathrm{T}} < 2$ and $1 < D_{\mathrm{f}} < 2$, there exist $D_{\mathrm{T}} - D_{\mathrm{f}} + 1 > 0$ and $0 < \left(\frac{\lambda_{\min}}{\lambda_{\max}}\right)^{D_{\mathrm{T}} - D_{\mathrm{f}} + 1} < 1$ in Equations 8.27 and 8.28. Due to $\left(\frac{\lambda_{\min}}{\lambda_{\max}}\right) \sim 10^{-2}$, Equation 8.28 can thus be reduced to

$$Q = \frac{A\Delta p D_{\mathrm{f}}}{6\mu L_0^{D_{\mathrm{T}}}(D_{\mathrm{T}} - D_{\mathrm{f}} + 1)} \lambda_{\max}^{1+D_{\mathrm{T}}} \tag{8.29}$$

Using the Darcy law, we obtain the permeability equation as follows:

$$K = \frac{\mu L_0 Q}{\Delta P A} = \frac{\mu L_0^{1-D_{\mathrm{T}}} D_{\mathrm{f}} \lambda_{\max}^{1+D_{\mathrm{T}}}}{6\mu(D_{\mathrm{T}} - D_{\mathrm{f}} + 1)} \tag{8.30}$$

Obviously, the permeability of fibre preforms is mainly determined by the macropore (gap or channel) between the fibre tows. The previous study indicated that the permeability contribution from micropores inside the fibre tows is negligible (Yu and Li, 2001). Thus, only the tortuosity of macropore channel pathways is included in the present consideration. It can be found that the macropore channels are approximately straight: see Fig. 8.11. Therefore, $D_{\mathrm{T}} = 1$ is applied in this investigation, and Equation 8.30 can be thus reduced to

$$K = \frac{D_{\mathrm{f}} \lambda_{\max}^2}{2 - D_{\mathrm{f}}} \tag{8.31}$$

in which D_{f} can be expressed as

$$D_{\mathrm{f}} = 2 - \frac{\ln \phi}{\ln(\lambda_{\min}/\lambda_{\max})} \tag{8.32}$$

So from this final equation, it can be predicted that with the increase of $\lambda_{\max}$, both D_{f} and K increase with it also (Liu Yi, 2006).

8.6 Conclusions

The effects of fabric microstructures and other properties of multilayer woven fabrics on permeability were examined in this chapter. A permeability model based on fractal theory has been presented to predict the

permeability of preforms fabricated by porous yarns. Another model based on the unit cell of quadratic fibre packing has also been established to predict the permeability of 3-D multilayer woven fabrics fabricated with the monofilaments.

For the 3-D multilayer woven fabrics fabricated with the monofilaments, the permeability model was related to the architectures of fibre preforms and their fibre volume fraction changes. It is evident that the permeability of monofilament preforms is mainly determined by the arrangement of the channels between the fibre tows. At the same fibre volume fraction, fabrics with a loose stitch array have better permeability than those with a compact stitch array. This is due to the different flow resistance with regard to the different stitch array. For fabrics with loose stitch structure, the flow resistance from the stitch array is less than that of fabrics with tight stitch array, thus leading to better permeability of fabrics with loose stitch array.

For the 3-D multilayer woven fabrics fabricated by porous yarns, a fractal permeability model was developed based on the fractal characteristics of pores in the fibre preforms to describe the disordered pore structures of preforms. The permeability model was found to be related to the pore area fractal dimension, the tortuosity fractal dimension, and the architectural parameters of fibre preforms. For fabrics with a rather large maximum pore size, λ_{max}, the flow resistance is relatively lower, hence the resin can impregnate more easily within it, thus leading to better permeability and less void formation in fabrics.

8.7 References

Adams K L and Rebenfeld L (1991), Permeability characteristics of multilayer fibre reinforcements, Part II: Theoretical model, *Polymer Composites*, **12**, 3, 186–190.

Adams K L, Miller B and Rebenfeld L (1986), Forced in-plane flow of an epoxy resin in fibrous networks, *Polymer Engineering and Science*, **26**, 20, 1434–1441.

Adams K L, Russel W B and Rebenfeld L (1988), Radial penetration of a viscous liquid into a planar anisotropic porous medium, *International Journal of Multiphase Flow*, **14**, 2, 203–215.

Advani S G and Calado V M A (1996), Effective average permeability of multi-layer preforms in resin transfer molding, *Composites Science and Technology*, **56**, May, 519–531.

Ambrosi D and Preziosi L (1998), Modelling matrix injection through elastic porous preforms, *Composites, Part A*, **29**, 1–2, 5–18.

Batch G L and Cumiskey S (1990), Multilayer compaction and flow in composites processing, *45th Annual conference SPI*, 1-11/session 9-A.

Berdichevsky A L and Cai Z (1993), Preform permeability predictions by self-consistent method and finite element simulation, *Polymer Composites*, **14**, 2, 132–143.

Blake F C (1922), The resistance of packing to fluid flow, *Transactions of the American Institute of Chemical Engineers*, **14**, 415–421.

Bruschke M V and Advani S G (1993), Flow of generalized Newtonian fluids across a periodic array of cylinders, *Journal of Rheology*, **37**, 3, 479–498.

Cai Z and Berdichevsky A L (1993), An improved self-consistent method for estimating the permeability of a fiber assembly, *Polymer Composites*, **14**, 4, 314–323.

Cairns D S, Humbert D R and Mandell J F (1999), Modelling of resin transfer molding of composite materials with oriented unidirectional plies, *Composites, Part A: Applied Science and Manufacturing*, **30**, 375–382.

Carman P C (1937), Fluid flow through granular beds, *Transactions of the Institution of Chemical Engineers*, **15**, 150–166.

Carter E J, Fell A W and Summerscales J (1995), A simplified model to calculate the permeability tensor of an anisotropic fibre bed, *Composites Manufacturing*, **6**, 3/4, 228–235.

Chan A W and Hwang S T (1991), Anisotropic in-plane permeability of fabric media, *Polymer Engineering and Science*, **31**, 16, 1233–1239.

Chang C Y and Hourng L W (1998), Study on void formation in resin transfer molding, *Polymer Engineering and Science*, **38**, 5, 809–818.

Coulter J P and Guceri S I (1988), Resin transfer molding: process review, modeling and research opportunities, *Proceedings of Manufacturing International '88,* Atlanta, GA, 79–86.

Darcy H P G (1856), Les Fontaines Bibliques de la Ville de Dijon, Victor Dalmont, Paris.

Ferland P, Guittard D and Trochu F (1996), Concurrent methods for permeability measurement in resin transfer molding, *Polymer Composites*, **17**, 1, 149–158.

Gebart B R (1992), Permeability of unidirectional reinforcements for RTM, *Journal of Composite Materials*, **26**, 8, 1100–1133.

Guangbiao Xu and Fumei Wang (2005), Prediction of the permeability of woven fabrics, *Journal of Industrial Textiles*, **34**, 4, 243.

Hirt D E, Adams K L, Prud'Homme R K and Rebenfeld L (1987), In-plane radial fluid flow characterization of fibrous materials, *Journal of Thermal Insulation*, **10**, 153–172.

Ko F K and Du G-W (1997), Processing of textile preforms, in *Advanced Composites Manufacturing* (ed. T G Gutowski), John Wiley, New York, 157–206.

Kolodziej J A, Dziecilak R and Konczak Z (1998), Permeability tensor for heterogeneous porous medium of fibre type, *Transport in Porous Media*, **32**, 1–99.

Kozeny J (1927), Ueber Kapillare Leitung des Wassers im Boden, *Sitzungsberichte, Akademie der Wissenschaften in Wien*, **136**, 271–301.

Lai C L and Young W B (1997), Model resin permeation of fibre reinforcements after shear deformation, *Polymer Composites*, **18**, 5, 642–648.

Lee L J (1997), Liquid composite molding, in *Advanced Composites Manufacturing* (ed. T G Gutowski), Wiley-Interscience, New York, 393.

Lekakou C, Johari M A K and Bader M G (1996b), Compressibility and flow permeability of two-dimensional woven reinforcements in the processing of composites, *Polymer Composites*, **17**, 666–672.

Liu Yi (2006), Study of the permeability of multi-layer woven fabrics, Ph.D. thesis, Institute of Textiles and Clothing, Hong Kong Polytechnic University.

Loos A C, Weidermann M H and Kranbuchi D E (1991), Processing of advanced textile structural composites by RTM, *Proc. 5th Textile Structural Composites Symposium,* Drexel University, Philadephia, PA, 4–6 December.

Lundström T S (2000), The permeability of non-crimp stitched fabrics, *composites, Part A: Applied Science and Manufacturing*, **31**, 1345–1353.

Mandelbrot B B and Freeman W H (1982), *The Fractal Geometry of Nature*, W.H. Freeman, New York, 23–57.

Martin G Q and Son J S (1986), Fluid mechanics of mold filling for fibre reinforced plastics, *Proc. Second Conf. on Advanced Composites,* 18–20 November, Dearborn, MI, 149–157.

Mogavero J and Advani S G (1997), Experimental investigation of flow through multi-layer preforms, *Polymer Composites*, **18**, 5, October, 649.

Padaki N V, Alagirusamy R and Sugun B S (2006), Knitted preforms for composite applications, *Journal of Industrial Textiles*, **35**, 4, 295–321.

Parnas R S and Phelan Jr F R (1991), The effect of heterogeneous porous media on mold filling in resin transfer molding, *SAMPE Quarterly*, **22**, 53–60.

Parnas R S and Salem A J (1993), A comparison of the unidirectional and radial in-plane flow of fluids through woven composite reinforcements, *Polymer Composites*, **14**, 5, 383–394.

Pillai K M and Advani S G (1998), Numerical simulation of unsaturated flow in woven fibre preforms during the resin transfer molding process, *Polymer Composites*, **19**, 1, 71–80.

Pitchumani R and Ramakrishnan B (1999), A fractal geometry model for evaluating permeabilities of porous preforms used in liquid composite molding, *International Journal of Heat and Mass Transfer*, **42**, 2219–2232.

Rudd C D, Morris D J, Chick J P and Warrior N A (1995), Material characterization for SRIM, *4th Int. Conf. on Automated Composites (ICAC '95),* Nottingham, UK, **1**, 211–218.

Rudd C D, Long A C, McGeehin P and Smith P (1996), In-plane permeability determination for simulation of liquid composite molding of complex shapes, *Polymer Composites*, **17**, 1, 52–59.

Rudd C D, Long A C, Kendall K N and Mangin G E (1997), *Liquid Moulding Technologies*, Woodhead, Cambridge, UK.

Shih C H and Lee L J (1998), Effect of fibre architecture on permeability in liquid composite molding, *Polymer Composites*, **19**, 5, 629–639.

Simacek P and Advani S G (1996), Permeability model for a woven fabric, *Polymer Composites*, **17**, 6, 887–899.

Skartsis L, Kardos J L and Khomami B (1992), Resin flow through fibre beds during composite manufacturing processes, Part 1 and Part 2, *Polymer Engineering Science*, **32**, 4, 221–231.

Smith P, Rudd C D and Long A C (1997), The effect of shear deformation on the processing and mechanical properties of aligned reinforcements, *Composites Science and Technology*, **57**, 327–344.

Van der Westhuizen J and Du Plessis J P (1996), An attempt to quantify fibre bed permeability utilizing the phase average Navier–Stokes equation, *Composites, Part A*, **27A**, 263–269.

Wang C Y (1996), Stokes flow through an array of rectangular fibres, *International Journal of Multiphase Flow*, **22**, 1, 185–194.

Wang T J, Wu C H and Lee L J (1994), In-plane permeability measurement and analysis in liquid composite molding, *Polymer Compos*ites, **15**, 4, 278.

Weitzenböck J R, Shenoi R A and Wilson P A (1999a), Radial flow permeability measurement, Part A: Theory; Part B: Application, *Composites, Part A: Applied Science and Manufacturing*, **30**, 6, 781–796, 797–813.

Weitzenböck J R, Shenoi R A and Wilson P A (1999b), Measurement of principal permeability with the channel flow experiment, *Polymer Composites*, **20**, 2, 321–335.

Wheatcraft S W and Taylor S W (1988), An explanation of scale dependent dispersivity in heterogeneous aquifers using concepts of fractal geometry, *Water Resources Research*, **24**, 566–578.

Williams J G, Morris C E M and Ennis B C (1974), Liquid flow through aligned fibre beds, *Polymer Engineering and Science*, **14**, 6, 413–419.

Yu B M and Li J H (2001), Some fractal characters of porous media, *Fractals*, **9**, 3, 365–372.

9

Using multilayer woven fabrics in resin transfer moulding

Abstract: In this chapter a detailed theoretical analysis for in-plane impregnation in multilayer woven (MLW) fabrics is reported in order to understand the mechanism of void formation. Unlike the previous works, where the void is formed in the plane of one layer of woven fabric, the void formation in the cross-section of MLW fabrics is presented. Based on two simplified unit cells, which were identified from two typical multiple modes of MLW fabrics, a mathematical model is developed to analyze the formation and size of voids. The flow front and void formation processes are also numerically simulated using the control-volume method.

Key words: multilayer woven (MLW) fabrics, flow resistance of MLW fabrics, void formation, flow modelling of MLW fabrics, filling properties of MLW fabrics.

9.1 Introduction

Resin transfer moulding (RTM) is a high-performance net-shape manufacturing process for polymer and advanced high-performance textile composite parts, especially in the aircraft and automobile industries due to its relatively short cycle time, low labour requirements and equipment costs. It is particularly suitable for producing large and geometrically complex parts. However, at present, part fabrication by RTM is a very expensive proposition due to the typically long process development time, limiting the potential use of the process. RTM consists of the following steps: (a) preform fabrication, (b) preform placement inside the mould, (c) mould filling by resin injection, (d) curing, and finally (e) demoulding of the finished part. The inherent variations of the process make it difficult to predict what happens inside the mould during the filling and curing stages and therefore what the properties of the resulting part will be. Both filling and curing are critical steps, though successful mould filling without dry spots is the first step to having a defect-free part (Barooah *et al.*, 2001).

Ideally, the resin flow should progress so that the last part of the mould to be filled is near the vents, and the preform is wetted out completely without leaving any dry spots. The flow pattern in the mould depends on such parameters as preform porosity and permeability, and resin viscosity. These properties are required as input parameters for the physical

models used to simulate mould filling. However, the permeability and porosity cannot be estimated accurately beforehand as compaction, preform preparation, etc. all affect their values. A common problem is the edge effect called racetracking which makes the resin flow faster along the edges of the preform. These random, unpredictable variations in the preform properties make it extremely difficult to predict resin flow progression accurately, which in turn makes it difficult to design an effective injection and venting scheme without trial and correction cycles.

Unfortunately, the fibre preform always has complicated and non-uniform microstructure, and hence its local permeability may differ by several orders of magnitude between inside and outside fibre tow. These non-uniform properties finally lead to the formation of air voids on the micro scale (Parnas and Phelan, 1991; Patel and Lee, 1995; Chen *et al.*, 1995).

Previous research (Yosida *et al.*, 1986; Harper *et al.*, 1987; Bowles and Frimpong, 1991; Feldgoise *et al.*, 1991; Ghiorse and Jurta, 1991) has revealed that the presence of voids is highly undesirable and has a deleterious effect on product mechanical properties including the interlaminar shear strength, compressive strength, impact resistance and fatigue life. The research has also revealed that the void formation and development are correlated to injection pressure, outlet pressure, resin properties (viscosity, surface tension), fabric characteristics (type and orientation of fibres, surface treatment), etc. Some studies (Hayward and Harris, 1990; Chen *et al.*, 1995) reported that having vacuum assistance will reduce the quantities of voids but cannot totally solve the problem. In recent years, the problem of void formation has received much attention and has been studied extensively. However, the variety of the architectures of fibre preforms is too large to allow the prediction of void formation based on one general model only. Furthermore, void formation in RTM seems to be inevitable and there is no proven way to eliminate voids completely (Chang and Hourng, 1998). Hence, understanding of the void formation mechanism is important and is necessary for the mould and fibre preform design.

As is well known, there are two scales of flow during RTM: one is the macro flow in the gaps between/around the tows, and the other is the micro flow within tows. Based on this concept, several investigators have developed models to predict void formation in RTM. Parnas and Phelan (1991) developed a model to predict the air entrapment for flow through unidirectional fibre mats with the global flow transverse to the fibres. Chen *et al.* (1995) also developed a model similar to that of Parnas and Phelan. The difference between these two models is that Chen *et al.* included the effects of capillary pressure on the impregnation of fibre tows. Also based on the concept of the two scales of flow, Chan and Morgan (1992) developed a model to analyze the resin flow and air entrapment during RTM of bidirectional non-woven fibre performs. Patel and co-workers carried out flow

visualization experiments of void formation in unidirectional stitched, bidirectional stitched and four-harness woven fibreglass mat (Patel and Lee, 1995). They reported that fingering took place at the flow front because the permeabilities in the fibre tows and in the gaps between the fibre tows were different, and void formation was correlated to capillary number and the liquid-fibre–air contact angle. For axial flow, the microvoids were formed at $Ca^* > 10^{-3}$, and for transverse flow, the microvoids were formed at an even lower capillary number, ~10^{-4}. Once formed, the microvoids were difficult to purge and remained trapped even after bleeding the liquid at much higher flow rates than those at which they were formed (Rohatgi *et al.*, 1996).

Several researchers have carried out theoretical analyses to describe the mechanism of void formation during RTM. Binetruy and Hilaire (1998) developed an analytical model to describe the tow impregnation where the global flow is parallel to the fibre axis. Based on the study of the contribution of the axial and transverse flow mechanisms inside tows, this model shows that the main tow impregnation process is transverse to the fibre axis. A criterion has been established to indicate when the axial flow can be neglected to simplify the tow impregnation. Kang *et al.* (2000) proposed a mathematical model to describe the mechanisms of void formation when global flow is transverse to fibre tow. The model shows that for a given fibre preform, the effects of resin velocity and capillary pressure can be described by the capillary number. With proper calibration, it can predict the size and content of voids within fibre tows as well as between them.

In this chapter a detailed theoretical analysis for in-plane impregnation in multilayer woven fabrics (MWFs) is reported to understand the mechanism of void formation. Unlike the previous work (Patel and Lee, 1995), where the void is formed in the plane of one layer of the woven fabric, the void formation in the cross-section of MWFs has been presented. Based on two simplified unit cells, which were identified from two typical multiple modes of MWFs, a mathematical model is developed to analyze the formation and size of voids. The flow front and void formation processes are also numerically simulated using the control-volume method.

9.2 Flow resistance of multilayer woven fabrics

Flow resistance is an important property of textile materials. Earlier research showed that the efficiency of various processes in open-width wet textile finishing depends mainly on the amount of flow of the process fluid through the textile material. This flow depends not only on process parameters like fabric velocity and on machine parameters like roller diameter, but also on the flow resistance of the treated textile materials. It is clear that this flow resistance is a function of the geometry of the textile material, hence it

important to establish a relation for the flow resistance of a woven textile fabric as a function of its geometry.

First, let us consider one layer of plain weave fabric. The typical architecture is displayed in Fig. 9.1(a). As described by Simacek and Advani (1996), there are two sub-domains within the perform. One consists of the fibre tows (warp and weft) which are woven together to create an interconnected network. Another is a network of empty pores and channels around yarns. Due to the non-uniform permeability in these two sub-domains, during RTM processes voids are formed not only in the plane of the fabric as described by Patel and Lee (1995), but also in the cross-section of multilayer woven fabric.

Three important geometrical parameters of this fabric are tow thickness h, tow width l_b and width of channel between adjacent tows l_c. Usually, the ratio l_b/h is about 5 or more for most reinforcement used in composites processing, and the cross-sections of fibre tows are not circular but elliptical as shown in Fig. 9.1(b). The present study focuses on resin impregnation and void formation in the cross-section of MWFs. For the purpose of simplicity, the configuration of the undulating yarns is approximated by linear segments and the cross-section of the fibre tow is considered to be rectangular; then an idealized cross-section of one-layer plain woven fabric for in-plane impregnation along the x-direction can be obtained as shown in Fig. 9.1(c).

When multiple layers of woven fabric are stacked together, due to the in-plane displacement, two typical modes can be observed as shown in

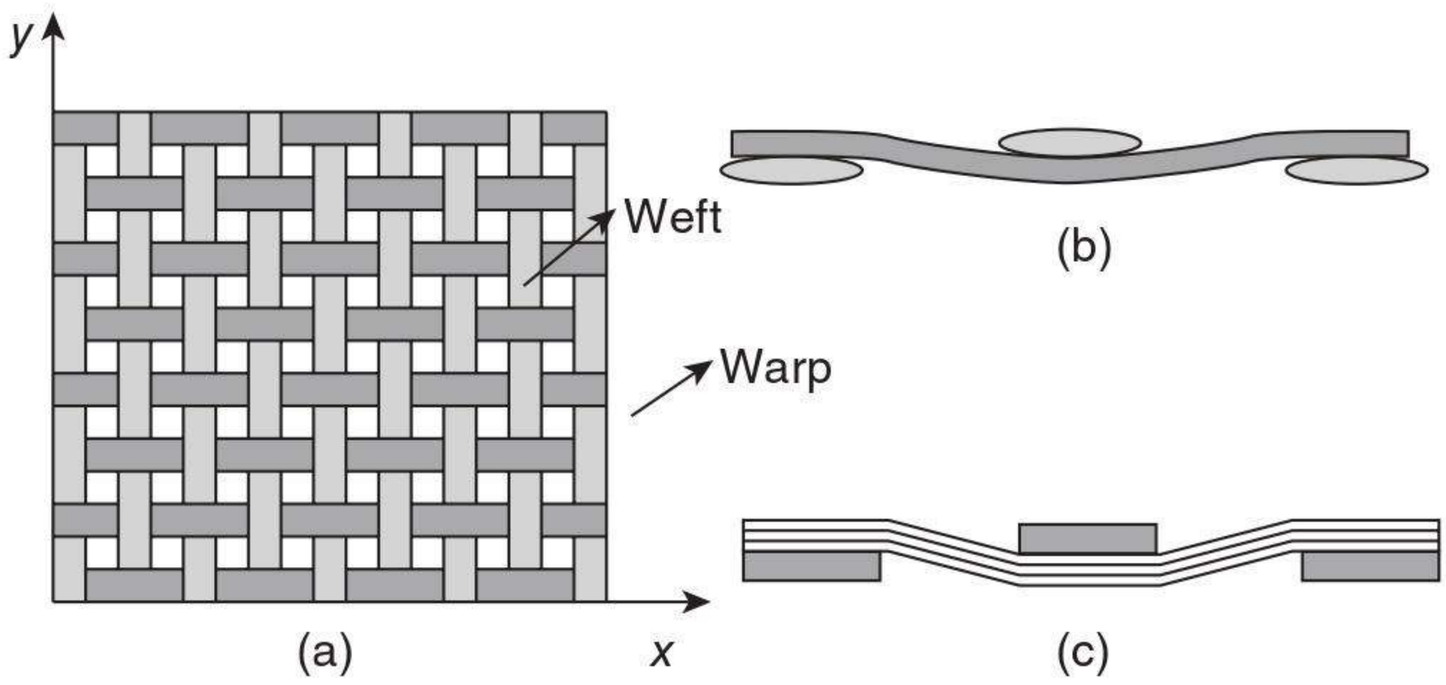

9.1 Architecture of the plain woven fabric.

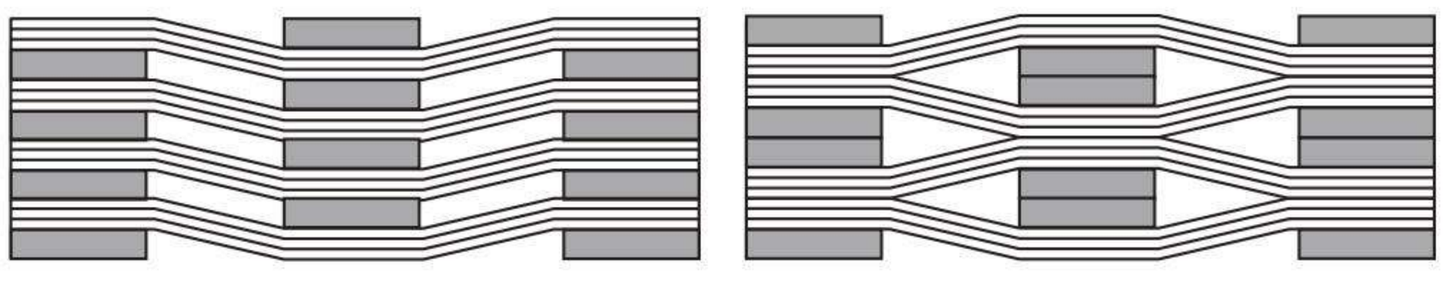

(a) Mode I (b) Mode II

9.2 Two typical multiple modes of MWFs.

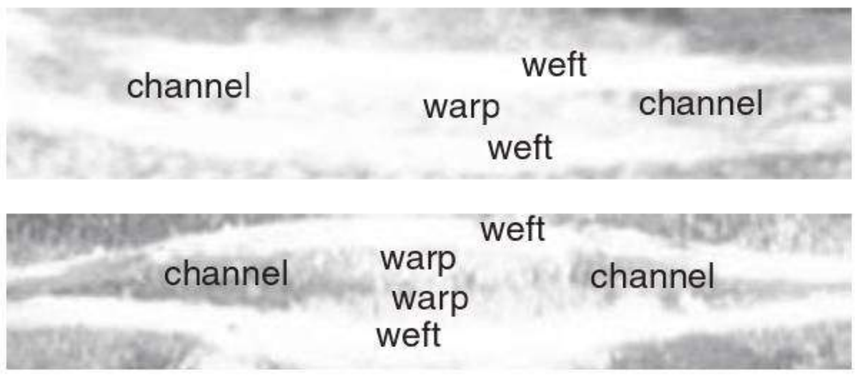

9.3 Typical cells of cross-section for MWFs.

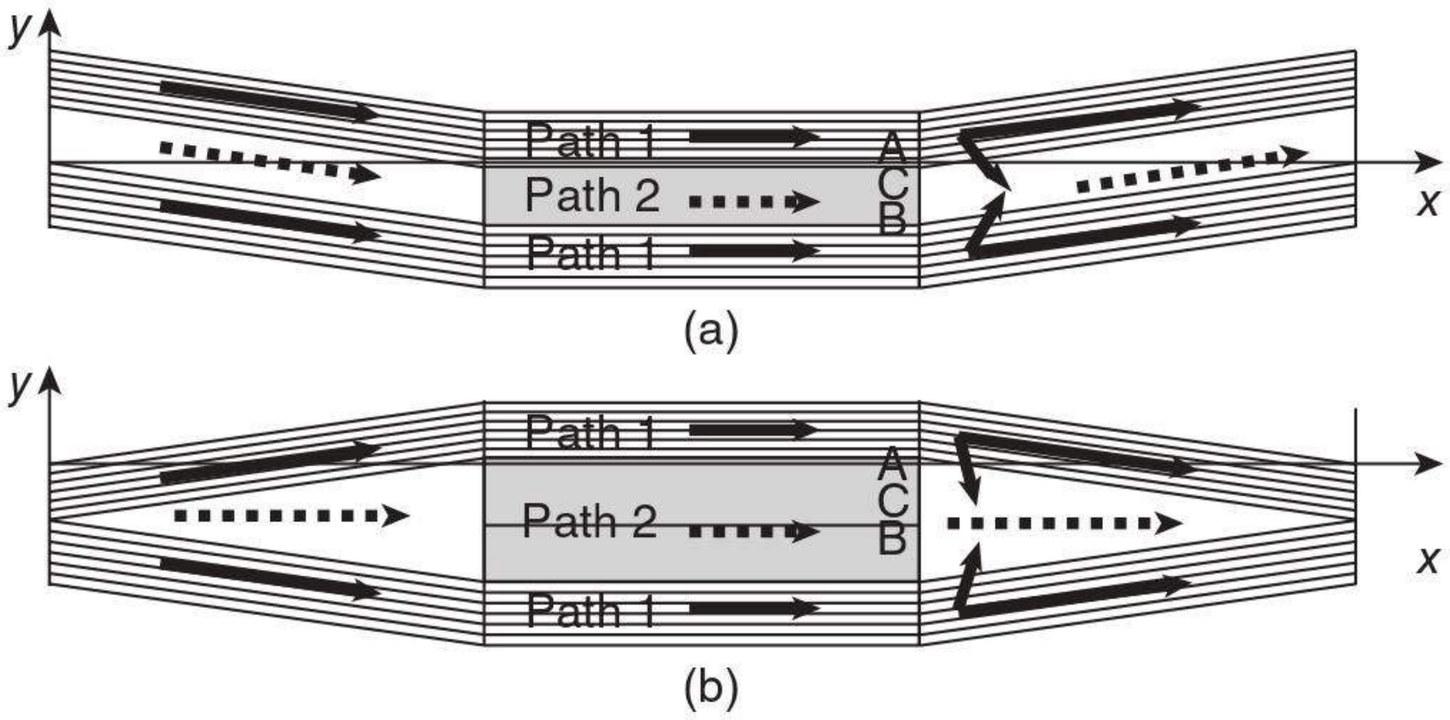

9.4 Unit cells for mode I and mode II.

Fig. 9.2. In mode I, there is no displacement between adjacent layers, while there is a displacement l_c in mode II. The above analysis is strongly supported by image analysis as shown in Fig. 9.3. Although the actual woven fabrics are 3-D, in this simulation we only consider the flow along the cross-section of woven fabrics. So this 2-D simulation model can simulate the flow along the cross-section of 3-D woven fabrics.

In both multiple modes, two unit cells for the void formation can be identified as shown in Fig. 9.4(a) and (b). It can be seen that the flow through the cross-section of the unit cell passes through not only the channel but also the weft and warp. Most resin would flow through the channels along the imposed pressure gradient, but it can also flow within warps and wefts. So we choose two paths as a representative cell, as shown in Fig. 9.4. One way is along the weft tow while the other is the flow in the channel and warp. As testified in the study of Patel and Lee (1995), the formation of voids is mainly due to the velocity difference of resin in different paths.

9.3 Flow modelling of multilayer woven fabrics

In the case of high injection pressure, the effect of capillaries is negligible; voids will form at the end of the warp tow as shown in Fig. 9.4. This will be discussed in more detail as follows. Since the thickness of fibre tows is far less than their width, the flow in path 1 can be simplified to flow along

a straight fibre tow. Then the time t, required for the flow front to reach position A can be approximated by

$$t_1 = \frac{(l_c + l_b)^2}{2K_b^a(P_0 - P_f)} \tag{9.1}$$

where μ is the viscosity of the fluid, K_b^a is the axial permeability of the fibre tow, and P_0 and P_f are the pressures at the inlet and flow front, respectively. When the flow front in path 1 reaches position A, on the one hand resin will keep on flowing along the weft, and on the other hand resin also will flow transversely to position B due the high permeability of the channel between tows. The time T_1 for the flow front to reach position B can be obtained from the following analysis.

For the given coordinate system (see Fig. 9.4) the transverse velocity V_t at an arbitrary point C (y, x_c) between A and B takes the form

$$V_t = \frac{dy}{dt} = \frac{K_c(P_0 - P_f)}{y}\left(1 - \frac{x_c}{x_f}\right) \tag{9.2}$$

where K_c is the permeability of the channel, $x_c = l_c + l_b$, and x_f is the x-coordinate of the flow front along path 1 when transverse flow reaches point C, which is given by

$$x_f = \sqrt{\frac{2K_b^a(P_0 - P_f)}{\mu}t} \tag{9.3}$$

Inserting Equation 9.3 into Equation 9.2 and integrating it with the boundary conditions:

$$y = 0 \text{ at } t = t_1$$

$$y = h_0 \text{ at } t = T_1 \ (h_0 = h/2 \text{ for model I}, h \text{ for model II})$$

we obtain

$$\frac{h_0^2}{2K_c(P_0 - P_f)} = T_1 - \frac{2(l_c + l_b)\sqrt{T_1}}{\sqrt{\frac{2K_b^a(P_0 - P_f)}{\mu}}} + \frac{(l_c + l_b)^2}{2K_b^a(P_0 - P_f)} \tag{9.4}$$

Then

$$T_1 = \left(\frac{l_c + l_b}{\sqrt{\frac{2K_b^a(P_0 - P_f)}{\mu}}} + \frac{h_0}{\sqrt{\frac{2K_c(P_0 - P_f)}{\mu}}}\right)^2 \tag{9.5}$$

For flow in path 2, the fluid will alternately flow within the channel and the fibre tows. We know that the transverse permeability in the fibre tow is much lower than that in the channel; at the same time the width l_c of the

channel is always less than or equal to the width l_b of the tow. Then the time T_2 required for the flow front in path 2 to reach position B can be approximated by

$$T_2 = \frac{l_b(l_c + l_b)}{2K_b^t(P_0 - P_f)} \tag{9.6}$$

Dividing Equation 9.5 by Equation 9.6, this yields the time ratio

$$\frac{T_1}{T_2} = \left(\frac{l_c + l_b}{\sqrt{\frac{2K_b^a(P_0 - P_f)}{\mu}}} + \frac{h_0}{\sqrt{\frac{2K_c(P_0 - P_f)}{\mu}}} \right)^2 \times \frac{2K_b^t(P_0 - P_f)}{l_b(l_c + l_b)} \tag{9.7}$$

The above equation can be further simplified by the quantity analysis. Noticing that the ratio of $h_0/(l_c + l_b)$ is smaller (10^{-1} to 10^{-2}) and the ratio K_c/K_b^a is larger (10 to 10^2) for most preforms used in composite processing, the second term in Equation 9.5 is much smaller than the first term. Then Equation 9.7 can be simplified to

$$\frac{T_1}{T_2} = \frac{(l_c + l_b)^2}{2K_b^a(P_0 - P_f)} \cdot \frac{2K_b^t(P_0 - P_f)}{l_b(l_c + l_b)} = \frac{l_c + l_b}{l_b} \cdot \frac{K_b^t}{K_b^a} \tag{9.8}$$

Usually, the ratio K_b^a/K_b^t is about 20 for the same fibre tow. At the same time, $l_c \le l_b$, so it seems that void formation in the cross-section of multilayer woven fabric is inevitable. The size of void mainly depends on the ratio K_b^a/K_b^t. In order to reduce the size and quantity of voids, it will be useful to use fibre tows with higher K_b^t for warp.

According to the simplified model, the flow through the cross-section of MWFs passes through five different basic sub-domains as shown in Fig. 9.5. In this thesis, the permeability tensors of these sub-domains are defined respectively as follows. For sub-domains a, b, c and d, the permeability for flow along and transverse to fibres is often evaluated from the Kozeny–Carman equation:

$$K = \frac{r_f^2}{4k} \cdot \frac{(1 - V_f)^3}{V_f^2} \tag{9.9}$$

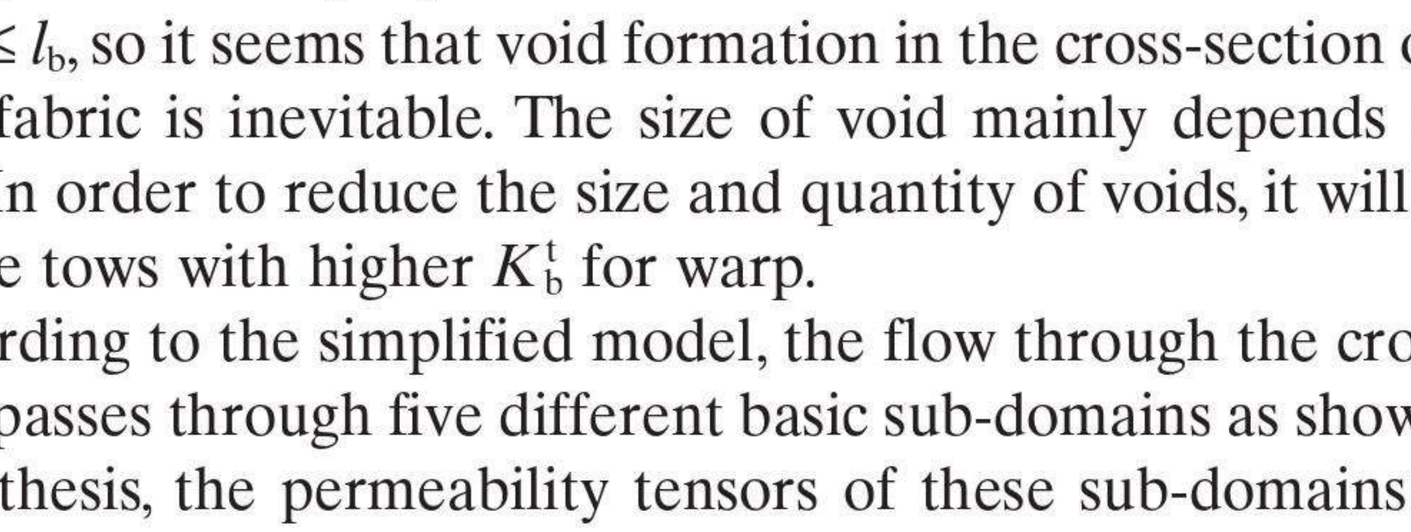

9.5 Sub-domains of MWFs.

where r_f is the fibre radius, V_f is the fibre volume fraction, and k is the Kozeny constant, which has been taken as $k_{//} = 0.5$ for flow along the fibres and $k_{\perp} = 10$ for flow transverse to the fibres (Williams *et al.*, 1974; Gutowski *et al.*, 1987b). Since this equation cannot predict the phenomenon that the transverse flow will stop at the maximum fibre volume fraction, a number of further modelling studies of permeability have been performed by Gutowski *et al.* (1987a), Gebart (1992) and Cai and Berdichevsky (1993). In this study, the fibre fractions employed were lower than $V_{f,max}$, hence permeability was evaluated according to Equation 9.9.

For sub-domains e and f, the permeability can be obtained from the expression for the equivalent permeability of a rectangular-shaped channel. In this study, the width of the channel is assumed to be l_b, and the height of the channel h_c is h for sub-domain f and 0 to h or $2h$ for sub-domain e. The velocity at the boundary of these channels is set to the Darcy velocity of fibre tows.

$$K_c = \frac{w_c^3}{h_c}\left[\frac{16}{\pi^5}\sum_{n=1,3,5\ldots}^{\infty} -\frac{1}{n^5}\frac{\exp\left(n\pi\frac{h_c}{w_c}\right)}{\exp\left(n\pi\frac{h_c}{w_c}\right)+1}+\frac{1}{12}\frac{h_c}{w_c}\right]+\frac{K_b}{(1-V_f)} \qquad 9.10$$

in which $w_c = l_b$ and

$$h_c = \begin{cases} h & \text{for sub-domain f} \\ 0 \text{ to h or 2h} & \text{for sub-domain e} \end{cases}$$

In Equation 9.10, K_b and V_f are permeability and volume fraction of fibre tows, respectively.

9.4 Modelling flow and void formation

The numerical simulations using the control-volume method of the flow fronts and void formation in both unit cells of MWFs are presented in this section. The preform in the mould is assumed to be rigid and is treated as porous medium, the flow in which is described by the following Darcy law:

$$\mathbf{U} = -\frac{1}{\mu}\mathbf{K}\cdot\nabla P \qquad 9.11$$

in which μ is the viscosity of the resin. In a two-dimensional flow field,

$\mathbf{U} = (u_x, u_y)^T$ is the flow velocity vector

$\nabla P = \left(\frac{P}{x}, \frac{P}{y}\right)^T$ is the pressure gradient vector

$\mathbf{K} = \begin{bmatrix} K_{xx} & K_{xy} \\ K_{yx} & K_{yy} \end{bmatrix}$ is the permeability tensor.

Inserting Equation 9.11 into the continuity equation for an incompressible fluid gives the governing equation for pressure distribution in the flow field:

$$\nabla \cdot \left(\frac{1}{\mu} \begin{bmatrix} K_{xx} & K_{xy} \\ K_{yx} & K_{yy} \end{bmatrix} \begin{bmatrix} \frac{\partial p}{\partial x} \\ \frac{\partial p}{\partial y} \end{bmatrix} \right) = 0 \qquad 9.12$$

The corresponding boundary conditions to be imposed can be stated as follows:

At injection gates: $P = P_0$ (for constant pressure injection)

At the mould wall: $\dfrac{P}{n_{\text{wall}}} = 0$

At the flow front: P = atmospheric pressure P_{f} (high injection pressure)

After the void is formed, the pressure in the void is assumed to obey the ideal gas law: $P_\rho = \rho RT$, where ρ is the density of air and R is the ideal gas constant.

It is noticed that Equation 9.12 is steady state. Although the mould filling process is time dependent, it can be treated as a series of steady-state problems by time increment. Within each time step, the pressure in the flow field can be determined by Equation 9.12. Generally, Equation 9.12 needs to be solved numerically. In the present simulation, the control-volume method is used.

The entire flow field is first discretized into a finite element mesh. In this simulation, a three-node triangular element is used. One node corresponds to one control volume. A control volume is composed of several sub-areas. The number of sub-areas is the same as the number of node-adjacent elements. The formation of the control volume is illustrated in Fig. 9.6 in which the region indicated by dashed lines is a control volume and the shaded region is a sub-area. Points i, j and k are nodes of a triangular element. Points a and b are the midpoints of element sides, and point o is the element centroid. Connecting points a, o and b, a sub-area is formed as the shaded region shown in Fig. 9.6. The procedure for forming other sub-areas is analogous.

Integrating Equation 9.12 over a control volume can lead to

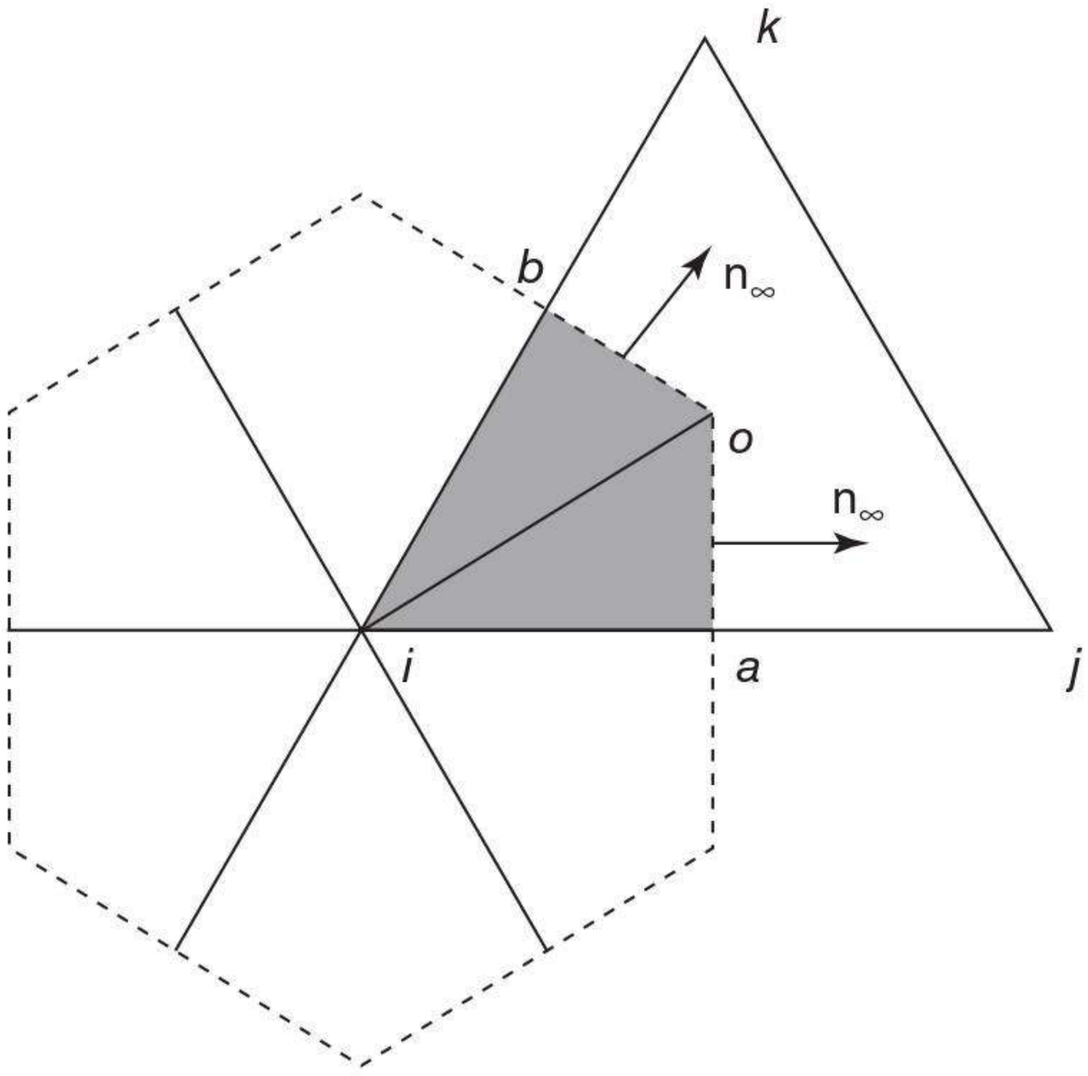

9.6 Control volume.

$$\iiint_V \nabla \cdot \left(-\frac{1}{}\begin{bmatrix} K_{xx} & K_{xy} \\ K_{yx} & K_{yy} \end{bmatrix} \begin{bmatrix} \dfrac{p}{x} \\ \dfrac{p}{y} \end{bmatrix} \right) \mathrm{d}V = 0 \qquad 9.13$$

By using the divergence theorem, the above equation can be written as

$$\iint_S \left(-\frac{1}{}\begin{bmatrix} K_{xx} & K_{xy} \\ K_{yx} & K_{yy} \end{bmatrix} \begin{bmatrix} \dfrac{p}{x} \\ \dfrac{p}{y} \end{bmatrix} \right) \cdot \mathbf{n}\, \mathrm{d}s = 0 \qquad 9.14$$

or

$$\int_C \frac{h_z}{} \begin{bmatrix} n_x & n_y \end{bmatrix} \begin{bmatrix} K_{xx} & K_{xy} \\ K_{yx} & K_{yy} \end{bmatrix} \begin{bmatrix} \dfrac{p}{x} \\ \dfrac{p}{y} \end{bmatrix} \mathrm{d}L = 0 \qquad 9.15$$

in which h_z is the thickness of the preform, and the line C is along the boundary of the control volume. If a control volume consists of m sub-areas, the integration along C can be divided into m parts. For each part, by the assumption of linear distribution of pressure in the corresponding element, the pressure gradient can be written as (Yong *et al.*, 1991):

$$\begin{bmatrix} \dfrac{\partial p}{\partial x} \\ \dfrac{\partial p}{\partial y} \end{bmatrix} = \frac{1}{2A} \begin{bmatrix} \beta_1 & \beta_2 & \beta_3 \\ \gamma_1 & \gamma_2 & \gamma_3 \end{bmatrix} \begin{bmatrix} P_i \\ P_j \\ P_k \end{bmatrix} \qquad 9.16$$

where A is the area of the element, $\beta_i = y_j - y_k$, $\gamma_i = x_k - x_j$, and i, j and k permute in natural order.

Then the total integration of Equation 9.15 can be expressed as:

$$\sum_{i=1}^{m}\left\{\frac{h_z}{2A}\left\{l_{ao}\begin{bmatrix}n_x & n_y\end{bmatrix}_{ao} + l_{bo}\begin{bmatrix}n_x & n_y\end{bmatrix}_{bo}\right\}\cdot\begin{bmatrix}K_{xx} & K_{xy}\\ K_{yx} & K_{yy}\end{bmatrix}\begin{bmatrix}\beta_1 & \beta_2 & \beta_3\\ \gamma_1 & \gamma_2 & \gamma_3\end{bmatrix}\begin{bmatrix}P_i\\ P_j\\ P_k\end{bmatrix}\right\} = 0 \qquad 9.17$$

where, l_{ao} and l_{bo} are length between points a and o, and b and o. Equation 9.17 is a linear algebraic equation, which can be written for all control volumes in the flow field. Together with the boundary condition, the pressure distribution in the flow field can then be solved.

Once the pressure field is determined, the velocity can be evaluated according to Equation 9.11; the flow front is then advanced using the FAN technique (Frederick and Phelan, 1997). In this method, the whole domain is divided into a fixed grid system and a scalar parameter f is introduced for each cell to represent the ratio of occupied volume to the total volume. As the flow front advances, all of the control volumes can be classified into three categories (see Fig. 9.7) as follows:

$f = 1$: filled region
$0 < f < 1$: flow front region
$f = 0$: empty region

For a selected volume $f\,(0 < f < 1)$ is calculated on the basis of the velocity field. The calculated volume of resin inflow is added to the original volume of resin in the flow front control volume. If the total resin volume in a control volume is equal to the volume of the control volume, that control volume is considered 'full' ($f = 1$). The time increment is selected in such a way that one control volume can be filled simultaneously. This restriction of the time increment ensures the stability of the quasi-steady-state approximation. The new flow front in each time step can be estimated according to the velocity vector in the flow front and the time increment after the pressure field is determined. After the value f is updated, another pressure

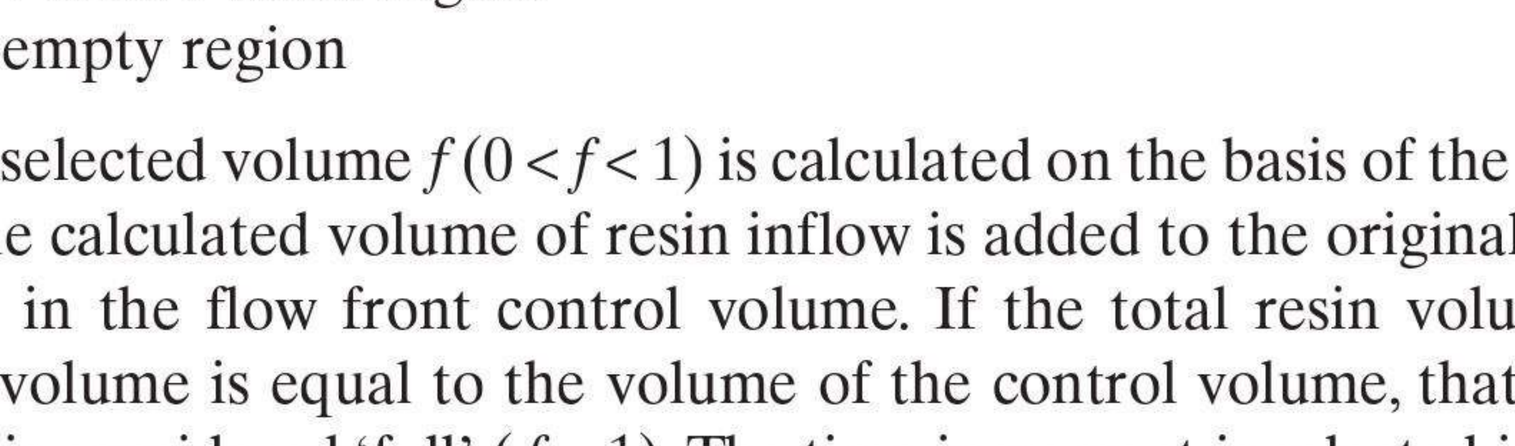

9.7 Illustration of the flow front advancing technique.

computation is performed for all the control volumes with $f = 1$. The procedure is repeated until the whole mould cavity is filled.

The time increment is determined in such a way that only one control volume is fully filled during the step, then

$$\Delta t = \min\left(\frac{V_i - V_i^{\mathrm{f}}(t)}{Q_i(t)}\right) \tag{9.18}$$

where V_i is the volume of control volume i, $V\mathrm{fi}(t)$ is the filled volume at time t, and $Q_i(t)$ is the flow rate into the control volume. Once the time increment is determined, the volume of fluid that flows into each control volume at the flow front can be calculated. Then the flow front is advanced.

$$f_i(t + \Delta t) = \frac{V_i^{\mathrm{f}}(t) + \Delta t \cdot Q_i(t)}{V_i} \tag{9.19}$$

A detailed flowchart of the numerical implementation is given in Fig. 9.8.

The numerical scheme outlined above has been implemented and tested by comparison with mould filling cases for which analytical solutions exist. The first case tested was boundary injection from one side of a rectangular mould: see Fig. 9.9. For constant injection pressure, the flow front position x_{f} at time t can be given by

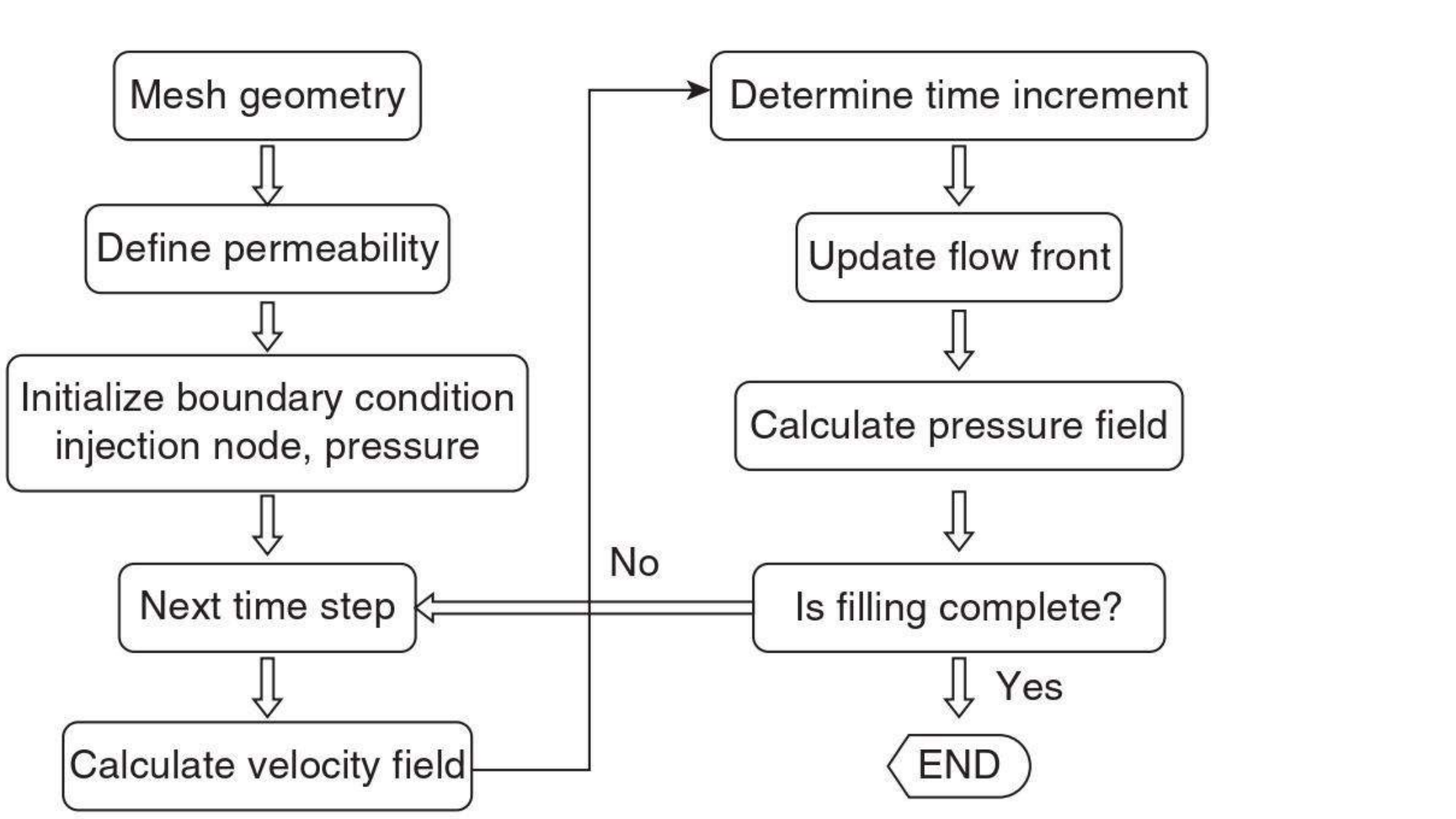

9.8 Flowchart of the numerical simulation using the control-volume method.

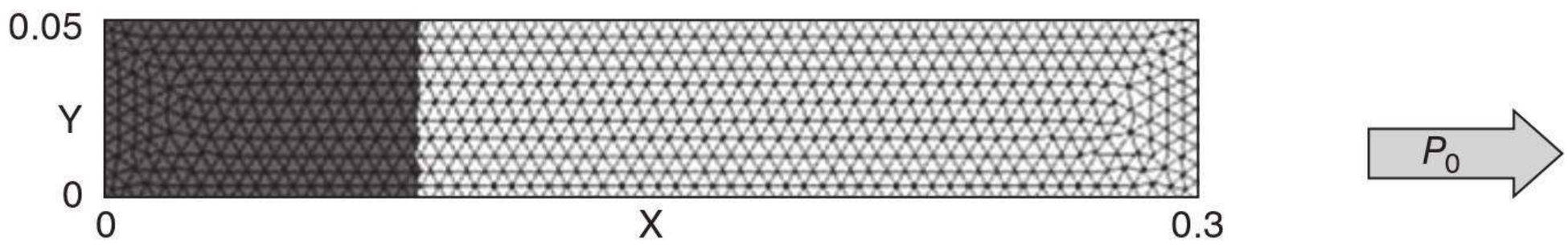

9.9 Boundary injection from one side of a rectangular mould.

$$x_f = \sqrt{\frac{2KP_0t}{}} \tag{9.20}$$

where P_0 is the injection pressure, K is the permeability of the preform, and μ is the viscosity of the fluid. Simulation was conducted for $P_0 = 200$ kPa, $K = 1.0 \times 10^{-10}$ m^2 and $\mu = 0.01$ Pa s. Predictions of flow front by simulation were in perfect agreement with the analytical results as shown in Fig. 9.10.

The second case tested was point injection from the centre of a square preform. The resin will flow in radial directions from the centre towards the preform edges. This results in an elliptical flow front, and the ratio a/b of its major axis to the minor axis is always equal to $\sqrt{K_1/K_2}$, where K_1 and K_2 are the principal permeabilities of the preform in two directions. The numerically simulated shapes of the flow front are shown in Fig. 9.11. For Fig. 9.11(a), there is $K_1 = K_2 = 1.0 \times 10^{-10}$ m^2; for Fig. 9.11(b), there is

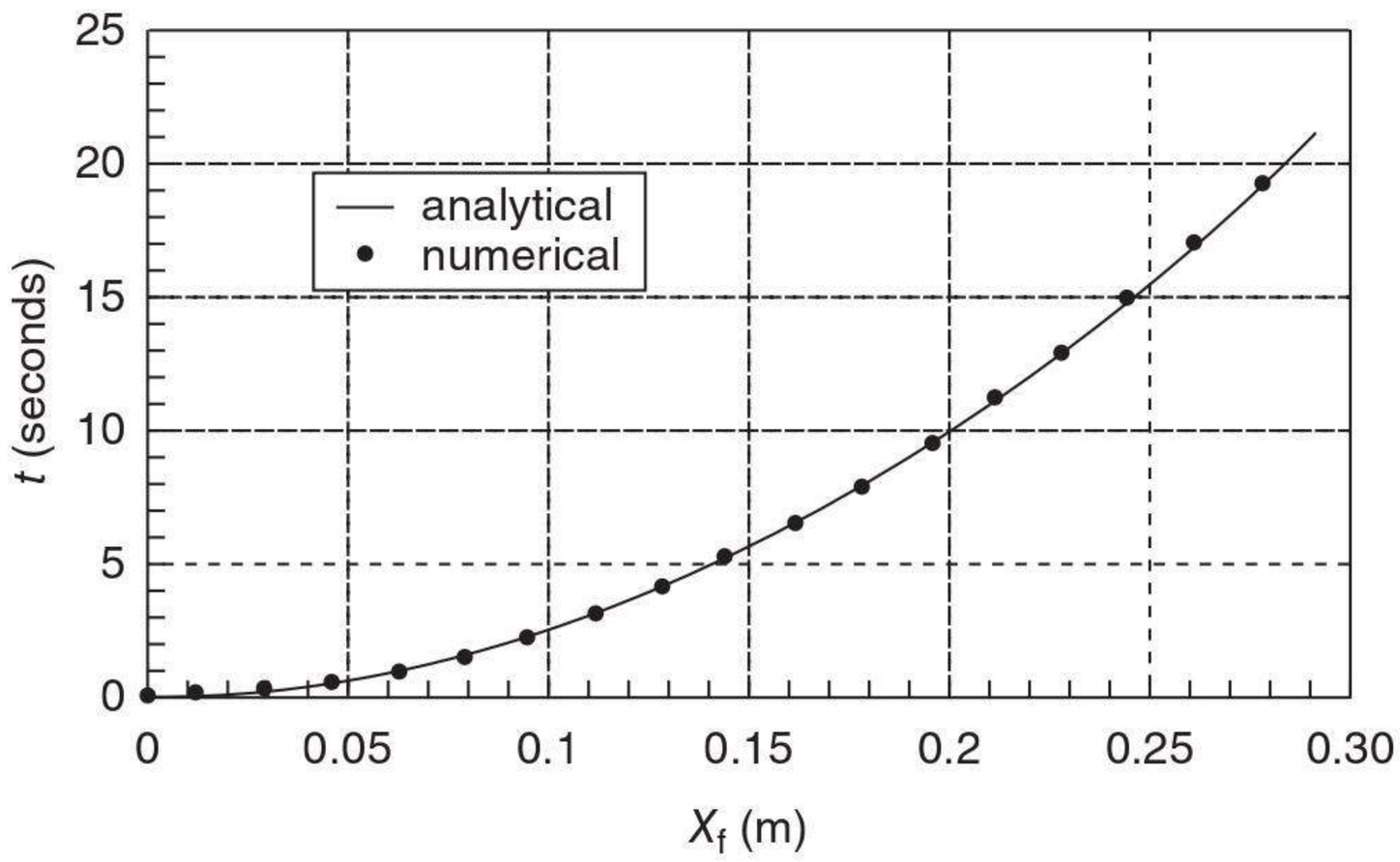

9.10 Comparison of analytical and numerical results of flow fronts.

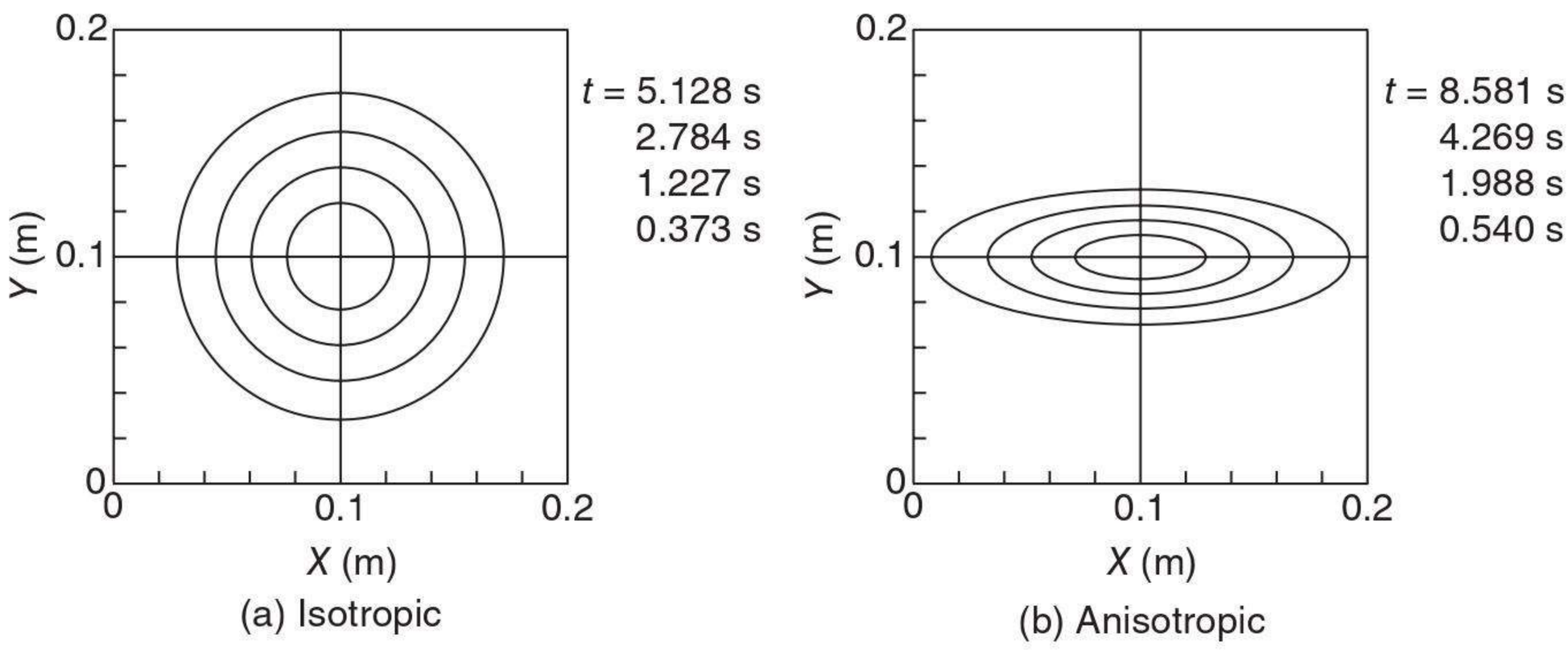

9.11 Flow fronts at different injection times of point injection in a square preform.

$K_1 = 1.0 \times 10^{-10}$ m^2, $K_2 = 1.0 \times 10^{-11}$ m^2. Excellent agreement can be observed between the numerical and analytical results for *a/b*.

It is noted that the flow fronts by simulation shown in Fig. 9.11 are not very smooth. The reason is that the flow front is identified by the filling factors on a fixed mesh, and it can be tacked to the resolution by using more elements in the flow domain.

9.4.1 Void formation in multilayer woven fabrics

In this section, the mould filling process and void formation in both unit cells of MWFs were simulated using the above numerical scheme. The fluid employed in the simulations was silicone oil of viscosity 0.1934 Pa s, which was taken from the experimental study of Patel and Lee (1995).

As described in section 9.2, since the thickness of the fibre tow is far less than the width, the unit cell of mode I (Fig. 9.4(a)) can be further simplified to Fig. 9.12, a cell with rectangular cross-section for both channel and warp/weft. This simplification was used by Yu and Lee to develop an in-plane permeability model of MWFs (Yu and Lee, 2000). Then a symmetry boundary condition can be imposed for the simulation of flow in both unit cells.

In order to define different permeabilities for different sub-domains, the flow field was first meshed by sub-domain to sub-domain using software ANSYS 5.7. In the simulation of the filling process, the boundary condition at the inlet can be either a constant volumetric flow rate or a constant injection pressure. Here, a constant injection pressure was taken. The pressures at inlet and flow front were set to be 5×10^5 Pa and 1×10^5 Pa, respectively. The fibre tows for weft and warp were the same with a fibre volume fraction of $V_{fb} = 0.45$ and a fibre radius of $r_f = 8 \times 10^{-6}$ m. Then the permeabilities of the fibre tow evaluated according to the Carman–Kozeny equation were $K_b^a = 2.63 \times 10^{-11}$ m^2 and $K_b^t = 1.32 \times 10^{-12}$ m^2.

Figure 9.13 shows the numerical simulation of flow fronts at various filling stages. The flow patterns in both unit cells are consistent with the analysis in section 9.2. In both unit cells, voids were formed at the ends of warp and the primary reason for void formation is the large difference in permeability between K_c, K_b^a and K_b^t. It can be observed that the void formed in the unit cell of mode I is smaller than that of mode II for the same parameters. This is understandable because there is only one warp between two adjacent

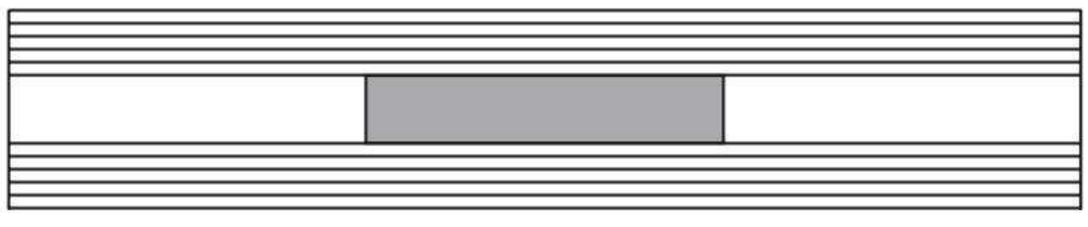

9.12 Simplified unit cells for mode I.

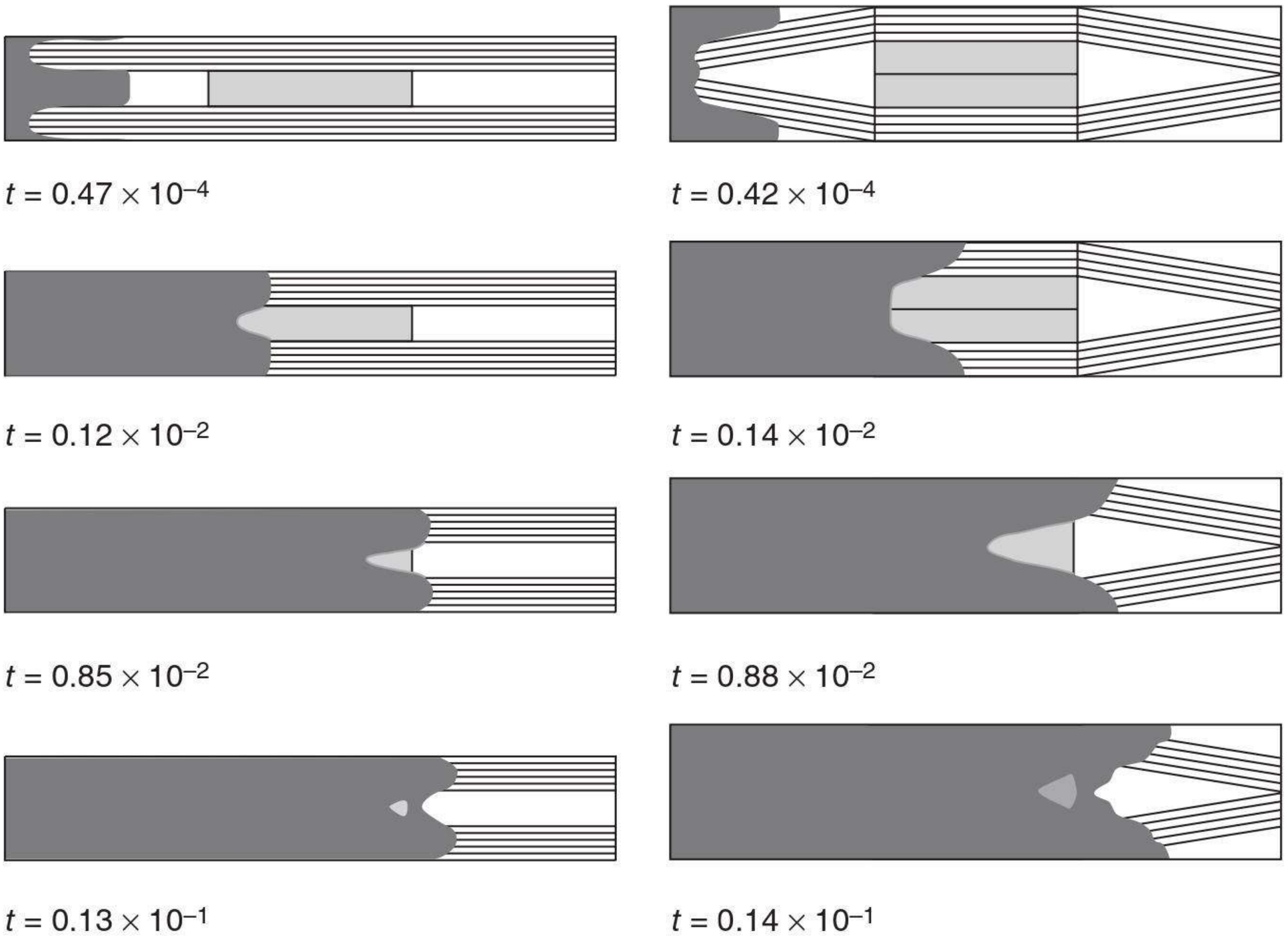

(a) Flow fronts in unit cell of mode I (b) Flow fronts in unit cell of mode II

9.13 Flow fronts at different stages of mould filling.

wefts in mode I, but two for mode II. Thus, the impregnation in the warp of mode I is much accelerated by the relatively high flow velocity in adjacent wefts. Furthermore, the channel before warp in mode II is triangle-shaped, which also makes the flow in path 2 of mode II slower than that of mode I.

It is also noted that the simulated time for voids to be formed at the ends of warp, namely the time for the flow front in path 1 to reach position B, is less than that predicted according to Equation 9.5. This is because the impregnation in the weft between two adjacent warps is accelerated due the high permeability in the channel. In Equation 9.5, this effect is not considered.

According to the analytical result for the time ratio T_1/T_2, it can be observed that K_b^a/K_b^t seems to determine the size of the void. In this study, void formation processes on different values of K_b^a/K_b^t were simulated. Figure 9.14 presents the effect of changing K_b^a/K_b^t on the void size for both unit cells, which shows that larger K_b^a/K_b^t corresponds to larger void size. In addition, it seems that the size of void is proportional to the ratio of K_b^a/K_b^t as shown in Fig. 9.14. This agrees with our analytical result in section 9.2.

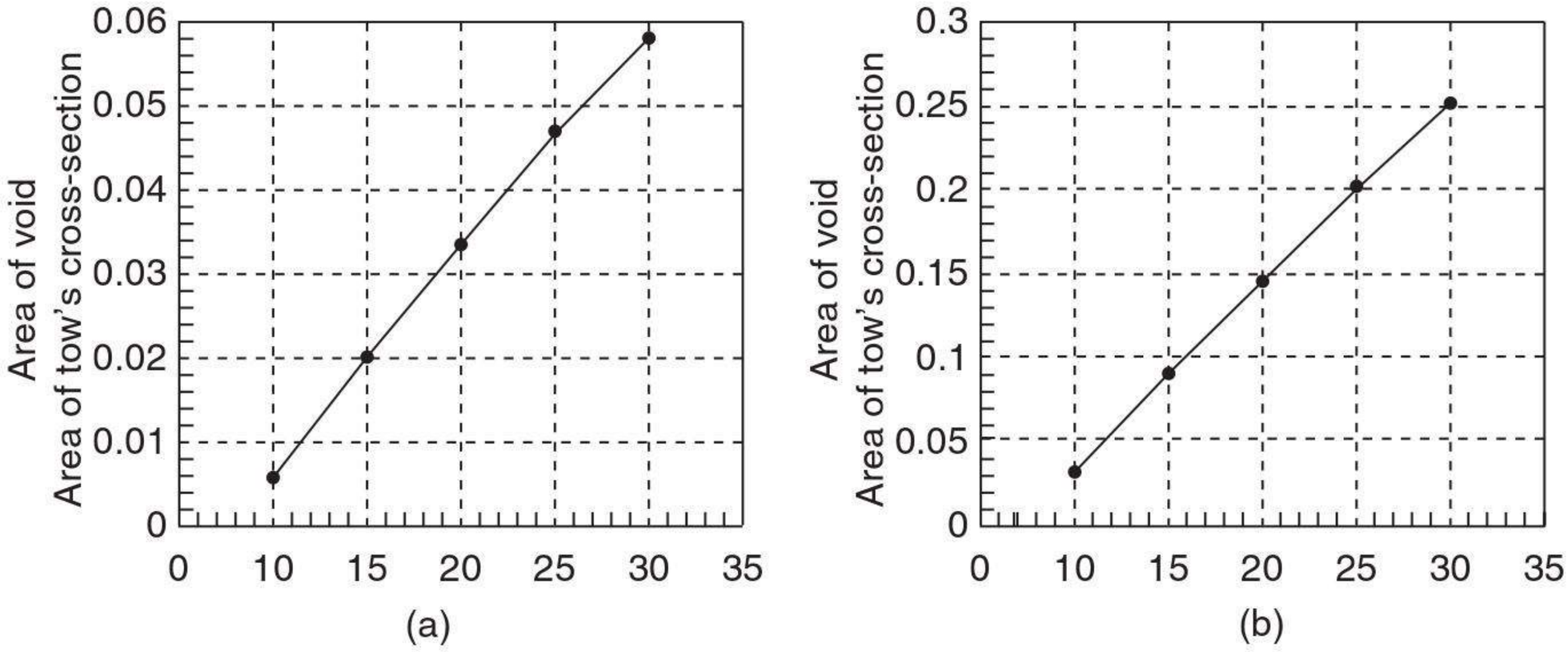

9.14 Size of void for different values of K_b^a/K_b^t. (a) unit cell of mode I, (b) unit cell of mode II.

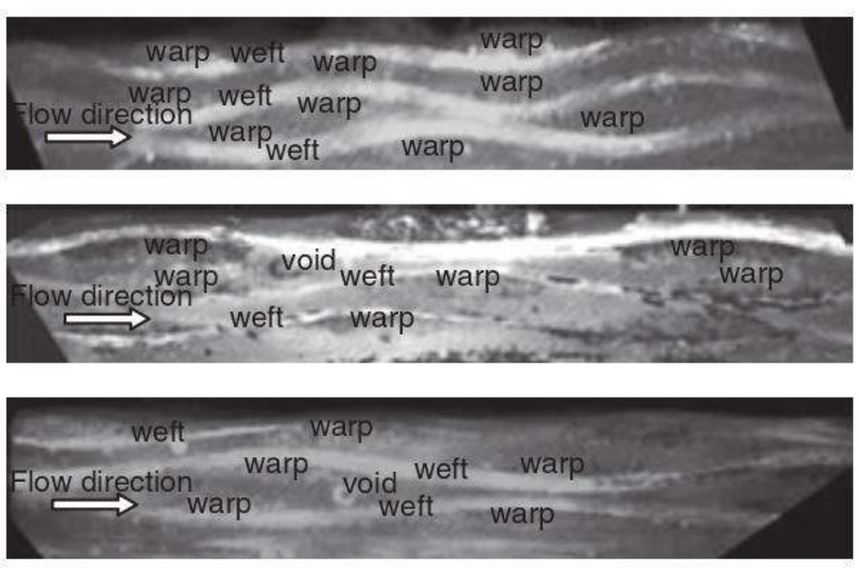

9.15 Experimental cross-sections of MWFs.

9.4.2 Experimental results

Experiments were performed to measure the formation of voids and their location. The reinforcement used in this experiment is plain woven fabrics. Three plies of glass fibre mat were stacked with low fibre volume fraction. The resin used was a two-part epoxy/amine resin, LY564/HY2954, from Ciba-Geigy (Hawthorne, NY). LY564 is the base resin of a bisphenol, an epoxy containing a reactive diluent. HY2954 is a hardener of 3,3′-dimethyl-4,4′-diaminodicyclohexyl methane. The mix ratio of LY564 to HY2954 (parts by weight) was 100:35. The resin had a viscosity of 0.617 Pa s at 25°C.

Resin was injected at constant pressure (0.5 MPa) into the mould. The longitudinal cross-section was examined using a microscope as shown in Fig. 9.15. From these images, two typical modes of the plain woven fabric can be clearly recognized and the formation of voids is mainly located at the end of warp.

9.5 Modelling the effect of stitch size, distribution and position

A key feature of 3-D multilayer woven fabrics is their interbundle stitches, but very limited information is available on the relationship between permeability and the effect of stitches. Shih and Lee (1998) proposed a parallel permeability model for flow through bidirectional stitched fabrics. The flow between the bundles is set by the Kozeny–Carman equation (Carman, 1937), and the effect of stitch was not specially mentioned in Shih and Lee's paper. Cairns *et al.* (1999) developed a model that incorporates Darcy's law within fibrous bundles and channels that exist between bundles. The paper reported that incorporating channel flow is an important feature for properly modelling the RTM process. With this model, pressure profiles, resin velocities and resin flow fronts are predicted accurately, and are available for manufacturing process development. The same materials were compared to fully stitched preforms. It was found that although the shapes for resin flow are similar between the experimental and analytical results, the stitch affects the permeability such that the unidirectional ply data do not accurately capture the times for resin flow.

Lundström (2000) also proposed a model for non-crimp stitched fabrics through theoretical analysis. The interbundle channel was assumed to be rectangularly shaped and the equivalent permeability is modelled by Equation 9.1. A comparison between the model and experimental data shows that this model works well in certain cases, while it fails in other cases to predict the permeability perfectly. Lundström suggested that one of the main reasons for the discrepancy was the assumption that the effect of stitch was negligible. Lundström also mentioned that study of both the dry fabric and the impregnated samples yielded stitches that were actually located in some of the channels. It is really important to make a quantitative study of the issue as to how stitches affect the effectiveness of the permeability. Such a study will be very helpful for designing stitched fabrics, exact pre-simulation of moulding processes, and the optimization of processing parameters.

The structure of 3-D multilayer woven fabrics is quite complicated and variable. In this section, we focus on its key feature, the interbundle stitch, and its effect on permeability. Several typical stitch structures were selected as the basic models, and the effect of stitches on permeability of the interbundle channel has been investigated through numerical simulation for various combinations of the stitch size, its off-centre position, slope, array, distribution density in the flow direction and the average Darcy velocity in the fibre bundle.

The results of numerical simulation are presented in this section. The effect of stitches on the equivalent permeability of the interbundle channel

is presented by the value of K/K_0 where K and K_0 are the permeabilities of the channels with and without stitches, respectively. It should be particularly noted that K_0 is different for different boundary conditions and geometrical structures (Hu *et al.*, 2003).

9.5.1 The effect of stitch size on distribution density

In this section, we consider that there is only one stitch in one representative cell, and the stitch is located on the centreline of the channel and perpendicular to the flow direction. The corresponding computational cell is shown in Fig. 9.1(a). Based on this computational cell, the effect of stitch on the permeability of the interbundle channel has been investigated for various combinations of stitch size (R/a), distribution density in the flow direction (L/W), and the ratio of V_b to V_a, in which $V_a = Q/A$ is the average velocity in the channel corresponding to the given flow rate.

Figure 9.16 shows the variation of K/K_0 with R/a for different boundary conditions and distribution densities. As shown in these figures, it is evident that stitches may severely influence the permeability of the interbundle channel. For all simulated cases, the value of K/K_0 is less than 0.80 at $R/a = 0.1$, and is around 0.10 at $R/a = 0.6$. Obviously, the effect of stitches cannot be neglected when establishing an effective permeability model. We also note that there is similar variation of K/K_0 with R/a for different conditions, but the extent of the influence is different for different boundary conditions or different distribution densities.

In Fig. 9.17, the variation of K/K_0 with V_b/V_a for different values of R/a and the same L/W is presented. For all simulated cases, K/K_0 decreases with increasing V_b/V_a, especially for boundary condition BC3, where the effect of V_b/V_a on the value of K/K_0 is much higher than that for BC2. The value of K/K_0 is reduced about 50% when V_b/V_a is increased from 0.1 to 0.8 for BC3. Thus, the effect of stitches on the permeability of the interbundle channel is different with different boundary conditions. It is known that, for a given pressure drop Δp, the larger the average flow velocity V_b in the fibre bundle, the higher the permeability.

The stitch distribution density in the flow direction is expressed by the value of L/W. If W is kept constant, then larger L/W means sparser distribution. The effect of L/W on the value of K/K_0 is shown in Fig. 9.18. There is a fairly linear relationship between K/K_0 and R/a, but the slope of change is different for different cases. For the same boundary condition, the slope decreases with increasing R/a. This means that the effect of stitch distribution density decreases with increase of R/a.

All the simulations are performed with the condition that channel height H is equal to width W. Certainly, the variation of H may affect the value of K/K_0. When H tends to infinity, the flow in the channel can be simplified

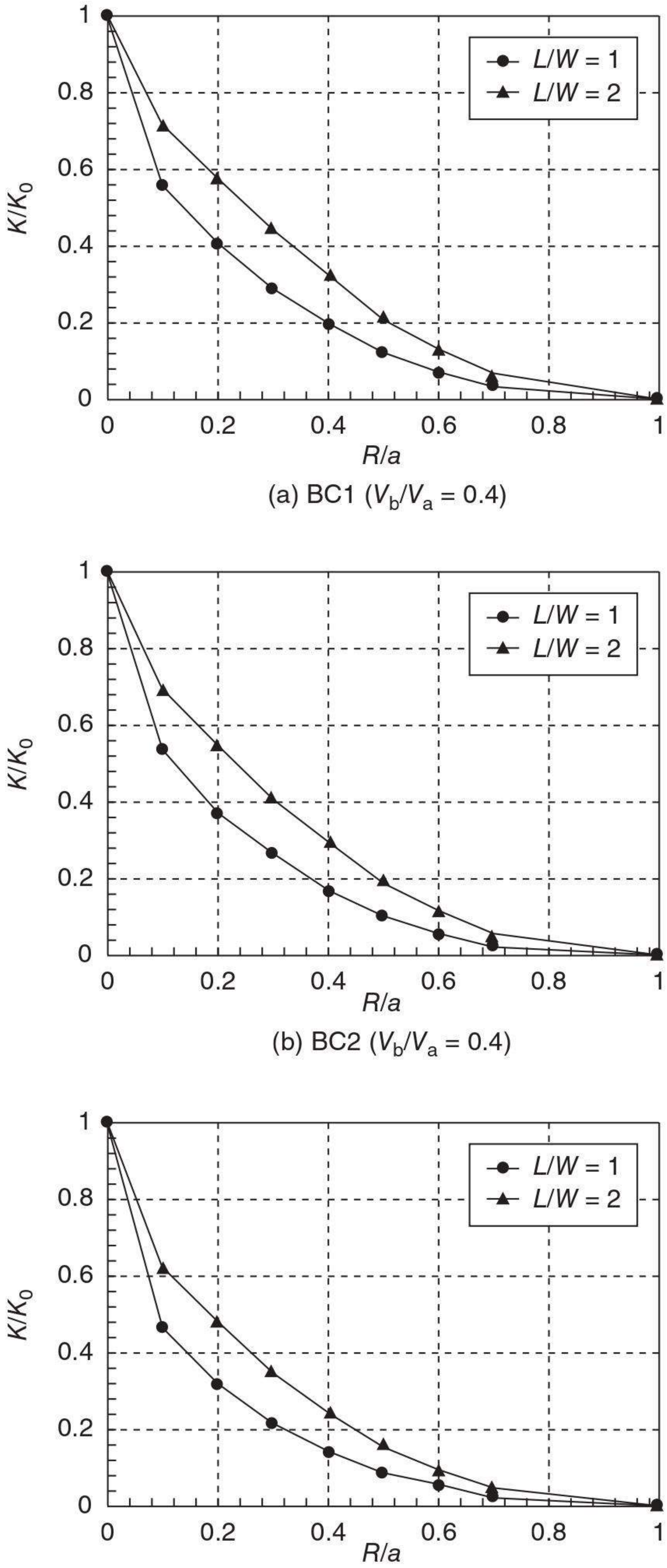

(a) BC1 ($V_b/V_a = 0.4$)

(b) BC2 ($V_b/V_a = 0.4$)

(c) BC3 ($V_b/V_a = 0.4$)

9.16 Change of K/K_0 with R/a on different boundary conditions.

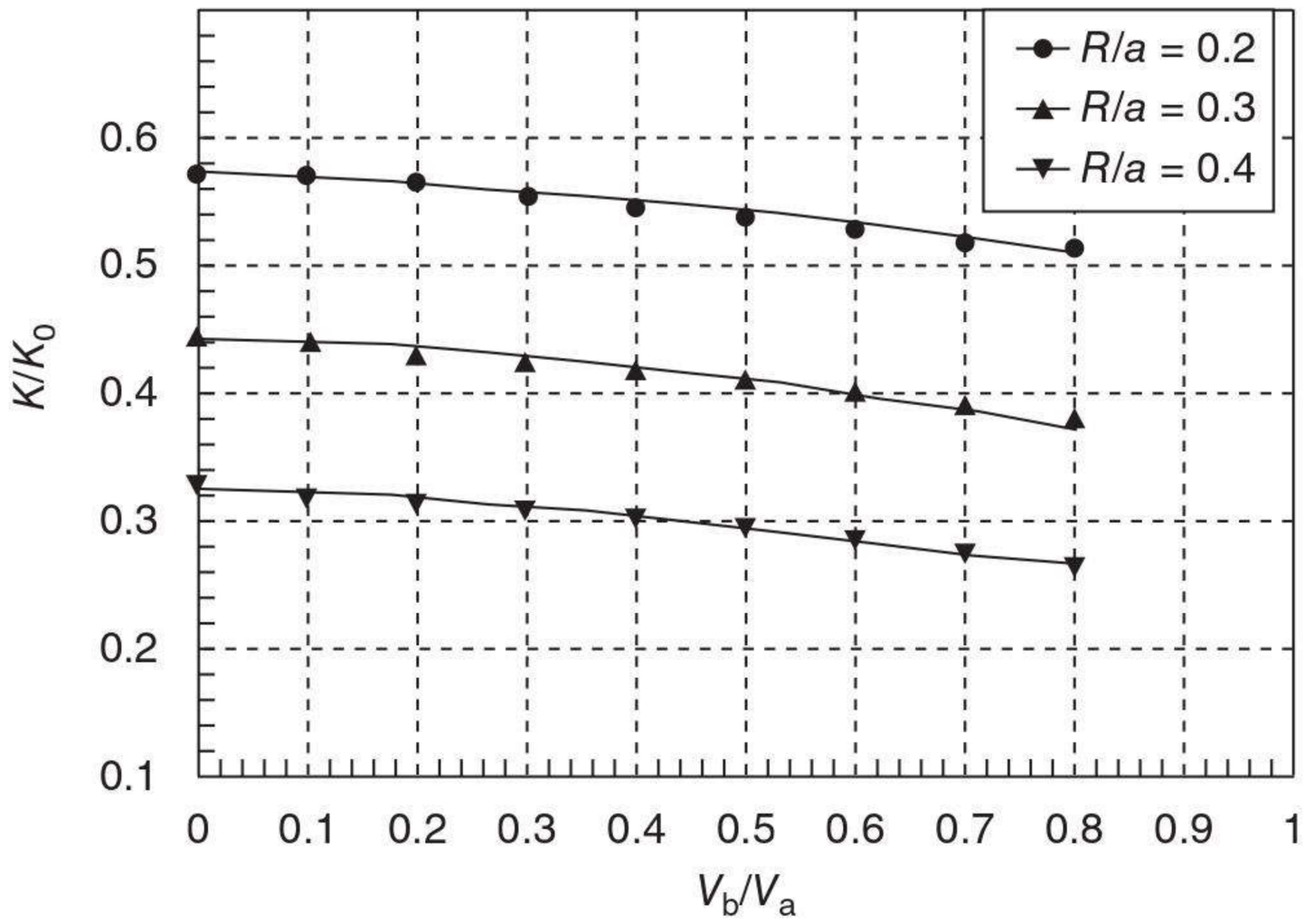

(a) BC2 (L/W = 2.0)

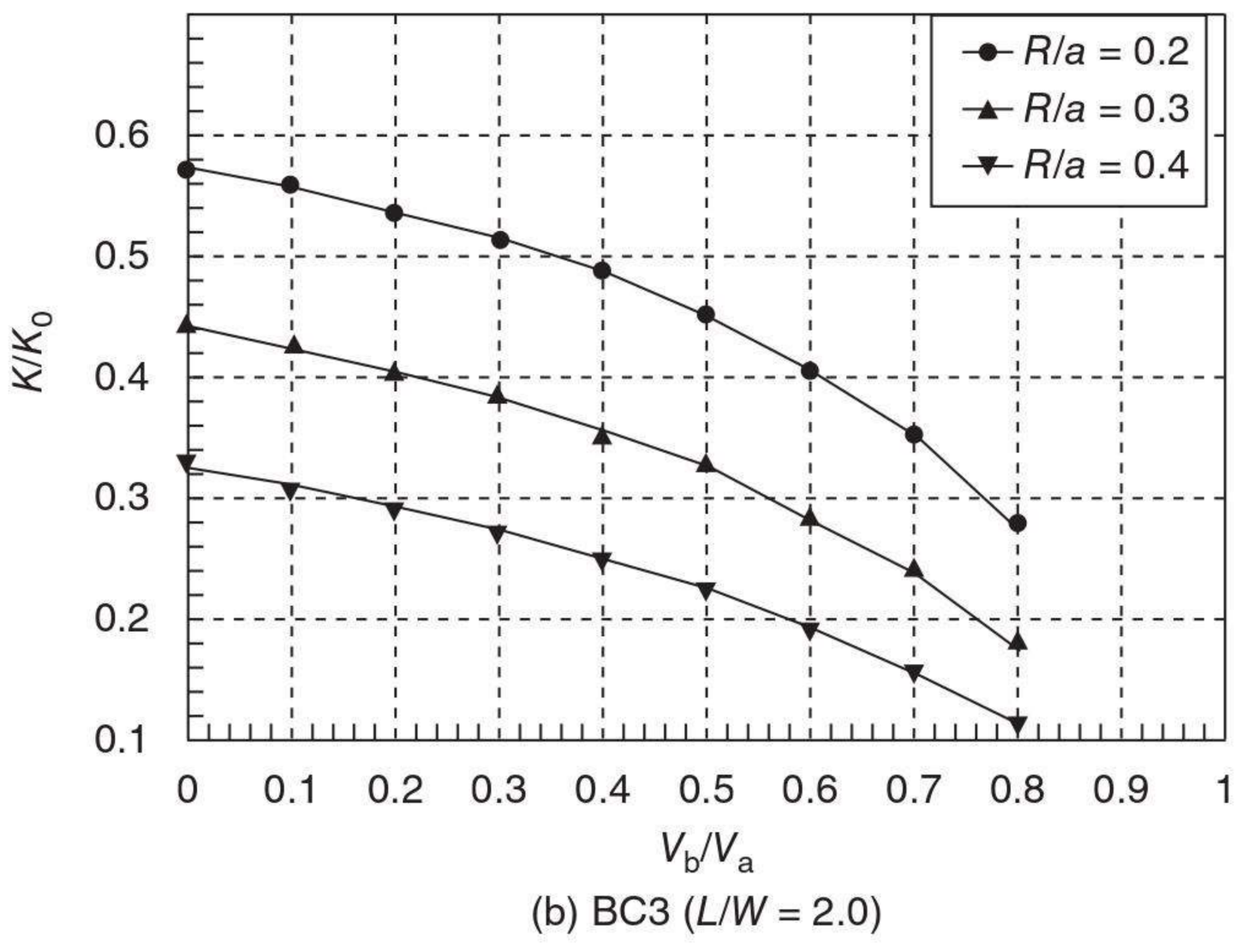

(b) BC3 (L/W = 2.0)

9.17 Change of K/K_0 with V_b/V_a for boundary conditions BC2 and BC3.

into a 2-D model as shown in Fig. 9.16(b). In this study, some cases based on a 2-D model are also simulated and the results are shown in Fig. 9.19. Comparing them with the corresponding results in Fig. 9.16, we find that the trend of K/K_0 varying with R/a is the same, i.e. K/K_0 decreases with increasing of R/a when other parameters are kept constant.

The impregnation process for different stitch radii was also simulated by finite element simulation. The schematic of the simulation unit cell is shown in Fig. 9.20 where the effect of stitch size is represented by the ratio between the stitch radius and the channel length (R/a). Based on the finite element method, the impregnation process of resin flow through the unit cell of the

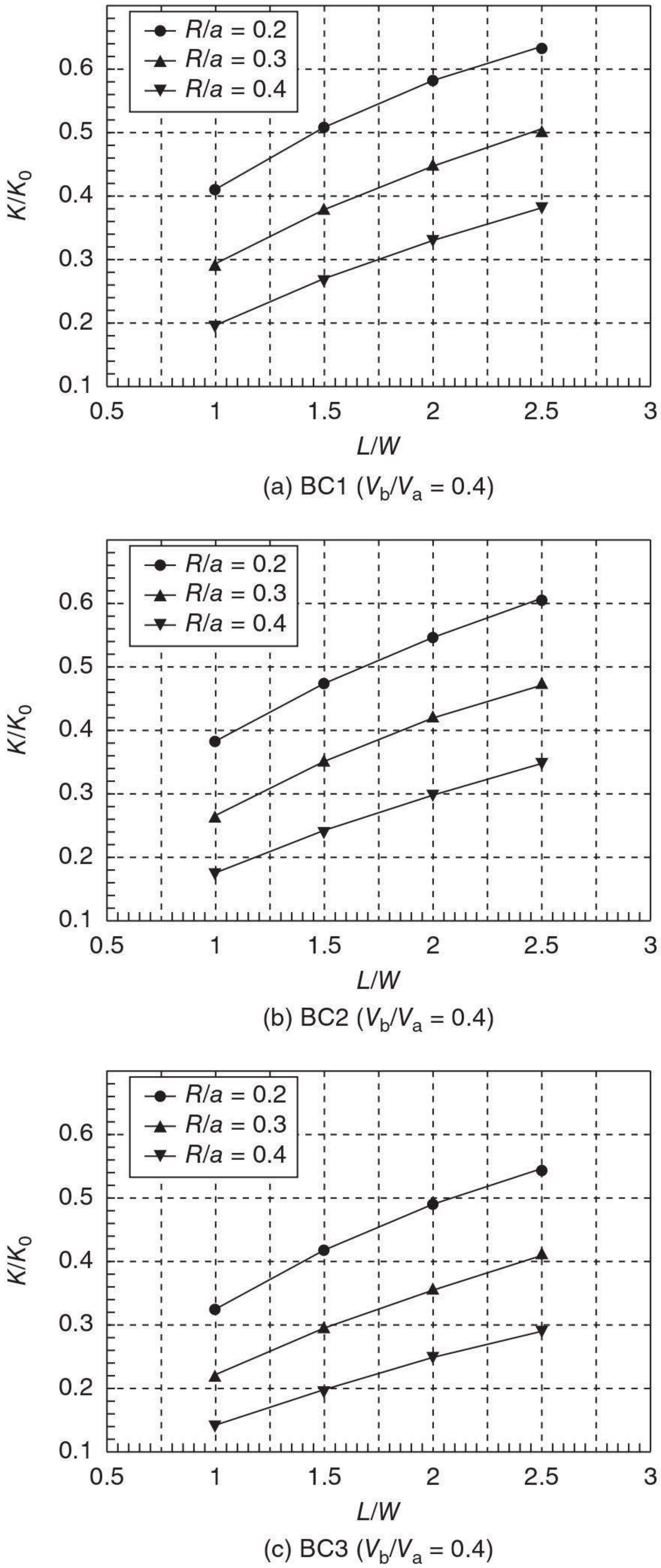

(a) BC1 ($V_b/V_a = 0.4$)

(b) BC2 ($V_b/V_a = 0.4$)

(c) BC3 ($V_b/V_a = 0.4$)

9.18 Change of K/K_0 with L/W on different boundary conditions.

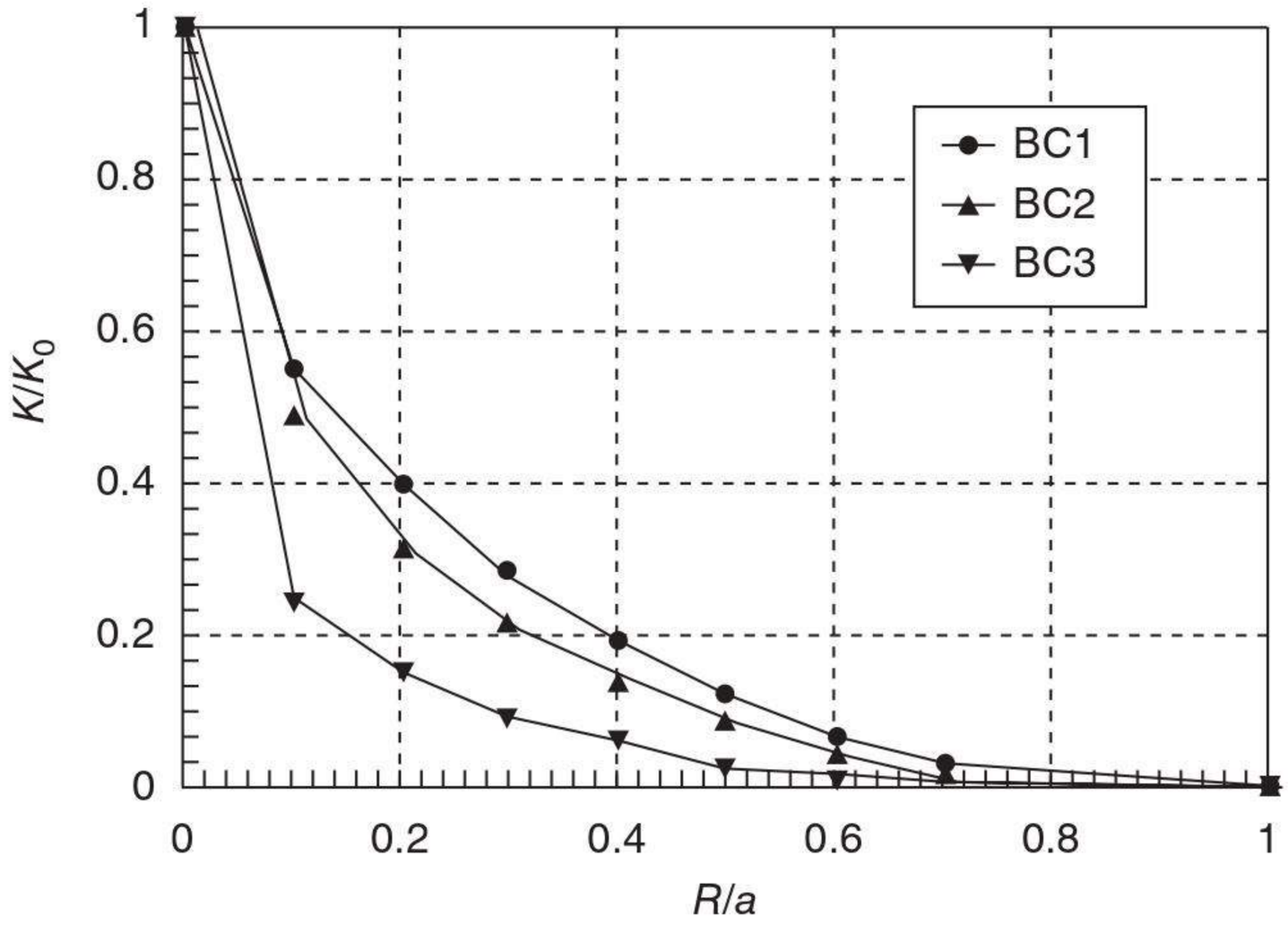

9.19 Results of 2-D simulation: change of K/K_0 with R/a ($L/W = 2.0$, $V_b/V_a = 0.4$).

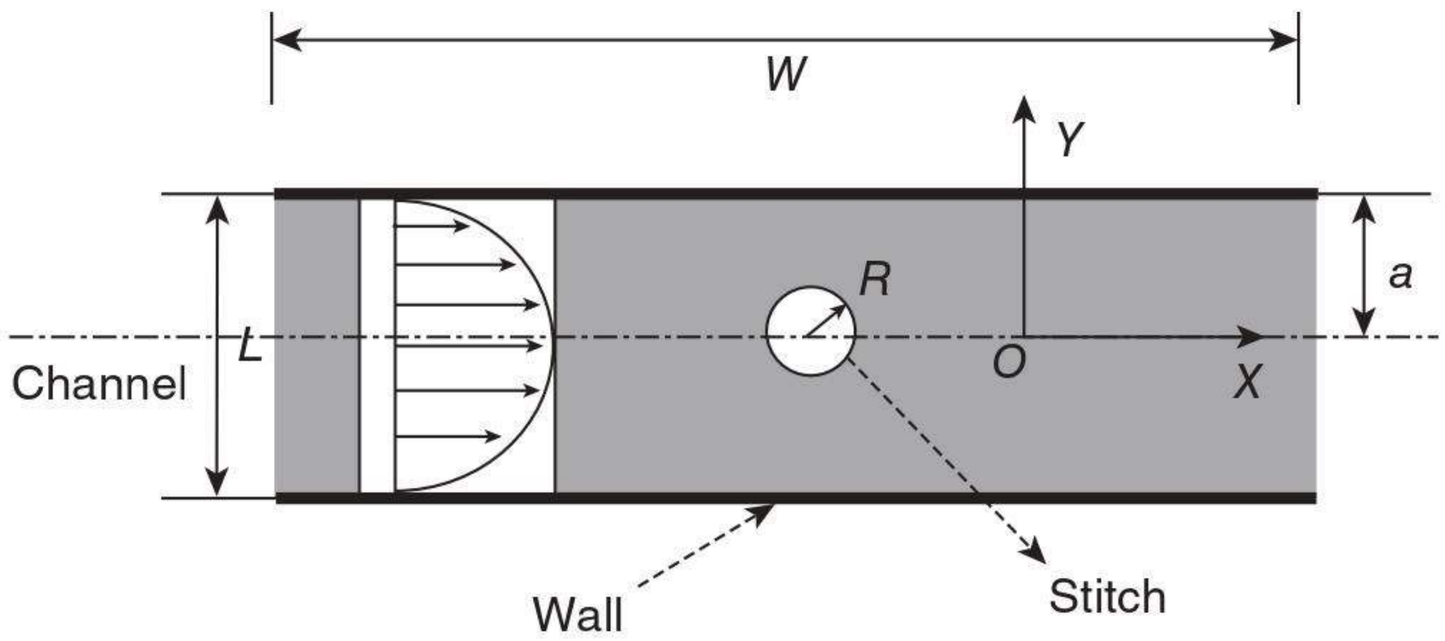

9.20 Unit cell of channel flow with different stitch sizes.

channel with stitch in the off-centre position is shown in the following simulation (Fig. 9.21).

9.5.2 The effect of stitch size on permeability

The effect of stitches on the equivalent permeability of the interbundle channel is represented by the value of K/K_0. The effect of stitch size on permeability is shown in Fig. 9.22, in which the x-coordinate is R/a, where R is the stitch radius and a is the channel width. As shown in Fig. 9.22, it is evident that stitch size may severely influence the permeability of the interbundle channel. The permeability decreases quickly with increase of stitch radius. These simulation results also correspond with the results of analysis by FLUENT as shown in Fig. 9.16.

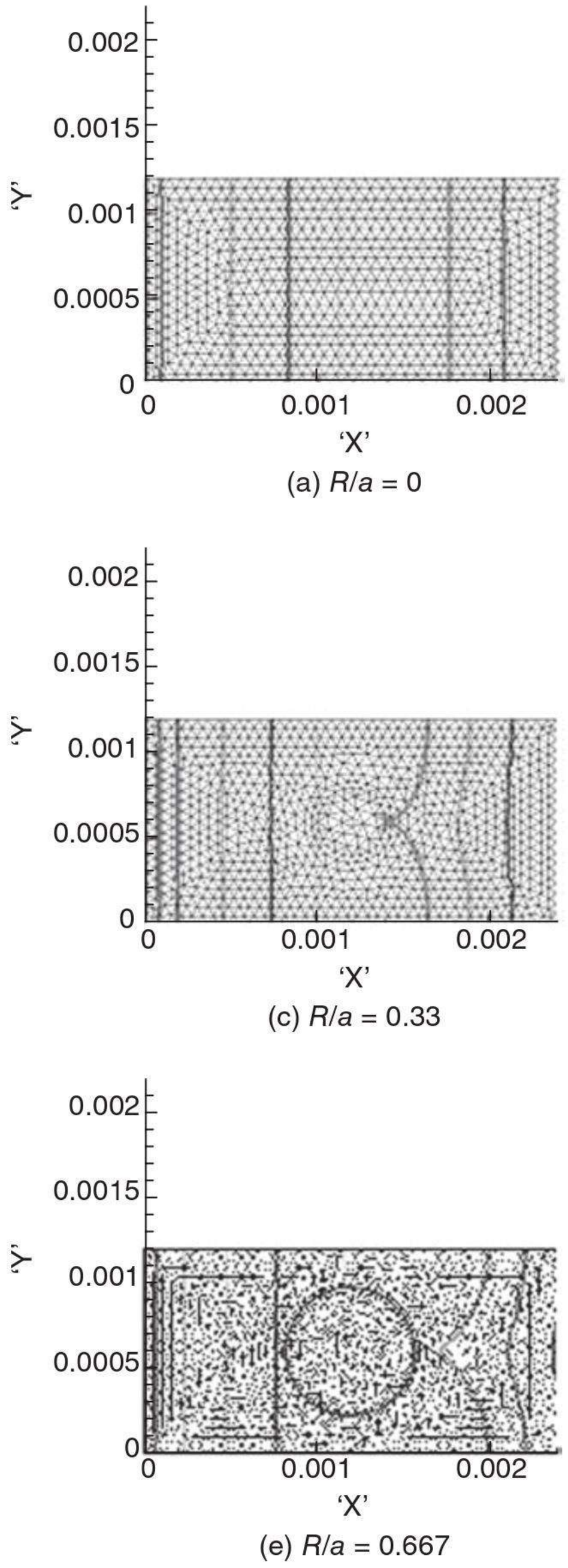

(a) $R/a = 0$

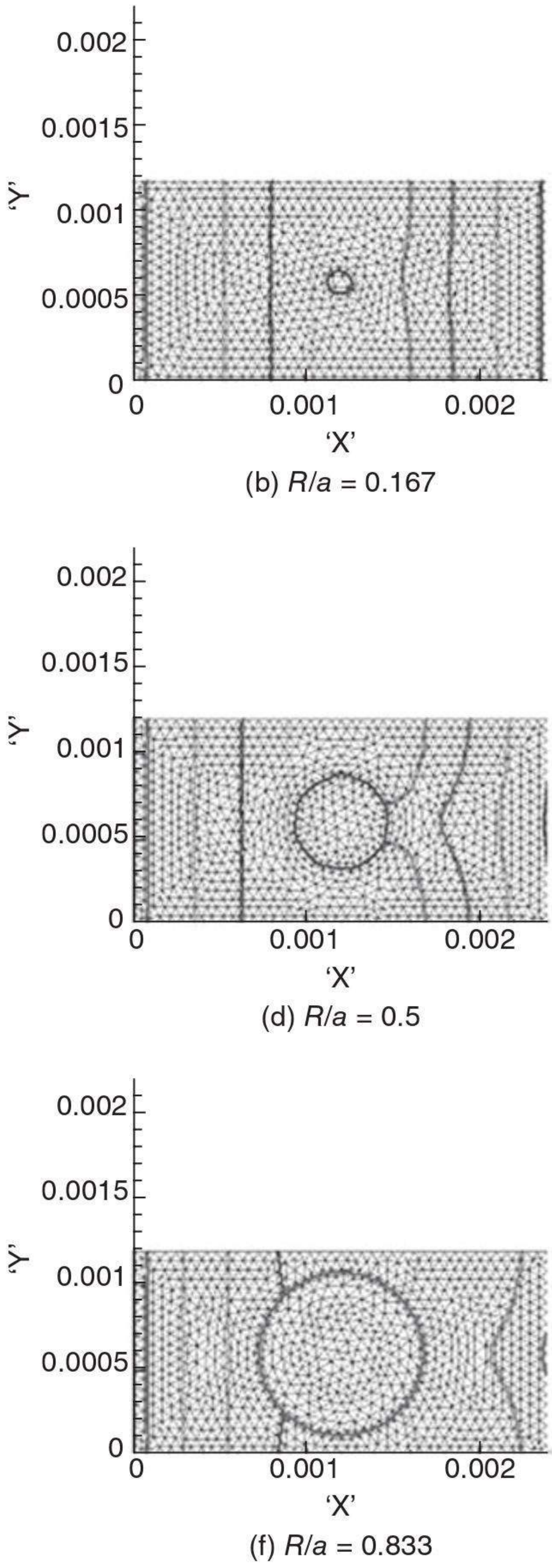

(b) $R/a = 0.167$

(c) $R/a = 0.33$

(d) $R/a = 0.5$

(e) $R/a = 0.667$

(f) $R/a = 0.833$

9.21 The simulation impregnation process of resin flow through the unit cell of the channel with different stitch sizes.

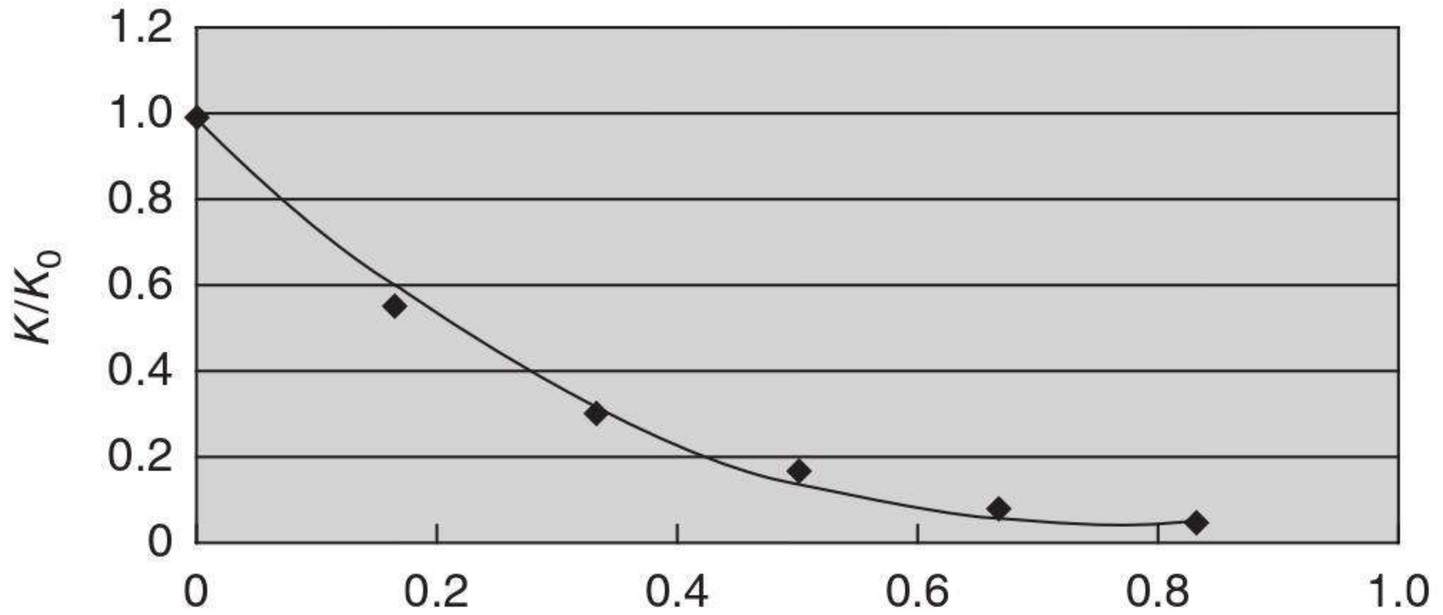

9.22 The effect of stitch size on permeability.

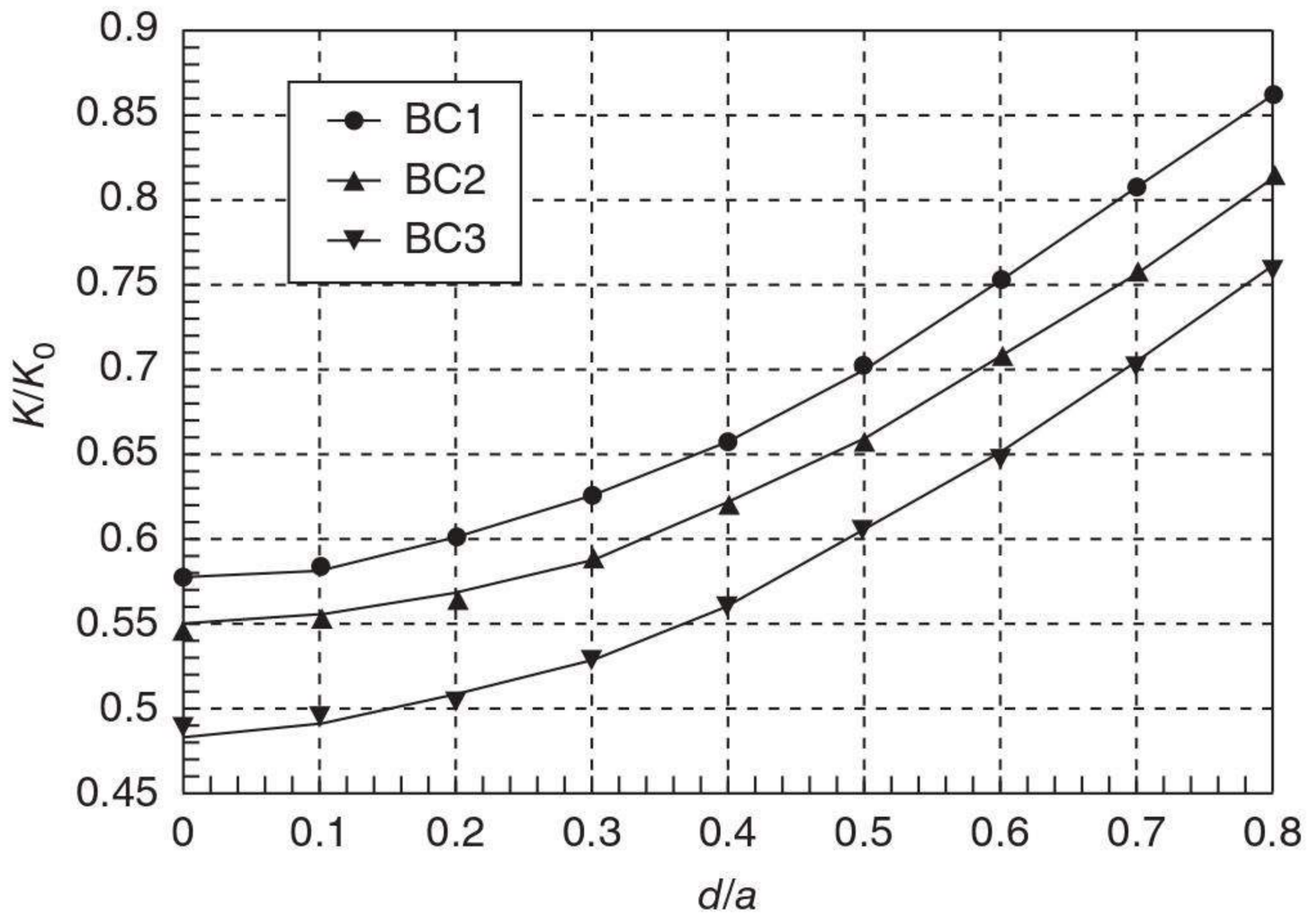

9.23 Change of K/K_0 with d/a.

9.5.3 The effect of stitch off-centre position in channel

Stitches in the interbundle channel do not always lie on the centreline. They are often off-centre. In this case, the upper half of the channel is selected as the computational cell. The simulation results are shown in Fig. 9.23, in which the x-coordinate is d/a where d is the distance between the stitch centre and the channel centreline. For the other parameters, $R/a = 0.2$, $L/W = 2.0$, and $V_b/V_a = 0.4$. Apparently, the effect of the stitch on the permeability of the channel is very different for different off-centre positions. When d/a increased from 0 to 0.8, i.e. the stitch location was moved from the centreline to close to the wall, the value of K/K_0 increased by about 50%, in other words, the effect decreased by 50%. So if we want to weaken the effect of the stitch on the permeability of the interbundle channels, and then

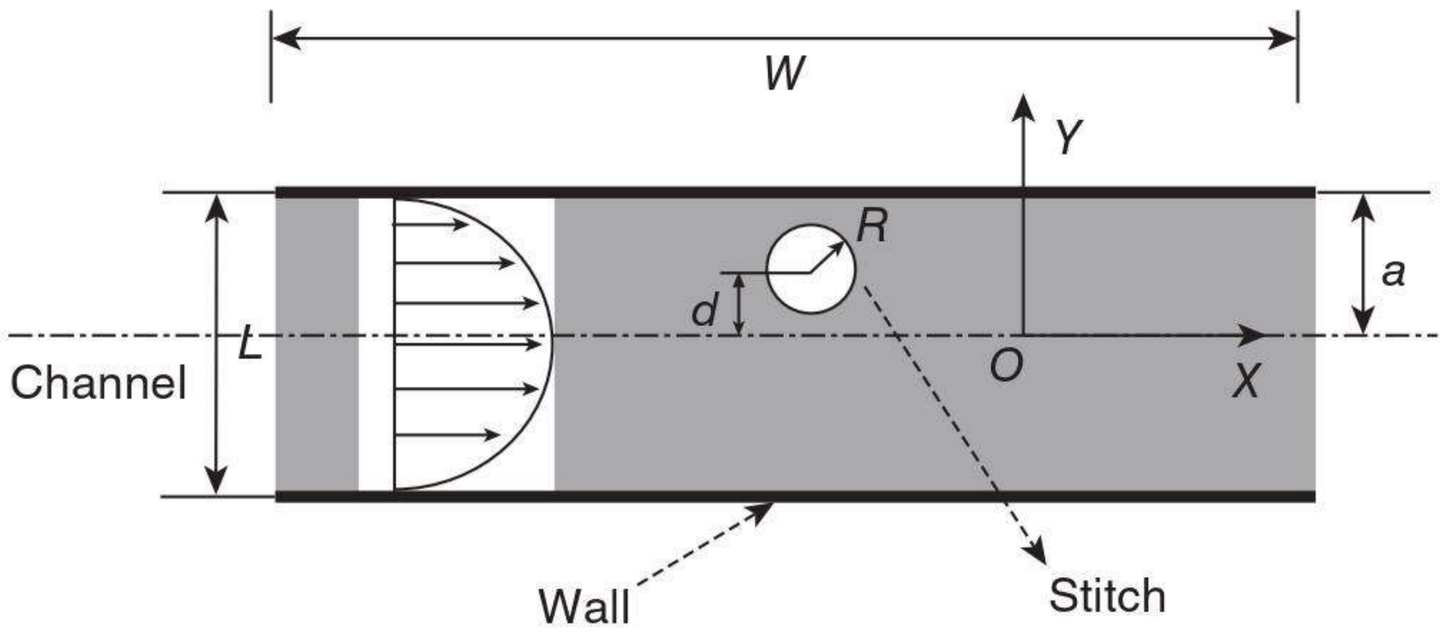

9.24 Unit cell of channel flow with stitch in the off-centre position.

to make the flow of resin in the channel smooth, it is better to keep the stitch off-centre in the interbundle channel.

The effect of the stitch off-centre position in the channel is also further testified by the simulated impregnation process analyzed by the finite element method as follows. A schematic of the simulation unit is shown in Fig. 9.24, where the stitch off-centre position in the channel is represented by the distance between the stitch centre and the channel centreline (d/a). For the simulated case in this section, L/W is 0.5. Based on the finite element method, the impregnation process of resin flow through the unit cell of the channel with stitch in the off-centre position is shown in Fig. 9.25(a)–(f).

Based on Darcy's law, the effective permeability of the unit cell can be calculated from the simulation impregnation process. The effect of stitches on the equivalent permeability of the interbundle channel is represented by the value of K/K_0, where K and K_0 are the permeabilities of the channel with and without stitches respectively. The effect of the stitch off-centre position on permeability is shown in Fig. 9.26, in which the x-coordinate is d/a, where d is the distance between the stitch centre and the channel centreline. Apparently, the effect of the stitch on the permeability of the channel is very different for different off-centre positions. When d/a increased from 0 to 0.7, i.e. the stitch location was moved from the centreline to close to the wall, the value of K/K_0 increased accordingly. These simulation results are consistent with the results of analysis by FLUENT.

In other cases, the stitch is always inclined towards the interbundle channel. So it is very necessary to make clear how the stitch slope will affect the equivalent permeability of the channel. The angle between the stitch orientation and the y-axis is defined as θ. In this section, the variation of K/K_0 with θ is investigated by keeping other parameters constant, such as R/a at 0.2, L/W at 2.0, and V_b/V_a at 0.4. As shown in Fig. 9.27, the permeability of the channel at $\theta = 0°$, 10°, 20° and 30° is simulated for different boundary conditions. The results show that K/K_0 decreases with increasing θ, but the difference for a unit increment of θ is very small when $\theta \leq 10°$.

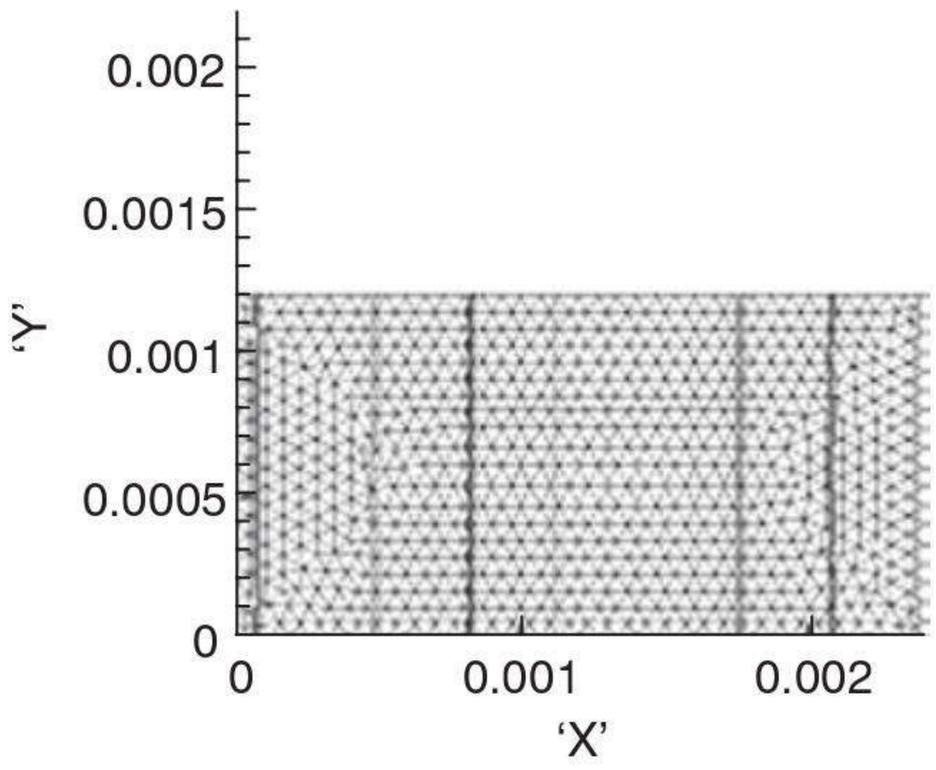

(a) Unit cell without stitch

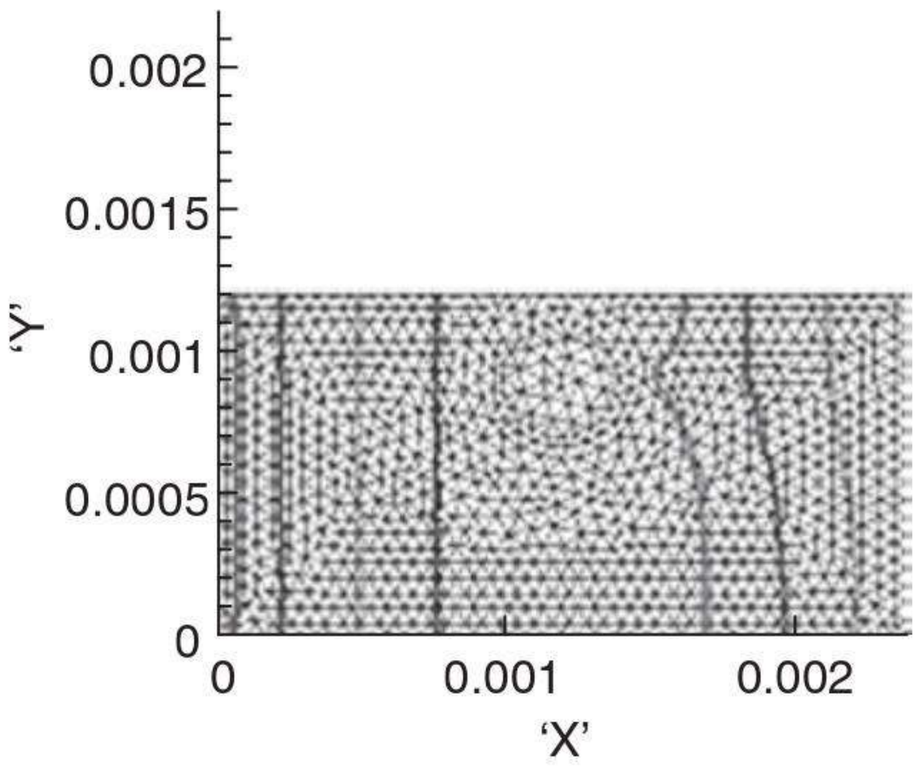

(b) *d*/*a* = 0.667

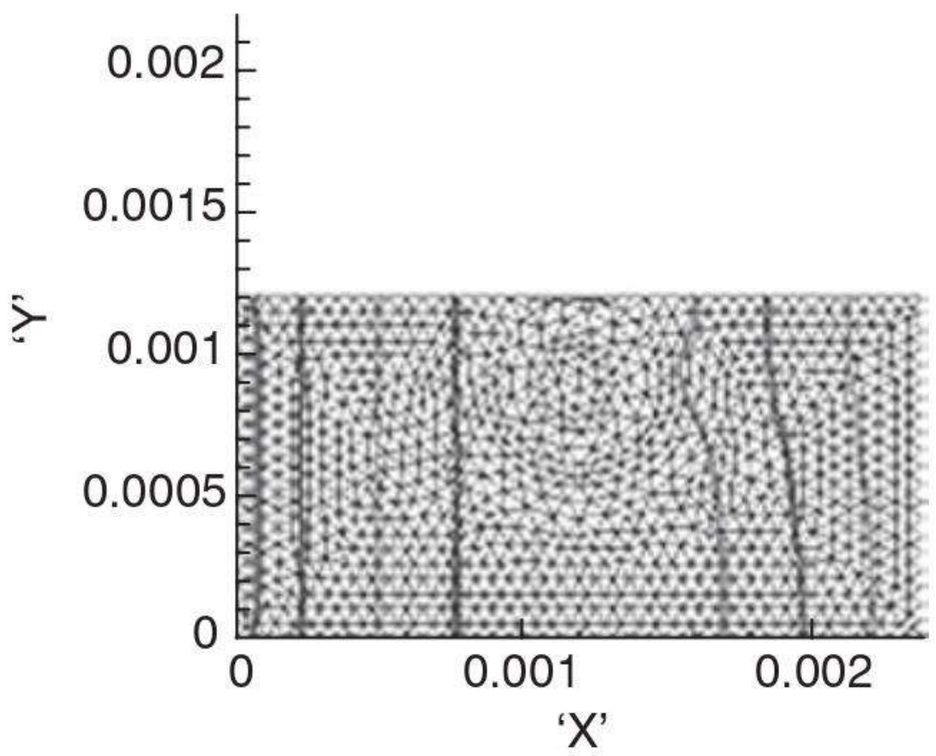

(c) *d*/*a* = 0.5

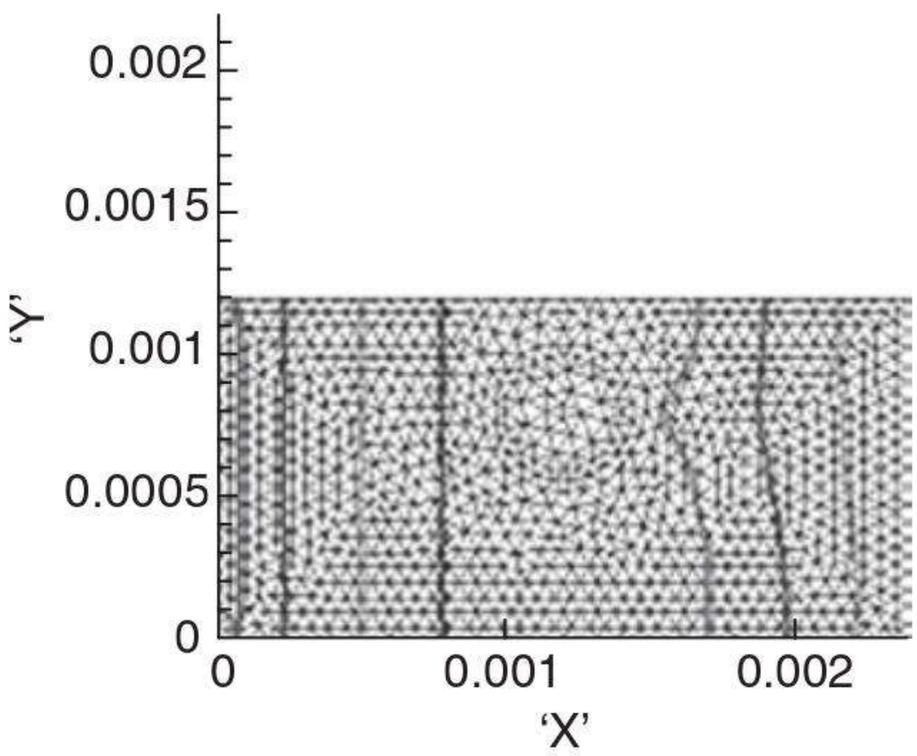

(d) *d*/*a* = 0.333

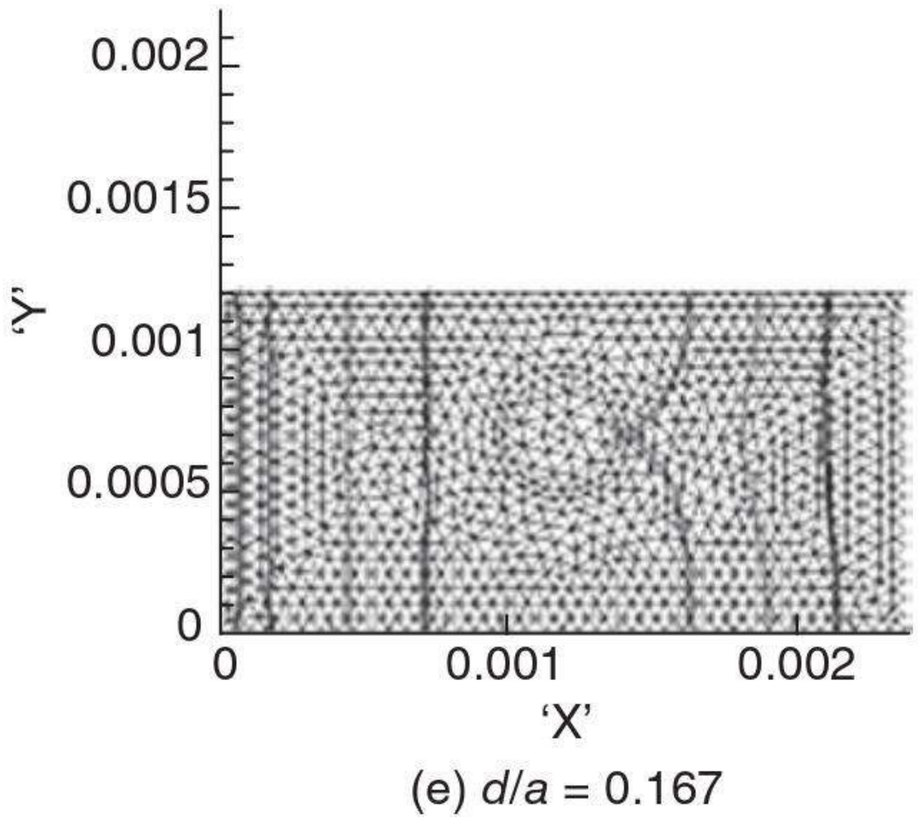

(e) *d*/*a* = 0.167

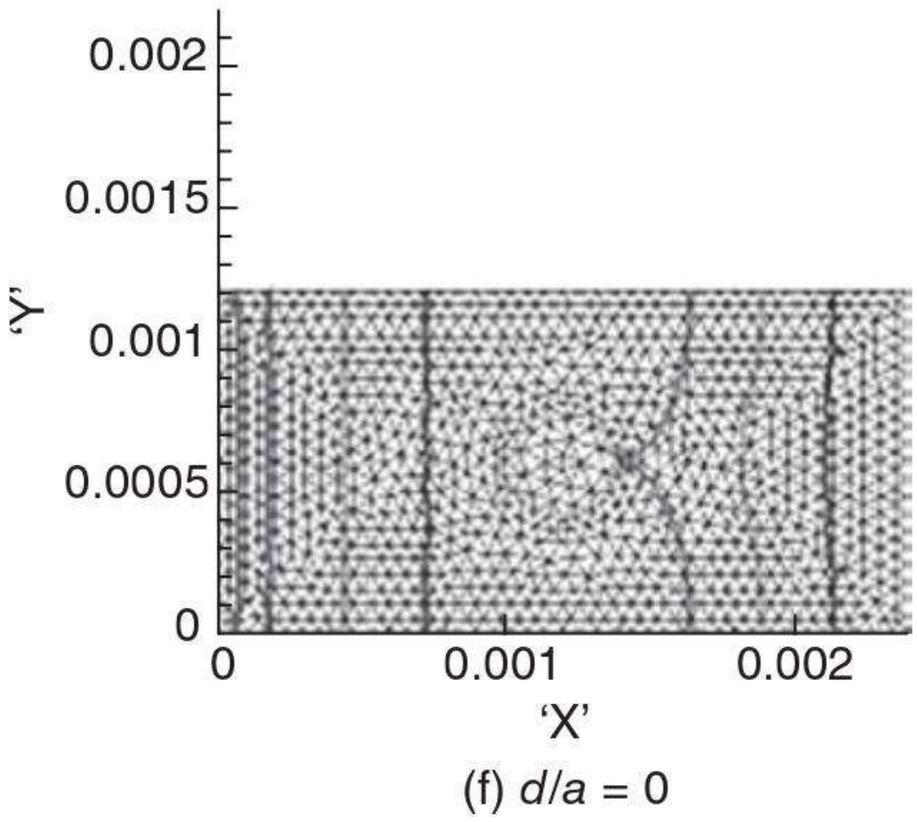

(f) *d*/*a* = 0

9.25 The simulation impregnation process of resin flow through the unit cell of the channel with stitch in the off-centre position.

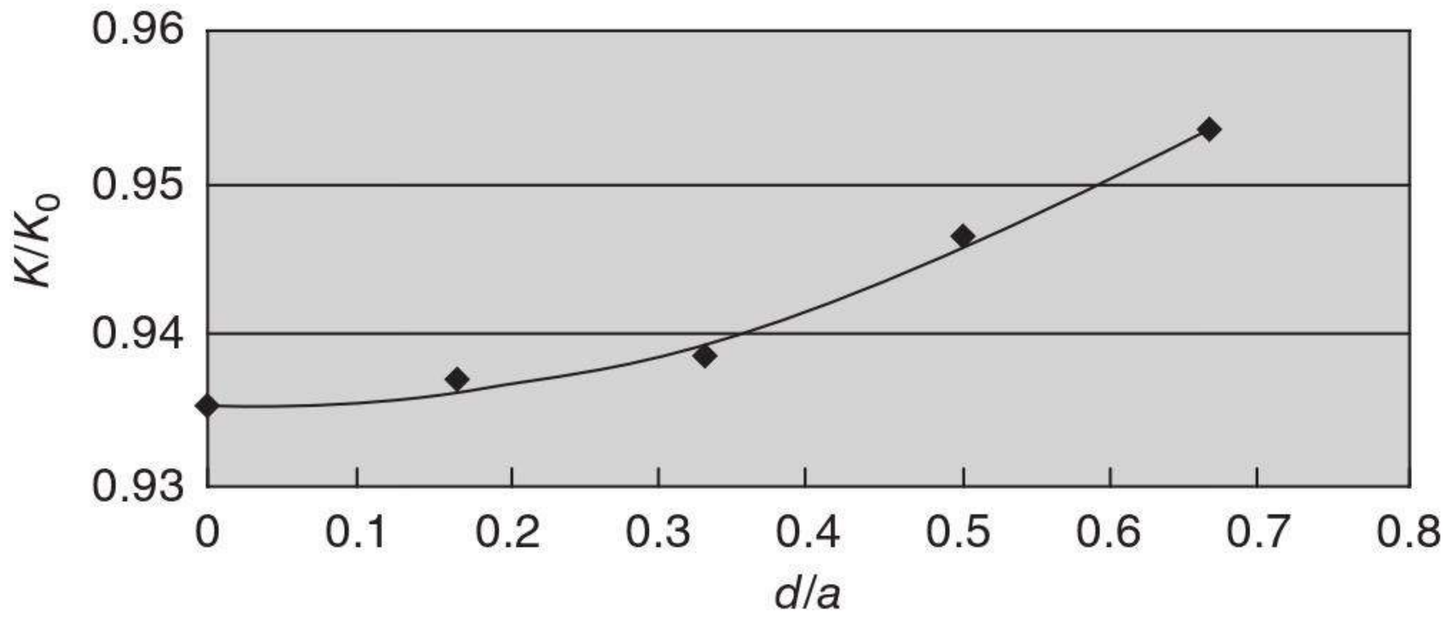

9.26 The effect of stitch off-centre position on permeability.

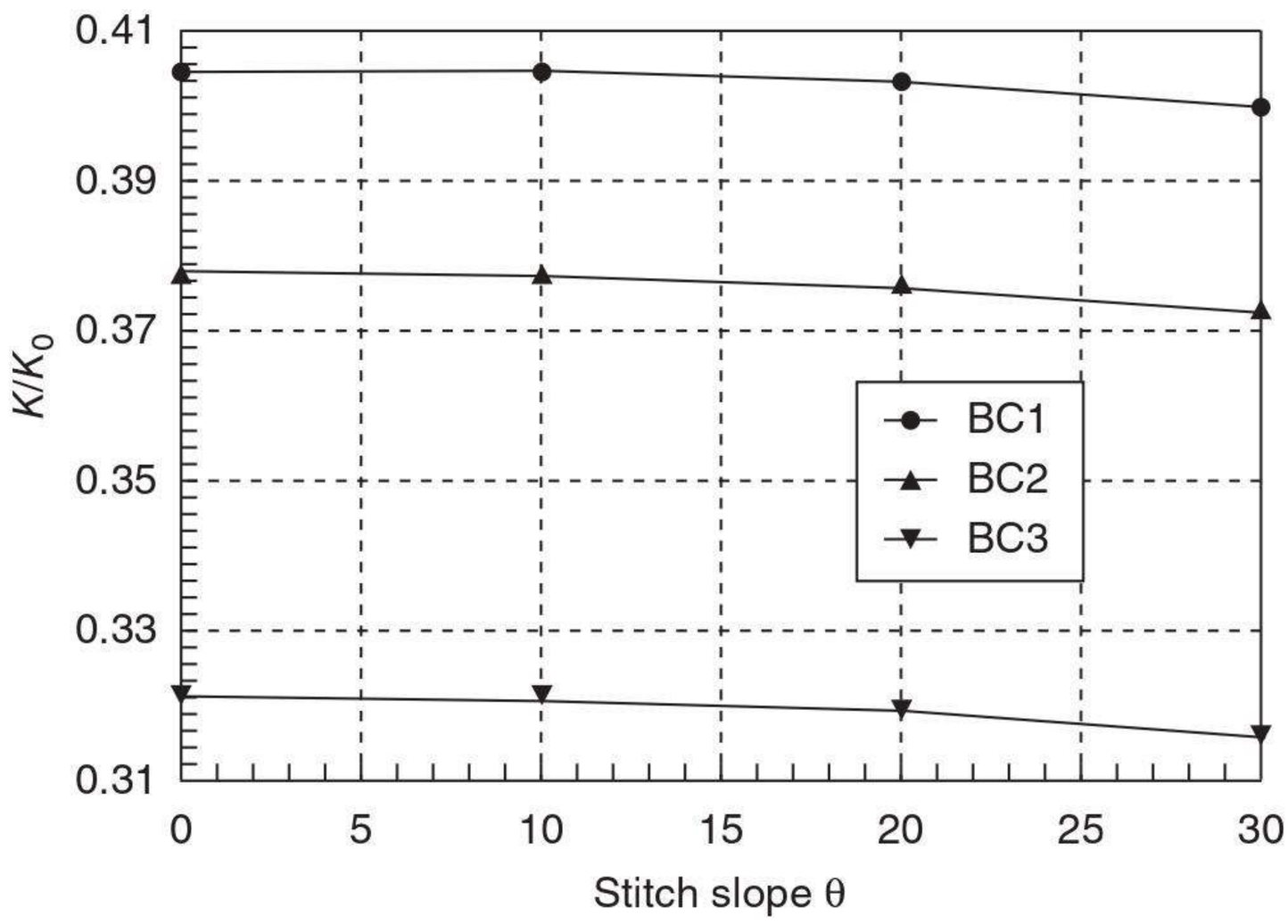

9.27 Change of K/K_0 with stitch slope θ.

This corresponds to the increment of surface area of the stitch in the channel with increasing θ. Therefore, it can be predicted that K/K_0 will decrease more quickly for larger θ. Comparing with other parameters, such as off-centre position and size, the effect of slope on the value of K/K_0 is relatively weaker.

9.5.4 The effect of stitch array

When there are two or more than two stitches in one representative cell, the effect of the stitches on the permeability of the channel must be different with different arrays. In this section, two situations are considered. Firstly, we consider that two stitches are located on the centreline, and arrayed up and down along the flow direction. We define this situation as array-1. Then two stitches are arrayed to be bilaterally symmetrical to

the centreline of the channel. We define this situation as array-2. In both situations, the distance between the two stitches is marked as D. For all simulated cases in this section, R/a is 0.2, L/W is 2.0, and V_b/V_a is 0.4.

In the case of array-1, the variation of K/K_0 with D/L is shown in Fig. 9.28(a). In this case, when D/L is equal to 0.1, two stitches should remain in contact with each other. The simulation results show that K/K_0 at D/L = 0.1 is relatively higher, and decreases quickly at first and then slowly with increasing D/L. When D/L is equal to 0.5, the value of K/K_0 should be the

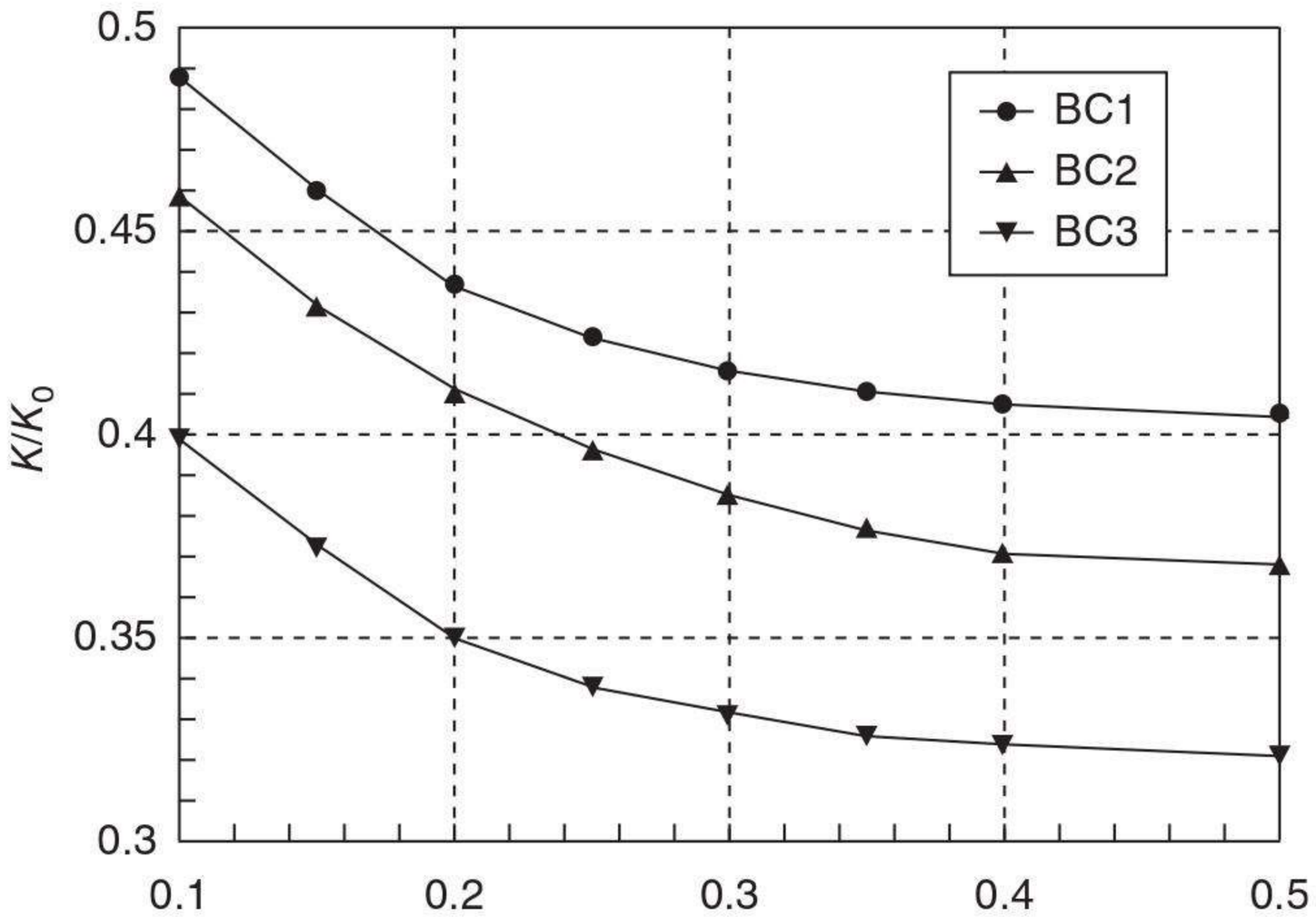

(a) Array-1

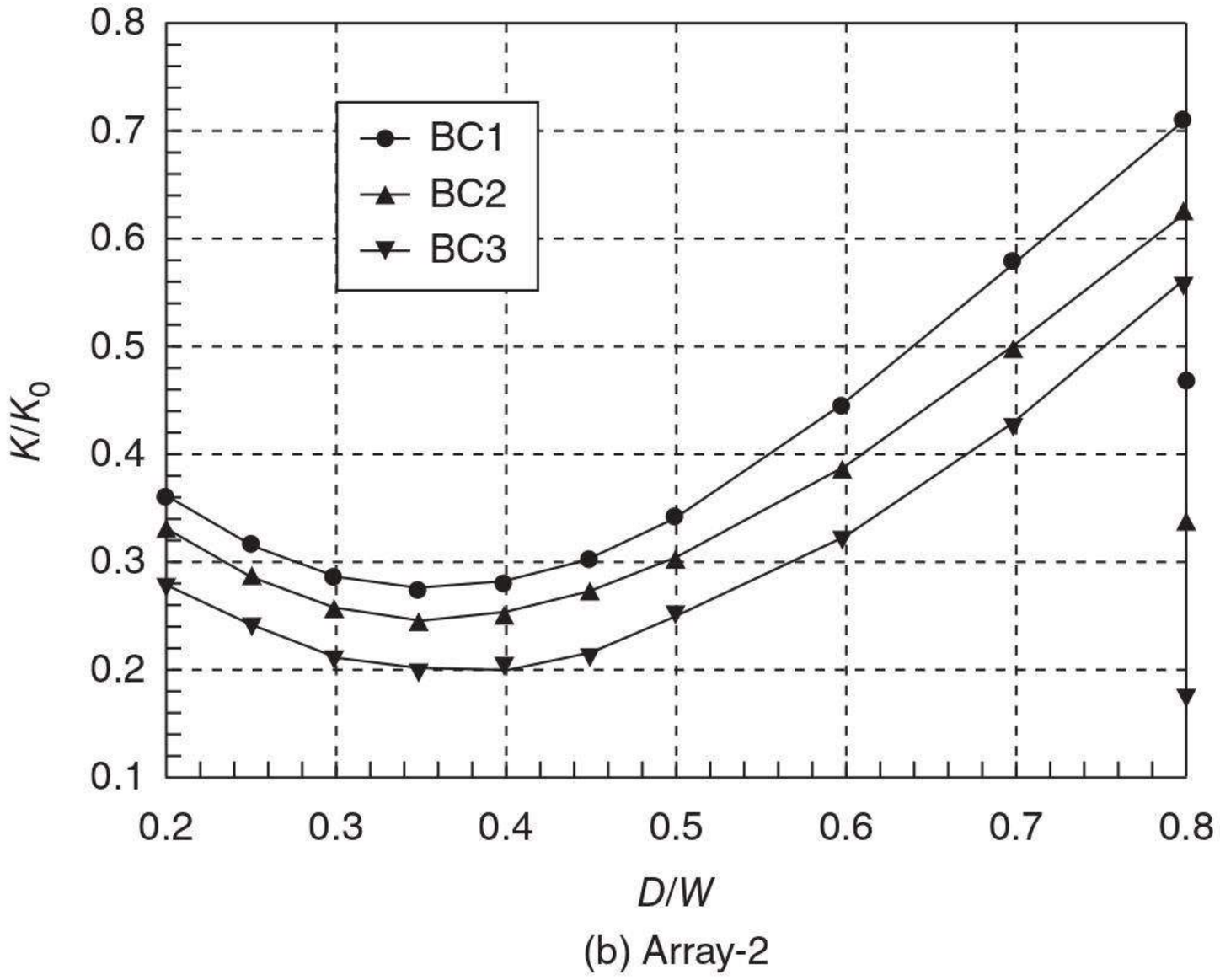

(b) Array-2

9.28 Change of K/K_0 with L/W in the cases of array-1 and array-2.

same as in the case where there is only one stitch in the representative cell for $L/W = 1.0$.

In the case of array-2, when D/W is equal to 0.2, two stitches also should remain in contact with each other, and when D/W is equal to 0.8, the stitch should touch the sidewall of the channel. The simulation results are shown in Fig. 9.28(b), which shows that the variation of K/K_0 with D/W is not monotonous. When two stitches move simultaneously from the centre to the sidewall of the channel, K/K_0 first decreases when D/W is equal to 0.35–0.40, then reaches its minimum, and then increases linearly. The difference between the minimum and maximum of K/K_0 is about three times. Therefore, a slight change in stitch array will induce a distinct variation of the permeability of the channel.

The impregnation process for the case of array-2 was also simulated by the finite element simulation. The schematic of the simulation unit is shown in Fig. 9.29, where the stitch off-centre position in the channel is represented by the ratio between the stitch centre distance and the channel length (d/b).

Based on the finite element method, the impregnation process of resin flow through the unit cell of the channel with stitch in the off-centre position (two stitches) is shown in Fig. 9.30(a)–(g).

The effect of stitches on the equivalent permeability of the interbundle channel is represented by the value of K/K_0. The effect of the stitch off-centre position on the permeability is shown in Fig. 9.31, in which the x-coordinate is d/b, where d is the half-length of the channel and b is the distance between the stitch centers. The stitch off-centre position can be expressed by d/b.

In this figure, when d/b is equal to 0.1667, two stitches should also keep touching each other, and when d/b is equal to 0.8333, the stitch should touch the sidewall of the channel. The simulation results are shown in Fig. 9.31, which shows that the change of K/K_0 with d/b is not monotonous. When two stitches approach closer, K/K_0 first decreases when d/b is equal to

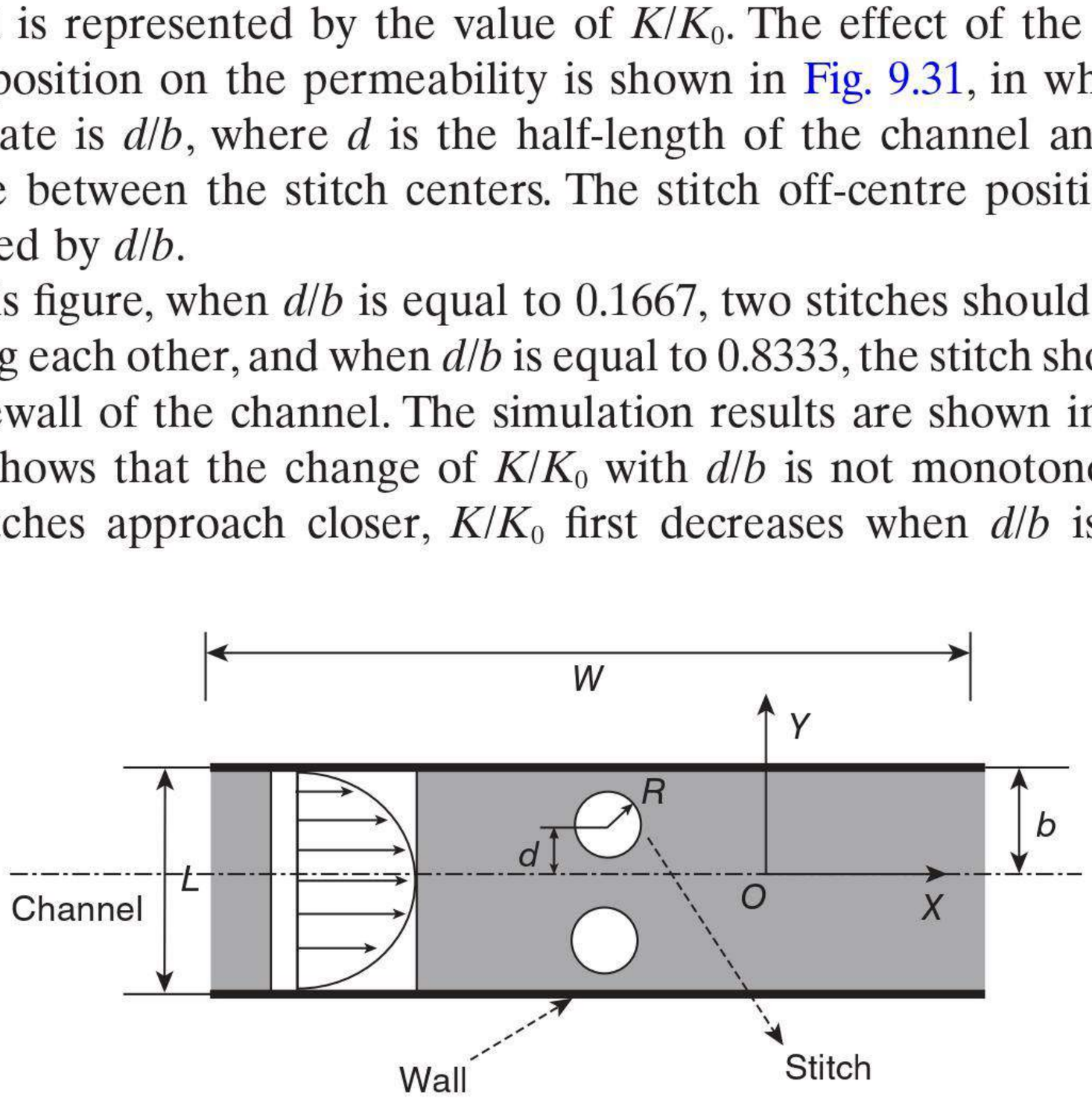

9.29 Unit cell of channel flow with stitch in the off-centre position (two stitches).

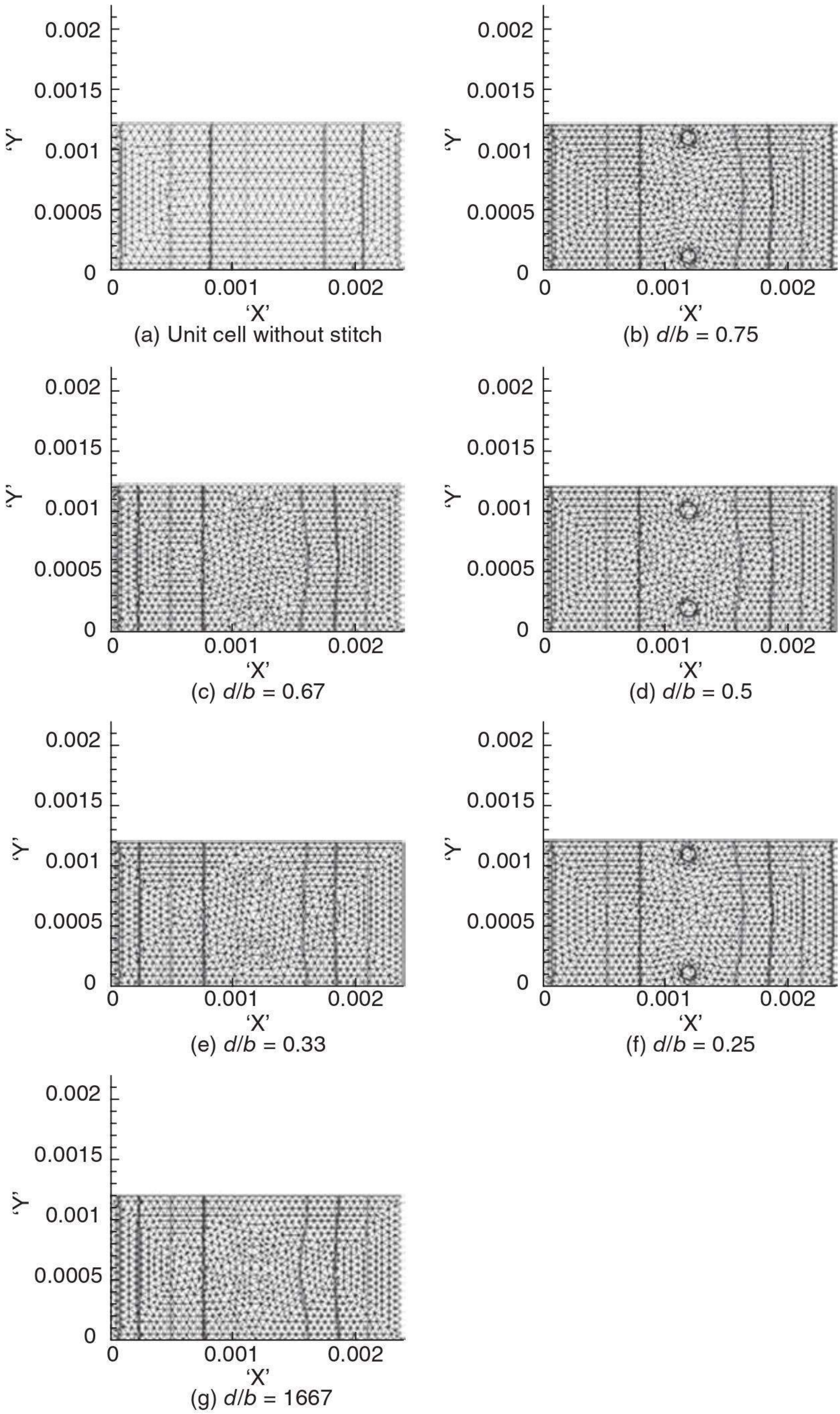

(a) Unit cell without stitch

(b) $d/b = 0.75$

(c) $d/b = 0.67$

(d) $d/b = 0.5$

(e) $d/b = 0.33$

(f) $d/b = 0.25$

(g) $d/b = 1667$

9.30 The simulation impregnation process of resin flow through the unit cell of the channel with stitch in the off-centre position (two stitches).

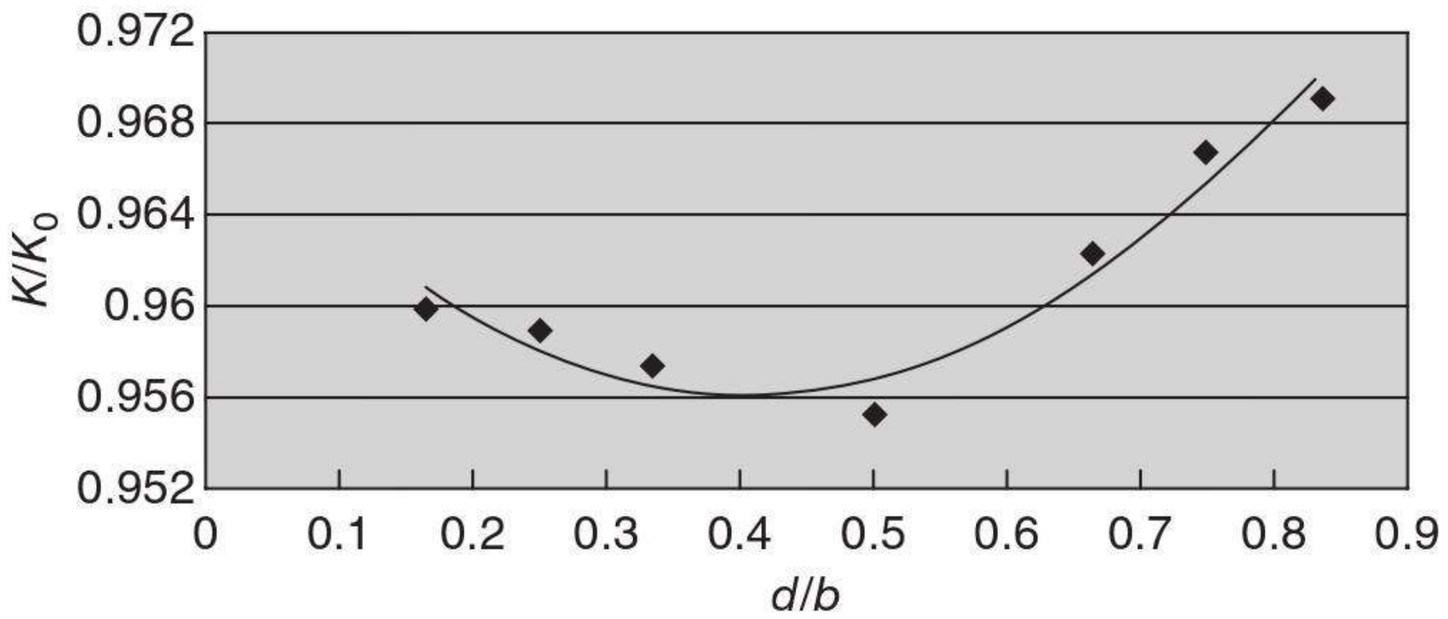

9.31 The effect of stitch off-centre position (two stitches) on permeability.

0.4–0.5, then reaches its minimum value, then with increase of d/b, K/K_0 increases linearly. These simulation results also correspond with the results of analysis by FLUENT.

9.6 Conclusions

In this chapter two simplified unit cells for in-plane impregnation in multilayer woven fabric have been suggested. In addition a mathematical model has been developed to analyze the void formation in both unit cells during RTM processes. The model recognizes non-uniform fibre permeability in different sub-domains of fibre preforms. Although a few simplifying assumptions have been introduced, the model still accounts for the key mechanisms of void formation in the cross-section of MWFs. The location of the void predicted by this model agrees quite well with the experiments. The model also shows that the ratio of weft axial permeability K_b^a to warp transverse permeability K_b^t largely determines the formation and size of voids.

The flows in both unit cells also were numerically simulated using the control-volume method. The presented numerical scheme was first tested by comparing it with mould-filling cases for which analytical solutions exist. The simulated results, including flow fronts and the effect of K_b^a/K_b^t, agree with the prediction according to the analytical model. The size of the void is proportional to the ratio K_b^a/K_b^t (Hu *et al.*, 2004).

Numerical simulations of flow in the interbundle channel with stitch have been carried out, and the effect of the stitch on the equivalent permeability of the interbundle channel has been revealed. The results show that stitches may severely affect the permeability of channels, even if their size is relatively smaller. So this effect has to be considered when establishing an effective permeability model for multilayer fabrics with stitches.

The numerical simulation results also suggest that the effect of a stitch is quite different for different stitch size, off-centre position, slope, array,

distribution density in the flow direction, and average Darcy velocity in fibre bundles. Therefore, with only one variable, usually the radius of the stitch, R, the permeability status of the interbundle channel is still very uncertain.

The effect of stitches on the equivalent permeability of the interbundle channel is presented by the value of K/K_0. The numerical simulation results suggest that the effect of stitches is quite different for different stitch size, off-centre position, slope, array, distribution density in the flow direction, and average Darcy velocity in fibre bundles. The value of K/K_0 will decrease with the increase of stitch size, slope and average Darcy velocity in fibre bundles, and will also decrease with the increase of off-centre distance. When there are two stitches in a representative cell, for an up and down array (array-1), the value of K/K_0 will decrease with increasing space between two stitches. For a left and right array (array-2), when two stitches move simultaneously from the centre to the sidewall of channel, K/K_0 first decreases to a minimum and then increases linearly.

9.7 References

Barooah P, Berker B and Sun J Q (2001), Integrated switching and feedback control for mold filling in resin transfer molding, *Journal of Manufacturing Science and Engineering*, **123**, May, 241.

Binetruy C and Hilaire B (1998), Tow impregnation model and void formation mechanisms during RTM, *Journal of Composite Materials*, **32**, 3, 223–245.

Bowles K J and Frimpong S (1991), Void effects on the interlaminar shear strength of unidirectional graphite-fiber-reinforced composites, *Journal of Composite Materials*, **26**, 1487–1509.

Cai Z and Berdichevsky A L (1993), An improved self-consistent method for estimating the permeability of a fiber assembly, *Polymer Composites*, **14**, 4, 314–323.

Cairns D S, Humbert D R and Mandell J F (1999), Modeling of resin transfer molding of composite materials with oriented unidirectional plies, *Composites, Part A: Applied Science and Manufacturing*, **30**, 375–382.

Carman P C (1937), Fluid flow through granular beds, *Transactions of the Institution of Chemical Engineers*, **15**, 150–166.

Chan A W and Morgan R J (1992), Sequential multiple port injection for resin transfer moulding of polymer composites, *SAMPE Quarterly*, **23**, 45–49.

Chang C Y and Hourng L W (1998), Study on void formation in resin transfer molding, *Polymer Engineering and Science*, **38**, 5, 809–818.

Chen Y T, Davis H T and Macosko C W (1995), Wetting of fiber mats for composites manufacturing: 1. Visualization experiments, *AIChE Journal*, **41**, 10, 2261.

Feldgoise S, Foley M F, Martin D and Bohan J (1991), The effect of microvoid content on composite shear strength, *Proc. 23rd International SAMPE Symposium*, 259–273.

Frederick R and Phelan J R (1997), Simulation of the injection process in resin transfer molding, *Polymer Composites*, **18**, 4, 460–476.

Gebart B R (1992), Permeability of unidirectional reinforcements for RTM, *Journal of Composite Materials,* **26**, 8, 1100–1133.

Ghiorse S R and Jurta R M (1991), Effects of low frequency vibration processing on carbon/epoxy laminates, *Composites*, **22**, 1, 3–8.

Gutowski T G, Morigaki T and Cai Z (1987a), The consolidation of laminate composites, *Journal of Composite Materials*, **21**, 172–188.

Gutowski T G, Cai Z, Bauer S, Boucher D, Kingery J and Wineman S (1987b), Consolidation experiments for laminate composites, *Journal of Composite Materials*, **21,** 650–669.

Harper B D, Staab G H and Chen R S (1987), A note on the effects of voids upon the hygral and mechanical properties of AS4/3502, *Journal of Composite Materials*, **21**, 280–289.

Hayward J S and Harris B (1990), Effect of process variables on the quality of RTM moulding, *SAMPE Journal*, **26**, 3, 39–46.

Hu J L, Liu Yi and Shao X M (2003), Effect of stitches on the permeability of interbundle channels in stitched fabrics, *Textile Research Journal*, **73**, 8, 691–699.

Hu J L, Liu Yi and Shao X M (2004), Study on void formation in multi-layer woven fabrics, *Composites: Part A, Applied Science and Manufacturing*, **35**, 595–603.

Kang M K, Lee W I and Hahn H T (2000), Formation of microvoids during resin-transfer molding process, *Composites Science and Technology,* **60**, 2427–2434.

Lundström T S (2000), The permeability of non-crimp stitched fabrics, *Composites, Part A: Applied Science and Manufacturing*, **31**, 1345–1353.

Parnas R S and Phelan Jr F R (1991), The effect of heterogeneous porous media on mold filling in resin transfer molding, *SAMPE Quarterly*, **22,** 53–60.

Patel N and Lee L J (1995), Effects of fiber mat architecture on void formation and removal in liquid composite molding, *Polymer Composites*, **16**, 5, 386–399.

Rohatgi V, Patel N and Lee L J (1996), Experimental investigation of flow-induced microvoids during impregnation of unidirectional stitched fiberglass mat, *Polymer Composites*, **17**, 161–170.

Shih C H and Lee L J (1998), Effect of fibre architecture on permeability in liquid composite molding, *Polymer Composites*, **19**, 5, 629–639.

Simacek P and Advani S G (1996), Permeability model for a woven fabric, *Polymer Composites*, **17**, 887–899.

Williams J G, Morris C E M and Ennis B C (1974), Liquid flow through aligned fiber beds, *Polymer Engineering and Science*, **14**, 6, 413–419.

Yong W B, Han K, Fong L H and Lee L J (1991), Flow simulation in molds with preplaced fiber mats, *Polymer Composites*, **12**, 6, 391–403.

Yosida H T, Ogasa T and Hayashi R (1986), Statistical approach to the relationship between ILSS and void content of CFRP, *Composites Science and Technology*, **25**, 3–18.

Yu B and Lee L J (2000), A simplified in-plane permeability model for textile fabrics, *Polymer Composites*, **21**, 5, 660–685.